

Effects of a stratified tidal flow on the morphodynamics

Meirelles, Saulo

DOI

[10.4233/uuid:b98e7799-c0d3-42ca-8c9c-70ee64bf059a](https://doi.org/10.4233/uuid:b98e7799-c0d3-42ca-8c9c-70ee64bf059a)

Publication date

2019

Document Version

Final published version

Citation (APA)

Meirelles, S. (2019). *Effects of a stratified tidal flow on the morphodynamics*. [Dissertation (TU Delft), Delft University of Technology]. <https://doi.org/10.4233/uuid:b98e7799-c0d3-42ca-8c9c-70ee64bf059a>

Important note

To cite this publication, please use the final published version (if applicable).
Please check the document version above.

Copyright

Other than for strictly personal use, it is not permitted to download, forward or distribute the text or part of it, without the consent of the author(s) and/or copyright holder(s), unless the work is under an open content license such as Creative Commons.

Takedown policy

Please contact us and provide details if you believe this document breaches copyrights.
We will remove access to the work immediately and investigate your claim.

Effects of a stratified tidal flow on the morphodynamics

Effects of a stratified tidal flow on the morphodynamics

Meirelles, S.

Saulo Meirelles



Saulo Meirelles

✉ s.meirellesnunesdarocho@tudelft.nl

✉ [s_meirelles](https://www.instagram.com/s_meirelles)

✉ [@SauloMeirelles_](https://twitter.com/SauloMeirelles_)

in Saulo Meirelles

EFFECTS OF A STRATIFIED TIDAL FLOW ON THE
MORPHODYNAMICS

DISSERTATION

for the purpose of obtaining the degree of doctor
at Delft University of Technology
by the authority of the Rector Magnificus, Prof. Dr. Ir. T. H. J. van der Hagen,
chair of the Board for Doctorates
to be defended publicly on
Monday 7 January 2019 at 10:00 o'clock

by

Saulo MEIRELLES NUNES DA ROCHA
Master of Science in Coastal Engineering, Federal University of Rio de Janeiro, Brazil
born in Rio de Janeiro, Brazil

This dissertation has been approved by the promotors.

Composition of the doctoral committee:

Rector Magnificus

prof. dr. ir. M.J.F. Stive

prof. dr. ir. A.J.H.M. Reniers

prof. dr. J. D. Pietrzak

Chairperson

Delft University of Technology, promotor

Delft University of Technology, promotor

Delft University of Technology, promotor

Independent members:

prof. dr. ir. S.G.J. Aarninkhof

prof. dr. ir. J. A. Roelvink

prof. dr. A. Falqués

dr. ir. M. A. de Schipper

Delft University of Technology

IHE/Delft University of Technology

Universitat Politècnica de Catalunya

Delft University of Technology

Prof. Dr. Alejandro Souza, Prof. Dr. Alexander Horner-Devine and ir. Martijn Henriquez have substantially contributed as supervisors of this research.

This research was funded by the ERC-Advanced Grant 291206 – Nearshore Monitoring and Modeling (NEMO) and Deltares.

Keywords: stratification, bedforms, sediment transport

Printed by: ProefschriftMaken || www.proefschriftmaken.nl

Cover by: Saulo Meirelles

Copyright©2019 by Saulo MEIRELLES

There are no facts, only interpretations.

— Friedrich Nietzsche in Notebooks (Summer 1886 – Fall 1887)

To Mini, Yang and Bel.

CONTENTS

1	INTRODUCTION	1
1.1	Context	1
1.2	The importance of the inner shelf	2
1.3	Objectives	4
1.4	Outline	5
I	HYDRODYNAMICS	7
2	CROSS-SHORE STRATIFIED TIDAL FLOW	9
2.1	Introduction	9
2.2	Study area	13
2.3	Methods	14
2.3.1	Field campaign	14
2.3.2	ADCP data processing	15
2.3.3	Tidal current ellipses	16
2.3.4	Cross-shore exchange currents	16
2.4	Observations	18
2.5	Discussion	25
2.6	Conclusions	29
3	BED SHEAR STRESS IN THE DUTCH INNER SHELF	31
3.1	Introduction	31
3.2	Study area and field observation	32
3.3	Methodology	32
3.3.1	The Madsen [1994] model	32
3.4	Data analysis	34
3.5	Results	35
3.6	Discussion and conclusions	38
II	MORPHODYNAMICS	39
4	SMALL SCALE BEDFORM TYPES IN THE DUTCH INNER SHELF	41
4.1	Introduction	41
4.2	Methods	42

4.2.1	Study area	42
4.2.2	Data collection	42
4.2.3	Data analysis	44
4.3	Results	47
4.4	Discussion	49
4.5	Conclusions	52
5	EFFECTS OF A STRATIFIED TIDAL FLOW ON THE BEDFORM DYNAMICS	53
5.1	Introduction	53
5.2	Methods	55
5.3	Results	55
5.3.1	Spring-neap variability	58
5.3.2	Ripple response to stratified and non-stratified spring tide currents	58
5.3.3	Semi-diurnal variability	62
5.3.4	Ripple migration rates	66
5.4	Discussion	69
5.4.1	Impact on the sediment transport	70
5.5	Conclusions	74
6	CONCLUSIONS	77
	ACKNOWLEDGMENTS	95
	CURRICULUM VITAE	97
	PUBLICATIONS	99

LIST OF FIGURES

Figure 1.1	The Sand Engine a few months after its construction. Picture courtesy of Rijkswaterstaat/Joop van Houdt.	3
Figure 1.2	Illustrative sketch of the processes that drive morphological changes in the inner shelf (highlighted in red). Modified from: Wright [1995].	4
Figure 2.1	Study area location. (a) The inset shows the location of the Holland Coast, the Sand Engine and the Rotterdam waterways within the Netherlands; (b) the Sand Engine a few months after its completion; and (c) the Sand Engine during the field experiment in Sep 2014 (Courtesy of Rijkswaterstaat/Joop van Houdt). The transects crossed the isobaths from approximately -12 to -8 m. The gray circles show the location of the 153 CTD casts. The Delft3D-FM computational grid is also shown as a reference.	10
Figure 2.2	Idealized interplay between baroclinic pressure gradient (P) and centrifugal acceleration (C) along a cross-shore profile off the tip of the Sand Engine. The plus and minus signs indicate positive and negative vertical shear in the cross-shore (see text for explanation), their colors indicate the terms P (black) and C (gray) and their size indicate the magnitude. The panels show the cross-shore distribution of the cross-shore exchange currents generated by P and C . Blue arrows are offshore-directed and red arrows are onshore-directed. The colored dots indicate when the cross-shore currents are nearly zero.	12
Figure 2.3	Time series of the observed cross- and alongshore profiles of the tidal velocities and density at the offshore (a, b, e, f, i and j) and onshore (c, d, g, h, k and l) limits of T_1 (left) and T_2 (right). The low water (LW) and high water (HW) tidal stages are indicated in (a) and (b). There is no CTD data after 1500H at T_2 as seen by the blank space in (j and l).	20

Figure 2.4	(a and b) Cross-shore density structure and the respective cross-shore velocity profiles at the seaward limit of T ₁ . (c to f) Radar images of the Northern flank of the Sand Engine during four distinct periods of the survey. The contours in the images show the edge of the plume front. (g to j) Density profiles taken at the offshore (black line) and nearshore (gray line) limits of T ₁ for the same periods of the radar images.	21
Figure 2.5	Time series of the squared vertical shear (S^2), buoyancy frequency (N^2) and the transformed Richardson Number ($\log(4Ri)$, where $Ri = N^2/S^2$) at the offshore (a, b and c) and onshore (d, e and f) limits of T ₁ . The thick gray lines mark the HW and LW slacks (i.e, $v = 0$).	22
Figure 2.6	Main parameters of the M ₂ tidal current ellipse at transect T ₁ . (a) M ₂ amplitude; (b) M ₂ phase; (c) M ₂ ellipticity.	23
Figure 2.7	(Previous page.) Upper panel: Depth-averaged alongshore (black line) and cross-shore velocities near the bed (dark gray line) and near the surface (light gray line) velocities. The velocities were taken from the offshore limit of T ₁ . Lower panel: vertical shear during 8 distinct periods over the tidal cycle. Negative values indicate a tendency to counterclockwise cross-shore circulation. The vectors represent the cross-shore velocities and the contour line indicates zero velocity.	25
Figure 2.8	(Previous page.) (a to h) Distribution of the baroclinic forcing (squares) and centrifugal acceleration (circles) along transect T ₁ during 8 distinct periods of the tidal cycle. (i) Violin plot of the estimated centrifugal acceleration off the tip of the Sand Engine considering the changes in the radius of curvature (R, in meters) from 2011 until 2015. The shapes correspond to the distribution of the data during spring (red) and neap (blue) with their respective maxima (colored bars) and means (black bars). The dashed black line and shaded area show the mean and standard deviation of the baroclinic forcing. The dashed gray line in (i) indicates the maximum baroclinic forcing. (j) Scaled terms of the cross-shore exchange flow governing equation (left y-axis), and near surface and near bottom cross-shore velocities (right y-axis) at the seaward limit of T ₁	28

Figure 3.1	Wave peak period extracted from the wave records during the STRAINS experiment plotted against the relative depth h/L	34
Figure 3.2	Oceanographic conditions during the STRAINS experiment. From top to bottom: [1] water elevation (the red rectangles indicate spring tides); [2] significant wave height (left axis; black circles) and wind speed (right axis; grey triangles); [3] peak period, T_p ; [4] wind (grey triangles) and wave direction (black circles).	36
Figure 3.3	Computed bed shear stress using the Madsen (1994) approach (the red rectangles indicate spring tides). From top to bottom: [1] tide-induced bed shear stress; [2] wave induced bed shear stress; [3] residual current induced bed shear stress. The red horizontal lines indicate the critical bed shear stress with respect to the d_{50} during the STRAINS.	37
Figure 3.4	tide, wave, and residual current bed stresses together with top-to-bottom salinity difference averaged across all M_2 tidal cycles of the first (left panel) and second (right panel) spring tides. The vertical dashed black line indicates the rapid increase of stratification.	37
Figure 4.1	Location of the study area and the measurement site where the Mini Stable was deployed. (a) The inset shows the Netherlands, the Holland Coast with the Sand Engine and the Rotterdam waterways; (b) the Sand Engine a few months after its completion; and (c) the Sand Engine during the field experiment in Sep 2014 (Courtesy of Rijkswaterstaat/Joop van Houdt)	43
Figure 4.2	Occurrence of current ripples (C), wave ripples (W), combined wave-current ripples (WC), current ripples with subordinate wave ripples (Cw), wave ripples with subordinate current ripples (Wc) and poorly developed ripples (P). This result is based on the visual identification explained in the text	48
Figure 4.3	(a) time series, in days of 2014, of the wave and current mobility numbers. The hatched areas depict the spring tide periods. (b) series of the logarithm of the ratio of $\psi_{rms,w}$ to $\psi_{rms,c}$ compared to the results from the visual observation. The green, yellow, red, blue, gray and black marks correspond to W, Wc, WC, Cw, C and P, respectively.	50

Figure 4.4 Seafloor imagery of a wave-formed ripple observed during the storm event on day 265 (a); and current-formed ripple observed during the first spring tide on day 271 (b). The trajectories seen in (a) and (b) were extracted from 13 consecutive images (i.e., approximately one tidal cycle) using optical flow technique (pixel tracking). The ending point of the trajectories is shown by the red circles (also seen in the insets). The insets in (a) and (b) depict the 2-D histogram of all trajectories together providing a first order estimation of the magnitude and direction of the mean ripple migration respectively. 51

Figure 5.1 Observed conditions during the field measurements. (a) water-level derived from the ADV pressure sensor; (b) ripple height; (c) significant wave height (red) and wind speed (blue); (d) wave (red) and wind (blue) directions; (e) wave peak period; and (f) river discharge. The spring tides are marked by the gray areas and the hatches inside the gray areas indicate the periods used to investigate the bedform behavior with respect to stratification (see text for details). 56

Figure 5.2 Imagery of the seabed for four different periods correspondent to Neap 1 (a); Spring 1 (b); Neap 2 (c) and Spring 2 (d). The current speed (blue arrows) and the orbital velocity (red arrow) are also indicated on the images. The approximate orientation of the coastline is represented by the Sand Engine contour (not to scale). 57

Figure 5.3 (Previous page.) Time series of the main parameters during Neap 1, Spring 1, Neap 2 and Spring 2. (a) Alongshore (black line; left y-axis) and cross-shore (red line; right y-axis) mean flow; (b) Alongshore (black line; left y-axis), cross-shore (red line; left y-axis) wind velocity, and wind stress, in Pa, at the sea surface (shaded area in gray; right y-axis); (c) mean ripple height; (d) ripple weighted peak wavelength; (e) $k_y/|k|$ ratio; (f) Alongshore (black line; left y-axis) and cross-shore (red line; left y-axis) ripple migration rates, and ripple migration magnitude (shaded area in gray; right y-axis); (g) top-to-bottom salinity differences. The vertical blue lines indicate the peaks observed in the ripple migration rates during Spring 2. The vertical magenta lines indicate the time when the images in Figure 5.2 were collected. The events with $H_s \geq 1$ m were left out from this figure. 60

Figure 5.4 Polar histogram of wind direction during Spring 1 (upper panels) and Spring 2 (lower panels) in which the background colors indicate the stratification of the water column based on binned values of ΔS , which range from 0 (well-mixed) to 8 (strongly-stratified) (a-d). The colormap provides a measure of the wind strength. The Sand Engine contour line (1 m above sealevel) is shown in black. 61

Figure 5.5 (Previous page.) Phase-averaged quantities computed for Spring 1 and 2 periods. (a) Alongshore (black line; left y-axis) and cross-shore (red line; right y-axis) tidal flow; (b) magnitude of ripple migration (black line; left y-axis) and top-to-bottom salinity differences (red/green line; right y-axis); (c) Alongshore (black line; left y-axis) and cross-shore (red line; right y-axis) ripple migration rates; (d) ripple mean height (black line; left y-axis) and $k_y/|k|$ ratio (red line; right y-axis); (e) Total current shear velocity [Grant and Madsen, 1979] (black line; left y-axis), critical shear velocity for initiation of suspended load transport (red line; right y-axis), and critical shear velocity for initiation of sediment motion (gray line; right y-axis). All the quantities were averaged over the M_2 period (=12.42 hours). Note that the vertical scale of the top-to-bottom salinity in (b) is not the same in Spring 2 and therefore it is plotted in green. 65

Figure 5.6 (Previous page.) Time series of cumulative fluxes of (a) alongshore ripple migration rates (red line), mean residual transport velocities (blue line) and wave-driven residual transport velocities (green line); (b) same as (a) but in the cross-shore; (c) Ellipticity of the ripple migration (red line), ellipticity of the tidal flow (blue line) and top-to-bottom salinity difference smoothed over a M_2 period; (d) Stick plot of the wind series. The hatched gray lines show Spring 1 and Spring 2. The red panels on the bottom of (a) and (b) show a zoomed in view of the migration rates during Spring 1 and 2. The yellow areas in (d) indicate the periods where the significant wave height was ≥ 1 m. The vertical blue lines (a-d) indicate the peaks observed in the ripple migration rates during Spring 2. 68

Figure 5.7 Scatter plot of (a) tidal current ellipticity against top-to-bottom salinity; and (b) ripple ellipticity against top-to-bottom salinity during Spring 1 (blue circles) and 2 (red circles). 69

Figure 5.8	Net displacement, in normalized units of length, of (a) the mean flow; and (b) the ripple migration over Spring 1 (blue arrows) and Spring 2 (red arrows). The daily displacement of the mean flow (in a) and the ripple migration (in b) are shown by the blue (Spring 1) and red (Spring 2) lines. The approximated orientation of the coastline is represented by the Sand Engine contour.	71
Figure 5.9	Comparison of the bedload transport rates estimated from the measurements and predicted from a sediment transport model (upper panel); and the corresponding root-mean-square-error (lower panel). The spring tides are marked by the gray areas and the hatches inside the gray areas indicate Spring 1 and Spring 2.	72
Figure 5.10	(Previous page.) Bed- and suspended load series calculated from the observations. (a) alongshore bed- and suspended load transport rates; (b) cross-shore bed- and suspended load transport rates; (c) cumulative alongshore bed- and suspended load transport rates; and (d) cumulative cross-shore bed- and suspended load transport rates. The spring tides are marked by the gray areas and the hatches inside the gray areas indicate Spring 1 and Spring 2. The green areas indicate $\Delta S > 2$ and the yellow areas indicate waves higher than 1 m.	74
Figure 5.11	Schematic representation of the bedload (brown arrows) and suspended load (yellow arrows) under stratified (blue lines) and non-stratified (red lines) conditions. Vectors are not to scale.	75
Figure 6.1	Schematic diagram of the influence of stratification on the bed- (brown arrows) and suspended (yellow arrows) load transport in the alongshore (a-b) and cross-shore (c-d) directions. The blue dashed arrows represent the net transports and the North arrow is shown in black.	81

LIST OF TABLES

Table 5.1	Descriptive statistics of the main ripple parameters.	63
-----------	---------------------------------------------------------------	----

ABSTRACT

This thesis examines the effects of the stratified tidal flow on the morphodynamics of the Dutch inner shelf. The south portion of the Dutch inner shelf is strongly influenced by the Rhine River ROFI (Region Of Freshwater Influence), which is generated by the discharge from the Rhine River through the Rotterdam waterways. Under stratified conditions, the three-dimensional structure of the tidal currents develops a strong cross-shore shear so that the bottom and surface currents become 180° out of phase. The sheared flow created by stratification operates in the inner shelf and nearshore zones so that the flow asymmetries imparted by stratification are expected to impact the morphodynamics, however the role of the stratified tidal flow on the morphodynamics along the Dutch coast has been often neglected or oversimplified. In this context, this thesis aims to provide new insights on how the stratified tidal flow dictates the morphodynamics outside the surfzone.

In the south portion of the Dutch coast is located the Sand Engine, a 21.5 million m^3 experimental mega-nourishment that was built in 2011. This intervention created a discontinuity in the previous straight sandy coastline, altering the local hydrodynamics in a region that is influenced by the Rhine River ROFI. Estimates of the centrifugal acceleration directly after construction of the Sand Engine showed that its curved shape impacted the cross-shore flow, suggesting that the Sand Engine might have played a role in controlling the cross-shore exchange currents during the first three years after the completion of the nourishment. Presently, the curvature effects are minute owned to the morphodynamic evolution of the Sand Engine. Observations document the development of strong baroclinic-induced cross-shore exchange currents dictated by the intrusion of the river plume fronts as well as the classic tidal straining which are found to extend further into the nearshore (from 12 to 6 m depth), otherwise believed to be a mixed zone.

In the inner shelf, shoaling waves are as effective in mobilizing sediment as the other co-existing flows. The influence of stratification on the hydrodynamics is translated into near-bed shear velocity in the layer immediately above the sea floor. The tide-induced bed shear stress is able to periodically agitate the bed near the peaks of flood and ebb cycles mostly during spring tides. Results from observations suggested that,

under stratified conditions, relatively high values of bed shear stress are sustained for a prolonged period of time. The results also revealed that the non-tidal flow, such as the wind-induced flow, plays a role in controlling the bed mobility. However, wave-induced bed shear stress in general does not set sediment in motion during fair weather conditions and thus the stirring role of the waves is mostly important during storms.

The co-existing near-bed flows in the inner shelf are responsible for moulding the seafloor so that the resulting types of bedforms can reveal important information on the hydrodynamic forcings that dictate the sediment mobility. Observations showed that 59% of the ripples in the Dutch inner shelf are classified as current ripples. Wave ripples occur only during storm conditions, comprising 3%. The frequency of occurrence of transitional bed types composes 23% and poorly developed ripples is found to develop mostly during neap tides making up 15% of the observed bed types. The feedback of the different types of bedforms on the overlying boundary layer plays a fundamental role in the dynamics of the sediment load.

The morphological response of the bed to the stratified and non-stratified tidal flow leads to differentiations of the ripple migration as well as the sediment transport modes (bedload and suspended load). The bedforms at the measurement site are strongly controlled by tides so that their behavior exhibits not only a spring-neap signature, but also a distinct semi-diurnal fluctuation. Under the influence of the Rhine ROFI, the bedform mean dimensions (ripple height and wavelength) are reduced, indicating that their development is affected by the stratified tidal flow. In the absence of (ambient) stratification, the tidal current ripples are more developed, attaining relatively larger dimensions. The net alongshore bedload transport is south-directed, whereas the net alongshore suspended load is north-directed regardless of stratification. Moreover, the net alongshore bedload transport is higher during stratified conditions but the net alongshore suspended transport is smaller. Regarding the cross-shore sediment transport, the findings show that ambient stratification promotes onshore-directed bed- and suspended load net transport. The gross suspended transport rates are $\mathcal{O}(10^1)$ greater than the gross bedload transport rates.

SAMENVATTING

Dit proefschrift onderzoekt de effecten van gestratificeerde getijdestroming op de morphodynamica van het Nederlandse continentale plat. Het zuidelijke deel van het Nederlandse continentale plat wordt sterk beïnvloed door de ROFI (Region Of Fresh water Influence – regio van zoet water invloed) van de Rivier De Rijn, die wordt gegenereerd door de afvoer van de Rivier De Rijn via de Rotterdamsche Waterweg. Tijdens gestratificeerde condities, leidt de drie-dimensionale structuur in het getijdestromingspatroon tot een sterke kustdwarse schuifspanning zodat de stroming aan de bodem en aan het oppervlak 180° uit fase geraken. De schuifspanningsstroming gecreëerd door de stratificatie is aanwezig op het continentale plat en de kustoever en de verwachting is dat de bijbehorende stromingsasymmetrie een effect heeft op de morphodynamica. Echter, de rol van gestratificeerde getijdestroming op de morphodynamica langs de Nederlandse kust is veelal verwaarloosd of overgesimplificeerd. Dit proefschrift streeft ernaar binnen deze context nieuwe inzichten te verschaffen op welke wijze de gestratificeerde getijdestroming de morphodynamica buiten de brandingszone aanstuurt.

De Zandmotor is een experimentele mega-suppletie van 21,5 miljoen m^3 die in 2011 langs de Nederlandse kust is aangelegd. Deze interventie creëerde een discontinuïteit in de eerder rechte zandige kustlijn, die de lokale hydrodynamica veranderde in een gebied dat onder invloed staat van de ROFI. Schattingen van de centrifugale versnellingen direct na aanleg van de Zandmotor toonden aan dat de bochteffecten van significante invloed waren. Dit suggereert dat de Zandmotor een belangrijke rol zou kunnen hebben gespeeld in het beheersen van de kust-dwarse uitwisselingsstromen gedurende de eerste drie jaar na de voltooiing van de suppletie. Momenteel zijn de krommingseffecten zwak als gevolg van de morphodynamische ontwikkeling van de zandmotor. Observaties tonen de ontwikkeling van sterke baro-klinische kust-dwarse uitwisselingsstromen, geforceerd door zowel de rivierwater pluim als de klassieke getijschuifstroming. Deze stromingen en bijbehorende stratificatie strekken zich uit tot in de kustnabije zone (12 tot 6 m diepte), een gebied dat normaal gesproken beschouwd wordt als een gemengde zone.

Op het continentale plat zijn golven net zo effectief in het mobiliseren van sediment als de andere optredende stromingen. De invloed van stratificatie op de hydrodynamica wordt vertaald middels een schuifspanning in de laag direct boven de zeebodem. De getij-geïnduceerde bedschuifspanning is in staat om het bed regelmatig in beweging te brengen tijdens de maximum vloed en eb getijsnelheden en dan met name tijdens springgetijden. Resultaten van observaties suggereren dat onder gestratificeerde condities relatief hoge bed schuifspanningen worden uitgeoefend voor langere tijdperioden. De resultaten toonden ook aan dat andere stromingen, zoals wind-geïnduceerde stroming, een rol spelen in het controleren van de bodem mobiliteit. Echter, golf-geïnduceerde bedschuifspanning in het algemeen krijgt het sediment niet in beweging gedurende rustige weersomstandigheden en derhalve beperkt de opwerpende rol van golven zich tot stormsituaties.

De co-existerende bodemnabije stromingen op het continentale plat zijn verantwoordelijk voor het vormen van de zeebodem waarbij de resulterende bedvormtypen belangrijke informatie kunnen leveren over de hydrodynamische forceringen die de sediment mobiliteit bepalen. Waarnemingen tonen aan dat 59% van de ribbels op het continentale plat worden geclassificeerd als stroom ribbels. Golfribbels (3%) treden alleen op tijdens storm condities. De frequentie van voorkomen van transitionele bedvormen bedraagt 23%. Slecht ontwikkelde ribbels vinden vooral plaats gedurende doodtij situaties, daarmee representatief voor 15% van de waargenomen bedtypen. De terugkoppeling van de verschillende bedvormtypen naar de bovenliggende grenslaag speelt een fundamentele rol in de dynamica van de sediment load.

De morfologische respons van de bodem op de gestratificeerde en niet-gestratificeerde getijdestroming veroorzaakt verschillen zowel in de ribbelmigratie als ook in de sediment transport modi (bedload en suspensie load). De bedvormen op de meetlocatie staan onder sterke invloed van het getij zodat hun gedrag niet alleen dood en springtij invloed maar ook een dubbeldaagse getijde-involed laat zien. Onder de invloed van de ROFI, reduceren de gemiddelde bedform dimensies (ribbel hoogte en golflengte), hetgeen een indicatie is dat hun ontwikkeling wordt beïnvloed door de gestratificeerde getijstroming. Wanneer stratificatie ontbreekt zijn de getijde ribbels meer ontwikkeld in termen van hoogte en lengte. Het netto kustlangse bedload transport is zuidelijk gericht, terwijl de netto kustlangse suspensie load noordelijk gericht is, ongeacht de stratificatie. Bovendien, de netto kustlangse bedload load is groter gedurende stratificatie maar het netto kustlangse suspensie transport is lager. De resultaten laten zien dat de aanwezigheid van stratificatie kustwaarts transport

van zowel de bed als suspensie load bevordert en dat het bruto suspensie transport $\mathcal{O}(10^1)$ groter is dan bedload transport.

INTRODUCTION

1.1 CONTEXT

Coastal areas can be defined as the interface between the terrestrial and marine environments connecting the open ocean with the continental land masses. This system is highly sensitive to impacts of different types acting over a variety of spatiotemporal scales. The shoreline and its seaward extension (the shoreface profile) are constantly adjusting to fluctuations of environmental forcings (e.g., tidal regime, wave climate, storms and sea-level) by means of sediment movement. In many cases, those fluctuations can lead to acute or chronic erosion [Cowell et al., 2003b]. Acute erosion is normally driven by episodic or extreme events, for instance storms and tsunamis which can cause vast catastrophes. Chronic erosion is related to systematic trends that continuously push the system away from its equilibrium which, for example, can be a result of sea-level cycles or changes in the wave climate.

Besides, the ever increasing utilization of coastal zone resources results in a high socio-economic pressure [Nicholls et al., 2007] as the rapid human intervention (e.g., due to the exploitation of natural resources and recreational activities) interferes with the genuine coastal dynamics which, in combination with natural forces, exacerbates negative impacts like structural erosion. Consequently, special attention has been paid to coastal protection over the last 50-60 years in order to mitigate potentially short- and long-term hazardous effects [Dean and Dalrymple, 2004].

In low-lying lands like the Netherlands, the coastal system is substantially more susceptible to natural and anthropogenic impacts. Owing to this vulnerability, the Dutch government has actively maintained the coastline at its position since 1990 preserving the sand volume from +3 to -20 m NAP (Dutch Ordnance Level). To achieve this, additional sand supply (normally referred to as nourishment) has been

artificially placed in the Dutch coastal zone as the principal mitigation measure since then. This mitigatory intervention has been successfully protecting the Dutch coast over many years.

Recently, an innovative technique of a localized nourishment was implemented on the coast of the province of South-Holland in the Netherlands. This coastal intervention, known as the Sand Engine (Fig.1.1), or *Zandmotor* (in Dutch), was a 21.5 Mm^3 hook-shaped nourishment with $2.5 \times 1 \text{ km}$ of initial dimensions in the along- and cross-shore directions, respectively [Stive et al., 2013]. Future beach nourishments with the dimensions of the Sand Engine are likely to be constructed more often as it is believed to be more environmentally friendly and efficient in terms of sand redistribution. Such approach is within the “Building with Nature” framework [de Vriend et al., 2015] which has been gaining ground in fighting coastal erosion around the globe. This requires a solid understand of the governing forces that control the morphodynamics of the coastal system as the seaward protrusion of Sand Engine-like nourishments can extend beyond the isobath of 10 m depth. Thus, the morphodynamics of the deeper section of the coastal system, commonly defined in the literature as inner shelf or shoreface, with depths ranging from -8 to -20 m NAP , should also receive attention in projects of large nourishments. However, relatively low importance has been given to the dynamics of the sediment transport of the Dutch inner shelf [Vermaas, 2010].

1.2 THE IMPORTANCE OF THE INNER SHELF

The importance of the inner shelf lies on its coupling mechanism connecting different scales of processes that take place in the mid-shelf and the littoral zone. In other words, the inner shelf modulates the processes that operate in its neighboring realms and therefore it is expected to play a crucial role in the coastal sediment budget, especially when time-varying scale processes that induce systematic trends are considered [Stive and de Vriend, 1995, Cowell et al., 2003a].

The inner shelf undergoes active response due to forces imposed by the action of tides, wind-induced currents, non-breaking waves and, if present, river plume fronts (Fig.1.2). The multitude of the environmental agents acting in combination to dictate the sediment transport depends on the characteristics of a particular coastal system [Wright, 1977, Kleinans, 2002]. In the presence of a coastal river plume, also referred to as ROFI (Region Of Freshwater Influence), the vertical structure of the

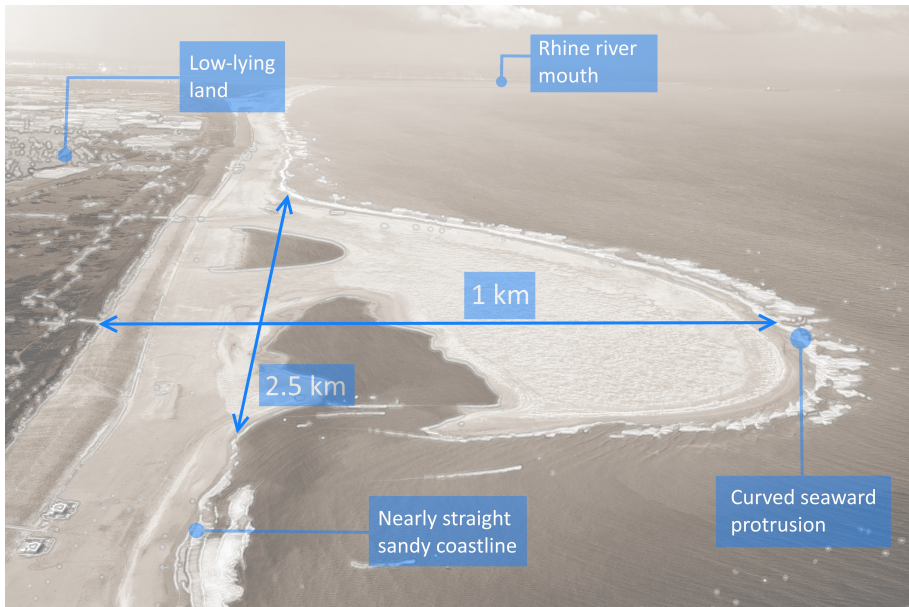


Figure 1.1: The Sand Engine a few months after its construction. Picture courtesy of Rijkswaterstaat/Joop van Houdt.

tidal currents is decoupled into two counter-rotating layers [Visser et al., 1994, Horner-Devine et al., 2015]. This mechanism, that results from the stratification created by the freshwater input, operates in the inner shelf and nearshore zones and has been found to contribute significantly to the fine sediment dynamics off the South-Holland coast [Flores et al., 2017, Horner-Devine et al., 2017]. However, the impact of the Rhine ROFI dynamics on the transport of the coarse sediment fraction (sand) as well as the seafloor (bedforms) dynamics is still poorly understood.

The sediment transport in the Dutch inner shelf has been investigated in previous studies within different frameworks [e.g. Van Rijn, 1997, Walstra et al., 1998, van de Meene and Van Rijn, 2000, Grasmeyer et al., 2006, Kleinhans and Grasmeyer, 2006]. Although significant advances have been achieved with respect to the inner shelf morphodynamics [e.g. van Rijn, 2005], the role of the stratified tidal flow on the sediment transport along the Dutch coast has been neglected or oversimplified. This can lead not only to discrepancies in results as discussed, for example, by Kleinhans and Grasmeyer [2006] but also to misinterpretation of physical processes. For example, the necessity to maintain the sand volume until the depth contour of -20 m is not entirely based on firm physical arguments due to the lack of information on the governing

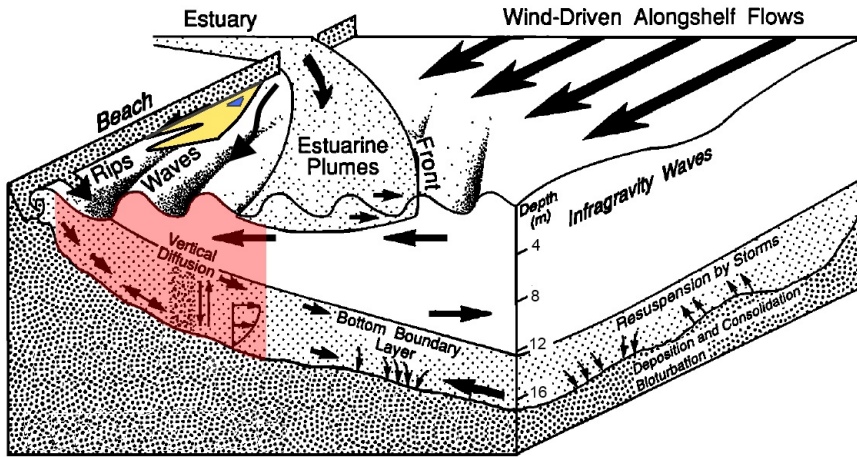


Figure 1.2: Illustrative sketch of the processes that drive morphological changes in the inner shelf (highlighted in red). Modified from: Wright [1995].

processes that operate on the Dutch inner shelf. Consequently, decision makers are led to adopt more conservative and thus less cost-effective solutions concerning the preservation of the coastline.

1.3 OBJECTIVES

Based on a newly collected dataset that is specifically meant to examine the effects of the stratified tidal flow on the morphodynamics of the Dutch inner shelf, the present investigation centers on the physical mechanisms that drive the seafloor (bedforms) dynamics and its intrinsic sediment transport under the influence of the Rhine river ROFI. Thus, the following hypothesis is formulated:

Hypothesis

The stratified tidal flow modifies the geometry and dynamics of small scale bedforms and thereby affects the bedload and suspended load sediment transport.

To test this hypothesis the following research questions (RQs) are addressed:

Research Question 1 - RQ1 (Chapters 2 and 3)

To what extent does the stratified tidal flow control the inner shelf hydrodynamics?

RQ1.1 *What is the impact of the Sand Engine on the stratified tidal flow?*

RQ1.2 *What is the contribution of the different terms of the momentum equation to the cross-shore flow?*

RQ1.3 *What is the shoreward extent of the stratified cross-shore flow?*

RQ1.4 *How does stratification affect the bed shear stress?*

Research Question 2 - RQ2 (Chapter 4 and 5)

How does the near-bed stratified tidal flow affect the bedform dynamics and sediment pick-up from the seafloor?

RQ2.1 *What bed form types are found off the South-Holland coast?*

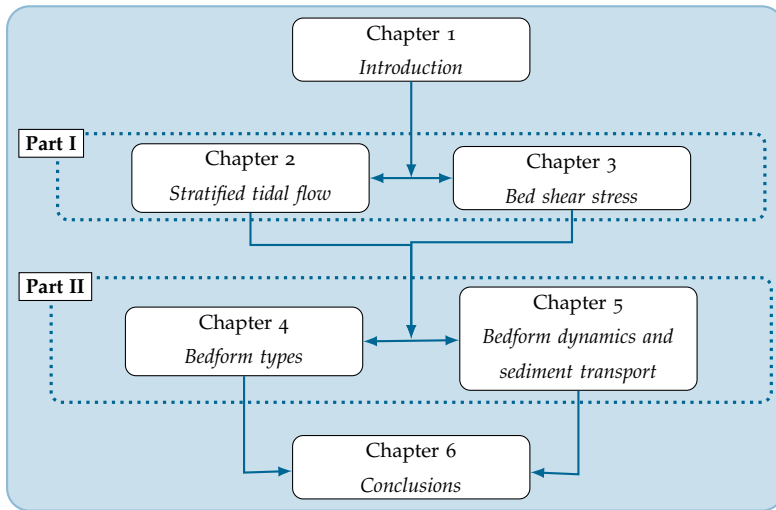
RQ2.2 *Which mechanisms control the bedform dynamics under stratified conditions?*

RQ2.3 *How does stratification impact the bedform migration rates?*

RQ2.4 *How does bedform dynamics affect the sediment transport modes?*

1.4 OUTLINE

This thesis is structured in six chapters divided in two main parts as outlined in the diagram below. The first part discusses the hydrodynamics and its association to sediment transport by means of bed shear stress (Chapters 2 and 3). The morphodynamics are discussed in the second part which includes Chapters 4 and 5. Chapter 6 verifies the hypothesis of this thesis by addressing all the findings and summarizes the main conclusions.



Part I

HYDRODYNAMICS

Observations of the tidal flow reveals a remarkable influence of stratification on the hydrodynamics. The Sand Engine curvature plays a secondary role on the cross-shore tidal dynamics which is strongly dictated by stratification. The near-bed flow translates the influence of stratification on the tidal flow in bed shear stress which ultimately impacts the sediment transport. The tide-induced bed shear stresses are dominant in the Dutch inner shelf.

CROSS-SHORE STRATIFIED TIDAL FLOW

This chapter is based on the publication: S. Meirelles, M. Henriquez, A. Reniers, A. P. Luijendijk, J. Pietrzak, A. R. Horner-Devine, A. J. Souza, and M. J. F. Stive. Cross-shore stratified tidal flow seaward of a mega-nourishment. Estuarine, Coastal and Shelf Science, 200:59 – 70, 2018b. ISSN 0272-7714. doi: <https://doi.org/10.1016/j.ecss.2017.10.013>

2.1 INTRODUCTION

In 2011, a localized mega-nourishment was implemented on the South-Holland coast, the Netherlands. This unique type of coastal protection, referred to as the Sand Engine or *Zandmotor* (in Dutch), was built in the shape of a hooked peninsula of 21.5 Mm³ of sand with initial dimensions of 2.5 × 1 km in the along- and cross-shore directions respectively [Stive et al., 2013] (Figure 2.1). The Sand Engine is intended to naturally nourish the 17 km-long adjacent coast over a 20-year period, providing an environmental and economic solution to systematic coastal erosion. Despite being a soft-engineering intervention, the Sand Engine created a sharp discontinuity in the previously nearly alongshore uniform coast, which altered the typical hydrodynamic regimes [Huisman et al., 2016, Radermacher et al., 2016].

This artificial peninsula that characterizes the Sand Engine is expected to promote curvature-induced flow similar to that reported in the literature on river bend currents [e.g., Bathurst et al., 1977, Odgaard, 1986], flow around headlands [e.g., Gerret and Loucks, 1976, Geyer, 1993] and circulation in curved estuaries [e.g., Chant and Wilson, 1997, Lacy and Monismith, 2001]. Huisman et al. [2016] and Radermacher et al. [2016] have found that the alongshore barotropic tidal flow is substantially impacted by the Sand Engine as a result of flow contraction around the tip of the Sand Engine and flow separation at its flanks, however no information on the cross-shore (baroclinic)

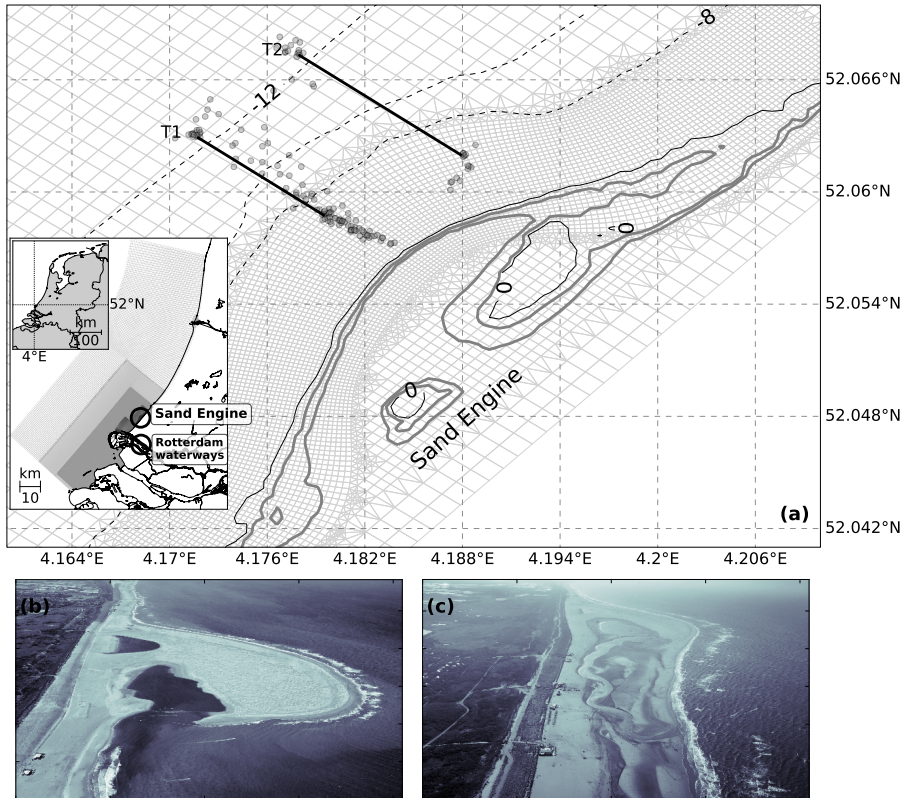


Figure 2.1: Study area location. (a) The inset shows the location of the Holland Coast, the Sand Engine and the Rotterdam waterways within the Netherlands; (b) the Sand Engine a few months after its completion; and (c) the Sand Engine during the field experiment in Sep 2014 (Courtesy of Rijkswaterstaat/Joop van Houdt). The transects crossed the isobaths from approximately -12 to -8 m. The gray circles show the location of the 153 CTD casts. The Delft3D-FM computational grid is also shown as a reference.

flow is provided. Because the barotropic alongshore (streamwise) current is deflected towards the outer bend, an imbalance between the depth-varying centrifugal acceleration and the cross-shore (cross-stream) pressure gradient is created, resulting in the development of cross-shore exchange currents (also referred as lateral, secondary or transverse flow). The cross-shore exchange currents are seaward-directed near the surface (towards the outer bend) and landward-directed near the bottom [Drinker, 1961]. Such a pattern plays a role in the sediment transport, for example in rivers and estuaries where lateral sediment trapping has been observed due to curvature effects in combination with density gradients and Coriolis forcing [Geyer et al., 1998, Hui-

jts et al., 2006, Fugate et al., 2007]. Therefore, a clearer understanding of the role of curvature-induced cross-shore flow off the Sand Engine is important so as to evaluate if there is any feedback between the curvature of the shoreline perturbation and the evolution of the coastal profile.

Hydrodynamics along the South Holland coast are strongly influenced by the Rhine River ROFI (Region Of Freshwater Influence), which is generated by the discharge from the Rhine River through the Rotterdam waterways. Previous studies have described a pronounced baroclinic cross-shore circulation along the Dutch coast, in regions where the water column is stratified [Van der Giessen et al., 1990, Visser et al., 1994, De Boer et al., 2009]. The cross-shore baroclinic pressure gradient is the main driver of the cross-shore exchange currents controlling the orientation of the cross-shore circulation which switches every low water (LW) and high water (HW), owing to the effects of the cross-shore tidal straining [Souza and James, 1996]. Tidal straining is a mechanism that results from the interaction of the vertical tidal shear and the horizontal density gradient, being responsible for inducing the semidiurnal switching of stratification [Simpson et al., 1993, 2005]. As a result of straining, the Rhine ROFI is advected shoreward from HW to LW, whereas it is advected seaward from LW to HW [De Boer et al., 2008]. The current structure and dynamics of river plumes has been studied extensively by Horner-Devine et al. [2015], however little attention has been paid to the modification of plume dynamics by coastline protrusions or the influence of the curvature-induced dynamics described above.

In general, the interaction between centrifugal acceleration and baroclinic pressure gradient may enhance or suppress the development of the cross-shore exchange currents. For example, the observations of Chant and Wilson [1997] near a headland in the Rudson River estuary revealed that the cross-shore density gradients weakened the centrifugally-induced flow resulting in an increase of the Ekman spin-down time of the tidally-generated eddies further downstream. Becherer et al. [2015] found, in the German Wadden Sea, that this interaction enhances the cross-shore exchange currents during flood and suppresses it during ebb. In the Marsdiep tidal inlet, the Netherlands, Buijsman and Ridderinkhof [2008] observed that the cross-shore exchange currents are mostly controlled by the centrifugal acceleration during flood and baroclinic forcing during ebb. In the Rhine ROFI system, under hypothetical conditions, the interplay between classic tidal straining and the centrifugal acceleration seaward of the tip of the Sand Engine should enhance the cross-shore exchange currents from LW to HW and diminish it from HW to LW as schematized in Figure 2.2. The verification of this hypothesis is discussed further in this work.

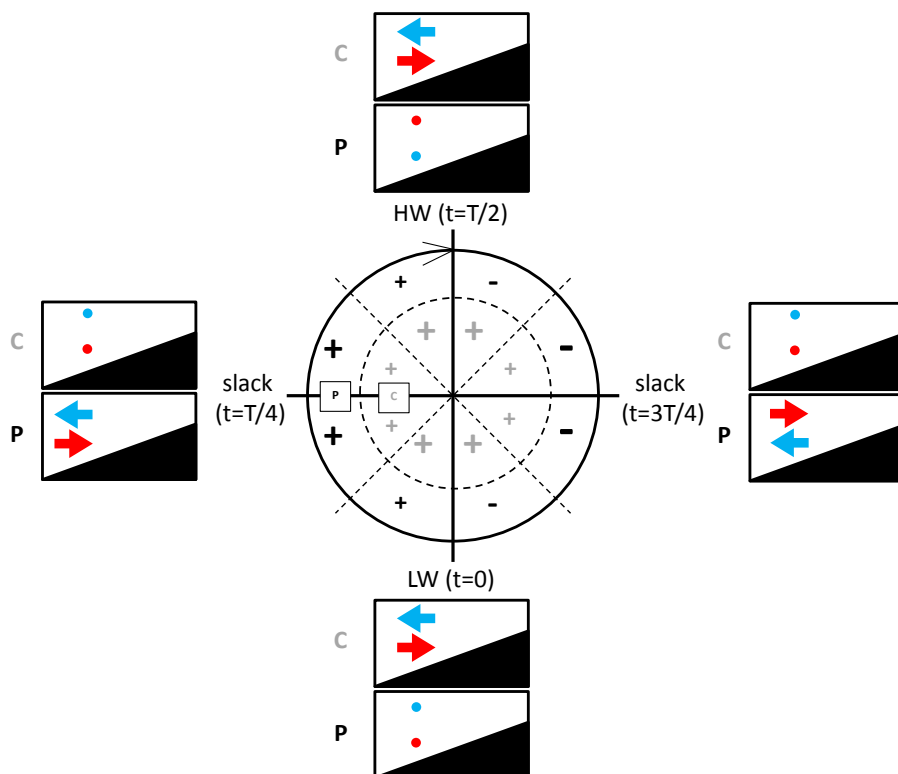


Figure 2.2: Idealized interplay between baroclinic pressure gradient (P) and centrifugal acceleration (C) along a cross-shore profile off the tip of the Sand Engine. The plus and minus signs indicate positive and negative vertical shear in the cross-shore (see text for explanation), their colors indicate the terms P (black) and C (gray) and their size indicate the magnitude. The panels show the cross-shore distribution of the cross-shore exchange currents generated by P and C. Blue arrows are offshore-directed and red arrows are onshore-directed. The colored dots indicate when the cross-shore currents are nearly zero.

While there is established knowledge on cross-shore exchange currents, it is still uncertain how they occur around protruding beach nourishments. The Sand Engine, due to its unprecedented dimensions, provides a unique opportunity to gain insight on how cross-shore exchange currents interact with this type of coastal intervention which has an erodible character. Furthermore, knowledge about the hydrodynamics is indispensable for understanding the evolution and role of the Sand Engine in nourishing the coast.

This paper investigates the cross-shore exchange currents around the Sand Engine in the light of the major mechanisms responsible for controlling the cross-shore current structures. The main research question is: what is the response of the cross-shore stratified tidal flow to the perturbation created by the Sand Engine? Therefore, the interplay between baroclinic forcing and centrifugal acceleration on the development of cross-shore exchange currents is examined. The objective is addressed through field measurements detailing the structure of the velocity and density fields immediately offshore of the Sand Engine.

2.2 STUDY AREA

The Sand Engine, built in 2011 with initial volume of 21.5Mm^3 of sand, is located along a sandy 17 km stretch of the Dutch coast that is otherwise relatively straight (Figure 2.1). This domain has its southern limit bounded by the Rotterdam waterways where the Rhine River discharges an average of $2200\text{m}^3\text{s}^{-1}$ of fresh water into the North Sea. The northern boundary is marked by the jetties of Scheveningen harbor.

The Sand Engine, which originally extended 1 km into the North Sea, has evolved dramatically since it was built. Within the first 2.5 years, the mega-nourishment redistributed 2.5Mm^3 of sand [De Zandmotor, 2014] so that its morphology has consequently been changed from a hook shape into a Gaussian shape [de Schipper et al., 2016] (Figure 2.1a and c). Currently, the Sand Engine extends 0.3 km perpendicular to the original coastline and 5 km in the alongshore. Evidently, the impact on the local hydrodynamics has reduced through this evolution and hence the curvature effects have also diminished. Below we describe the hydrodynamics in this region in the absence of the bathymetric perturbation associated with the Sand Engine.

The tide behaves as a Kelvin wave propagating from South to North along the Dutch coast so that the peak of flood currents coincides with HW so does the peak of ebb currents with LW. The orientation of tidal ellipses generally follows the isobaths [Van der Giessen et al., 1990]. The semi-diurnal band, which is dominated by the M_2 constituent, holds about 90% of the variance of the tidal signal. The near surface M_2 amplitude ($\approx 4\text{ m}$ below the surface) increases seaward over a cross-shore distance of about 10 km (from ≈ 55 to $\approx 60\text{cms}^{-1}$), while the near bottom amplitudes ($\approx 4\text{ m}$ above the bottom) decreases (from ≈ 43 to $\approx 32\text{cms}^{-1}$) [Visser et al., 1994]. The peak of flood and ebb currents fluctuates typically 30% over an entire spring-neap cycle

[Visser et al., 1994]. The largest shallow-water constituent in the northeast European shelf is the M_4 with average amplitudes higher than 8 cm [Andersen, 1999].

In the North Sea, the vertical structure of the tidal current is affected by differences in eddy viscosity over depth owing to stratification [Maas and Van Haren, 1987]. Visser et al. [1994] demonstrated how the suppression of turbulence at the pycnocline leads to a significant increase of the cross-shore tidal current that can reach 35 cm s^{-1} in the Rhine River ROFI. The later investigation from Souza and Simpson [1996] confirmed the enhancement of the cross-shore amplitudes by showing that the tidal current ellipses develop a more circular pattern with the onset of stratification.

Van der Giessen et al. [1990] observed a large variability of residual currents along the Dutch coast which closely correlates with fluctuations of the wind field on time scales of days to weeks. If persistent, northeasterly winds can enhance stratification, while southwesterly winds favor mixing [Souza and James, 1996]. The results presented by Souza and Simpson [1996] showed that winds are the main agent in controlling stratification in the Rhine region of influence. The stability of the vertical density structure is also dictated by tidal and wave stirring [Souza and Simpson, 1997].

The wave climate along the Dutch coast is dominated by wind-sea waves. Under typical conditions, they approach the coast from the western quadrant and swell is primarily from northwesterly direction due to the geometry of the North Sea [Wijnberg, 2002]. The nearshore wave climate varies considerably and is characterized by waves of moderate height and short period [Van Rijn, 1997]. The wave action on the South-Holland coast is the main driver of the Sand Engine evolution followed by the tidal flow [Luijendijk et al., 2017].

2.3 METHODS

A 13-hour field campaign was conducted to map the cross-shore current structures and the density field in order to investigate how the baroclinic forcing and centrifugal acceleration control the cross-shore exchange currents in the study area.

2.3.1 *Field campaign*

The measurement of current velocities was conducted on October 17, 2014 over two transects perpendicular to the original (unnourished) coastline (Figure 2.1). Transect

1 (T1) was aligned with the tip of the Sand Engine and transect 2 (T2) was located at its northern flank. Concurrently, the density structure of the water column was measured at the beginning and the end of every transect. The sampling strategy envisioned to capture the mechanisms that generates cross-shore exchange currents on the time-scale of the semi-diurnal tide (≈ 12.5 h). The analysis of the balance between centrifugal acceleration and baroclinic forcing focuses on the T1 transect because it is radial to the Sand Engine curvature.

An ADCP Workhorse 600 KHz, looking downward, with sampling frequency of 0.6 Hz, was mounted on a boat and integrated into a DGPS system able to correct accurately for the pitch, roll and heading. The ADCP's main axis pointed 45° to the boat's bow allowing all beams to detect a similar magnitude of Doppler shift with the aim of increasing accuracy [Raye and Driscoll, 2002]. The ADCP was positioned 1 m below the waterline.

During a semi-diurnal tidal cycle, the boat navigated over the transects in a clockwise direction at a speed of about 2 ms^{-1} . The transects were 640 m apart from each other so that the surveying time of two consecutive transects was short enough that the statistical distribution of the tidal flow did not significantly change within this interval. Both transects had their offshore and onshore limits roughly between the isobaths of -12 and -5 m, respectively. The ADCP was set to measure over 20 m depth with a vertical resolution of 0.5 m comprising 40 measurement cells.

The density profiles were obtained with a Castaway-CTD. This instrument features built-in GPS that gives the geographic position. The CTD sampled at 5 Hz which provided enough vertical resolution to capture vertical density stratification associated with the Rhine River plume at the site. From 1100H to 1500H, additional CTD casts were carried out from a jet-ski to increase the cross-shore resolution at T1.

2.3.2 ADCP data processing

The ADCP dataset consists of 56 transect repetitions and the average time between each repetition was 24 minutes. The velocities measured at T1 and T2 were rotated to a coordinate system aligned with the main coastline orientation of 42° . Thus the cross-(u) and alongshore (v) components of the velocities could be resolved. Subsequently, a moving average with a window of 3 profiles was applied to reduce noise. The navigated transects were projected onto reference transects T1 and T2 through the inverse distance weighting method that spanned over the two closest neighbors. This

procedure was repeated for each depth creating a 2D grid with horizontal and vertical resolution of $\Delta x = 0.7$ m and $\Delta z = 0.5$ m, respectively.

Following the analysis of Valle-Levinson et al. [2015], the M_2 tidal constituent was extracted from the series of horizontal velocities by using least-squares-based harmonic analysis [Codiga, D. L., 2011] in which the velocities were represented as complex numbers ($u + iv$). Later the data was smoothed by applying a moving average with 90 m window along the transects. In addition, the remaining spurious values, i.e spikes, were manually removed from the series.

2.3.3 Tidal current ellipses

Because the properties of the vertical structure of the M_2 tidal current ellipses are modified by stratification [e.g., Souza and Simpson, 1996, van Haren, 2000], the ellipse parameters were calculated. These were derived from the complex velocities which were decomposed, for a specified frequency, into cyclonic and anti-cyclonic circular components with amplitudes W_{\pm} and phases θ_{\pm} [Thomson and Emery, 2014]. The semi-major axis (U), phase angle (ϕ) and the ellipticity (also referred to as eccentricity) (ϵ) of the ellipses are expressed, respectively, by:

$$U = W_+ + W_-, \quad (2.1)$$

$$\phi = (\theta_- - \theta_+)/2, \quad (2.2)$$

$$\epsilon = (W_+ - W_-)/(W_+ + W_-). \quad (2.3)$$

The semi-major axis indicates the maximum current velocity, the phase defines the time taken to reach the maximum current, the ellipticity determines if the tidal motion is rectilinear ($\epsilon = 0$; i.e the semi-minor axis of the tidal ellipses have a negligible amplitude) or circular ($\epsilon = 1$) and the sign of the ellipticity provides the sense of rotation (negative is anti-cyclonic and positive is cyclonic).

2.3.4 Cross-shore exchange currents

In order to evaluate the impact of the Sand Engine's curvature on the hydrodynamics, it is necessary to compare the cross-shore exchange currents generated by centrifugal

acceleration with those induced by baroclinic forcing. We will make this comparison based on the two-layer momentum balance described below.

The dynamics of the cross-shore exchange currents associated with curvature are commonly analyzed through the approach by Kalkwijk and Booij [1986] who presented an analytic solution for the momentum balance equation for curved flows. This method determines the generation of secondary flow that is forced by curvature as well as Coriolis acceleration. The reduction of the eddy viscosity, A , by stratification is not accounted for, which may modify the strength of the cross-shore exchange currents as reported by Geyer [1993].

To examine the role of stratification on the cross-shore exchange currents, Seim and Gregg [1997] included the baroclinic pressure term in the secondary flow governing equation of Kalkwijk and Booij [1986]:

$$\frac{\partial u}{\partial t} + v \frac{\partial u}{\partial y} + \frac{v^2 - \langle v^2 \rangle_z}{R} = -\frac{g}{\rho_0} \int_z^0 \frac{\partial \rho}{\partial x} dz + \frac{g}{\rho_0} \frac{\partial \langle \rho \rangle_z}{\partial x} h + \frac{\partial}{\partial z} \left(A \frac{\partial u}{\partial z} \right) + \frac{\tau_b}{\rho h}, \quad (2.4)$$

where x , y and z denote the cross-shore, alongshore and vertical coordinates, respectively. R is the local radius of curvature and h is the water depth. Depth-averaged quantities are denoted by $\langle \rangle_z$. The acceleration due to gravity is represented by g , ρ_0 is a constant reference water density, ρ is the seawater density and τ_b is the cross-shore bottom stress.

Seim and Gregg [1997] scaled Equation 2.4 by assuming a steady balance between centrifugal acceleration and the cross-shore (or cross-channel) baroclinic pressure gradient, simplifying it to:

$$\frac{v^2 - \langle v^2 \rangle_z}{R} = -\frac{g}{\rho_0} \int_z^0 \frac{\partial \rho}{\partial x} dz + \frac{g}{\rho_0} \frac{\partial \langle \rho \rangle_z}{\partial x} h. \quad (2.5)$$

The omission of frictional forces in Equation 2.5 was justified by considering the relative importance of advection to friction. The ratio of these terms is defined as $R_{ef} = h/LC_D \sim v \frac{\partial u}{\partial y} / \frac{\tau_b}{\rho h}$, where R_{ef} is the equivalent Reynolds number, L is the alongshore (streamwise) length scale and C_D is the bottom drag coefficient and values of $R_{ef} > 1$ indicates that friction is of secondary importance [Alaee et al., 2004]. The values of R_{ef} were 1.68 ± 0.35 during our measurement period (not shown), confirming that advective processes prevailed over bottom friction and therefore we have left out the frictional terms. Given the dimensions of the Sand Engine, Coriolis acceleration is assumed to be irrelevant as the Rossby number, $2v/fR$, is greater than unity (≈ 3), i.e, curvature effects dominate over Coriolis.

To calculate the centrifugal acceleration (LHS of Equation 2.5), the ADCP velocities were first divided in two layers of equal height following the bathymetry of the cross-shore profile, then the centrifugal acceleration was computed and averaged over each layer separately. The values of the bottom layer were then subtracted from those of the top layer following the approach by Buijsman and Ridderinkhof [2008], eliminating the barotropic pressure gradient from the balance. Using this same two-layer approach, the baroclinic forcing (RHS of Equation 2.5) was calculated with the CTD data.

2.4 OBSERVATIONS

The measurements took place during neap tide which is the part of the spring-neap cycle typically characterized by strong stratification. This strong stratification results from the reduced vertical mixing due to tidal stirring that is generated by the weaker neap currents. The river discharge was about $1651 \text{ m}^3 \text{ s}^{-1}$ which is below the annual mean that is between 2000 and $2500 \text{ m}^3 \text{ s}^{-1}$. Winds and waves were approximately orthogonal to each other and developed a choppy sea state during the survey. Waves were measured by a wave buoy deployed at the site. The root-mean-squared wave height, H_{rms} , was slightly higher than 0.4 m throughout the survey and the wave direction was nearly perpendicular to the shore. The estimated mean Stokes drift was of 0.012 m s^{-1} near the surface and negligible near the bottom. The meteorological station in Rotterdam registered persistent SW winds fluctuating from 5 to 8 m s^{-1} . The estimated depth-averaged wind-generated current, based on the Ekman motion, was shore-directed with average speed of 0.044 m s^{-1} . Based on these estimations, the Stokes drift and wind-driven current were neglected in our the analysis of the cross-shore exchange currents.

The Stokes drift presented very small values and it did not contribute to the development of the cross-shore exchange currents. Regarding the role of the winds, they can significantly modify the flow and dynamics of the Rhine ROFI, however their directly influence on the development of the cross-shore exchange currents is still not well understood. Based on our calculations using the present dataset, the cross-shore exchange currents are strongly dominated by the density gradient and thus we anticipate that they are neither forced nor controlled by the winds.

The presence of cross-shore exchange currents is apparent from the vertical decoupling of the cross-shore component of the tidal currents (Figures 2.3e and f) marked by

a 180° phase shift from top to bottom. The maximum cross-shore currents occurred during the period of strong stratification reaching offshore and onshore velocities of -24 and 20 cms^{-1} , respectively. The observed cross-shore exchange currents extended to the shallower part of T1 (Figure 2.3g), although the cross-shore velocities were significantly smaller (-8 and 11 cms^{-1}). The vertical density structure and the velocities at T2 are also presented in Figure 2.3 for comparison purposes.

The alongshore component behaved as expected (i.e, with the characteristics of a progressive Kelvin wave) and therefore the alongshore tidal currents were approximately in phase with the water elevation (Figures 2.3a, b, c and d). The alongshore currents reached 66 cms^{-1} and -55 cms^{-1} during flood and ebb, respectively. The velocities observed at the shoreward limit of T1 were higher than those of T2, indicating the contraction of the tidal current as it flows around the tip of the Sand Engine [Radermacher et al., 2016].

The observed density structures showed a clear variability of strong vertical stratification from LW to HW (Figures 2.3i and k). After HW, the stratification started to weaken substantially, but the water column was not fully mixed. The water density near the bottom varied from 1020.80 to 1022.75 kgm^{-3} and from 1020.39 to 1022.08 kgm^{-3} at the seaward and shoreward limits of T1, respectively. Near the surface those values varied from 1020.04 to 1021.33 kgm^{-3} and from 1020.06 to 1021.59 kgm^{-3} .

The variability of the cross-shore density field is illustrated in Figure 2.4 for two distinct periods. The first is just after HW when water column was de-stratifying and the cross-shore velocity profile exhibited relatively strong offshore-directed velocities in the lower layer of the water column and onshore-directed velocities in the upper layer (Figure 2.4a). The second is during early ebb when the water column became slightly stratified again (Figure 2.4b) and the associated cross-shore velocity profile exhibited onshore-directed velocities in the lower layer of the water column and offshore-directed velocities in the upper layer. The variability of the density field is also captured by radar images that showed the recurrent presence of the plume front during the measurements (Figures 2.4c to f) and therefore vertical stratification was observed much of the time (Figures 2.4g to j).

The Richardson number, Ri , defined as the ratio of the buoyancy frequency, $N^2 = (-g/\rho_0) \partial\rho/\partial z$ to the squared vertical shear, $S^2 = (\partial u/\partial z)^2 + (\partial v/\partial z)^2$ (i.e, $Ri = N^2/S^2$), provides information on the competition between shear-driven mixing and vertical density stratification. Figures 2.5c and f show time series of the transformed Richardson number ($\log(4Ri)$) calculated for the offshore and onshore limits of T1.

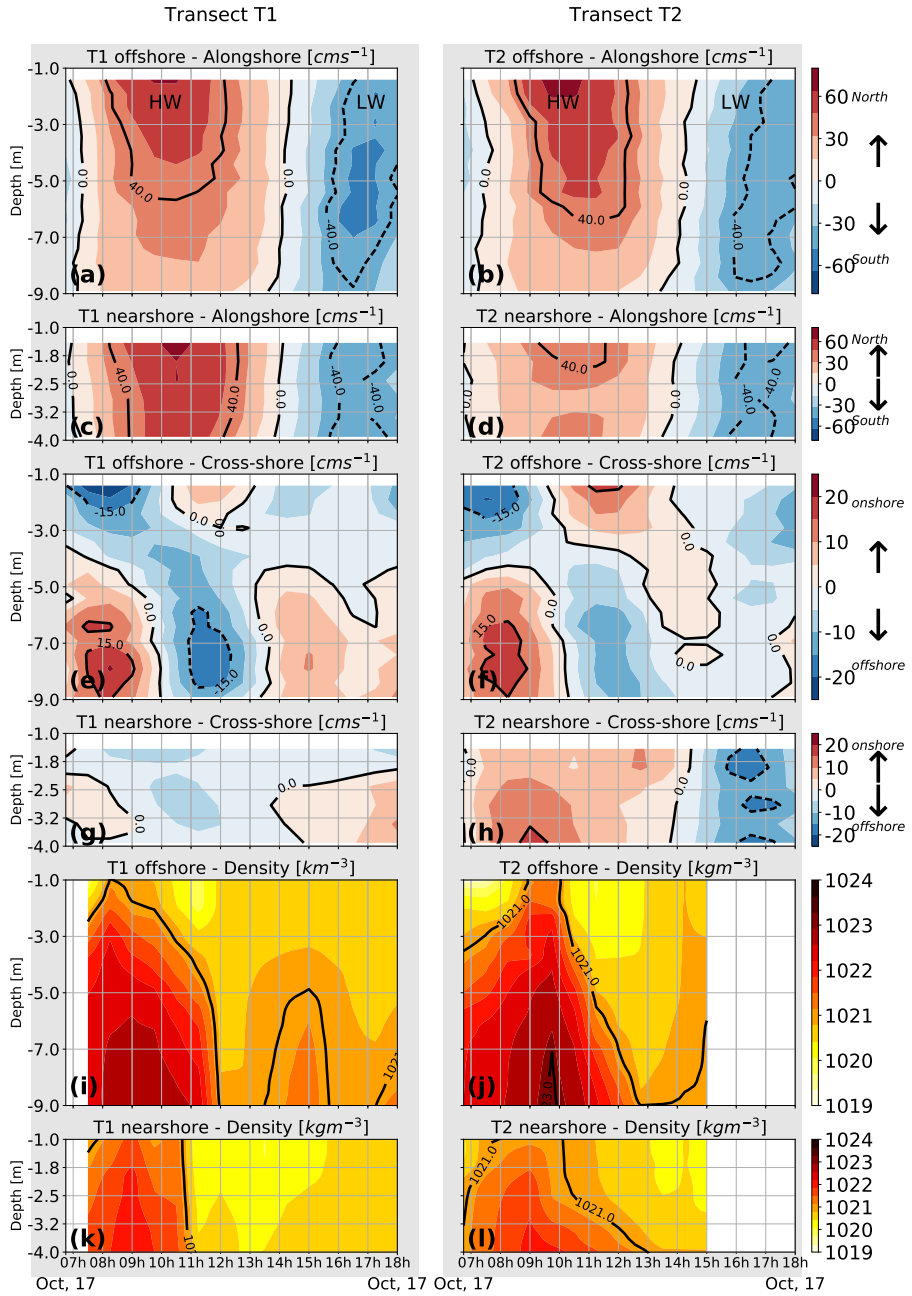


Figure 2.3: Time series of the observed cross- and alongshore profiles of the tidal velocities and density at the offshore (a, b, e, f, i and j) and onshore (c, d, g, h, k and l) limits of T1 (left) and T2 (right). The low water (LW) and high water (HW) tidal stages are indicated in (a) and (b). There is no CTD data after 1500H at T2 as seen by the blank space in (j) and (l).

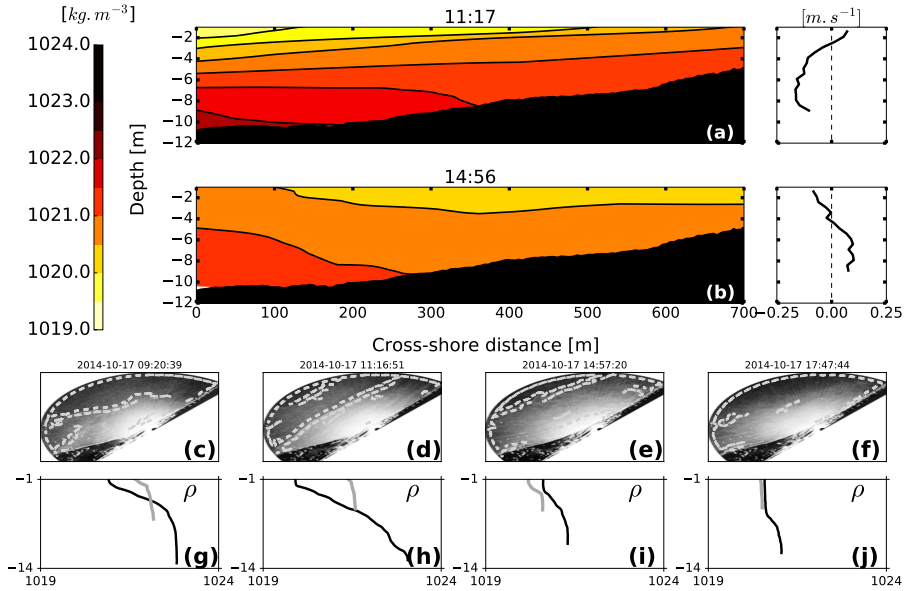


Figure 2.4: (a and b) Cross-shore density structure and the respective cross-shore velocity profiles at the seaward limit of T₁. (c to f) Radar images of the Northern flank of the Sand Engine during four distinct periods of the survey. The contours in the images show the edge of the plume front. (g to j) Density profiles taken at the offshore (black line) and nearshore (gray line) limits of T₁ for the same periods of the radar images.

The values of $\log(4Ri)$ were above the threshold for stability ($\log(4 \cdot 0.25) = 0$) most of the tidal cycle indicating a tendency for the development of stratification. Given this condition, the turbulent mixing tends to be reduced or, as Geyer et al. [1998] pointed out, the shear may be enhanced by stratification. The results showed moments of high vertical shear (Figures 2.5a and d) coinciding with the stratified period (Figures 2.5b and e) which may imply that shear is intensified by stratification, consistent with the model of Visser et al. [1994].

Figure 2.7 displays the vertical shear of the u component ($\partial u / \partial z$) computed with the M_2 tidal velocities averaged over 30 min bins. The vertical shear ranged from -0.24 to 0.16 s^{-1} in which negative and positive values indicate a tendency of counterclockwise (CC) and clockwise (CW) rotation in the vertical plane, respectively. From LW to HW, during the period of strong stratification, the cross-shore circulation tended to rotate in the CC direction. After HW, when stratification started to break down, the vertical shear changed sign, meaning that the sense of rotation of the cross-shore circulation tended to be in the CW direction. At about 1400H, the circulation changed

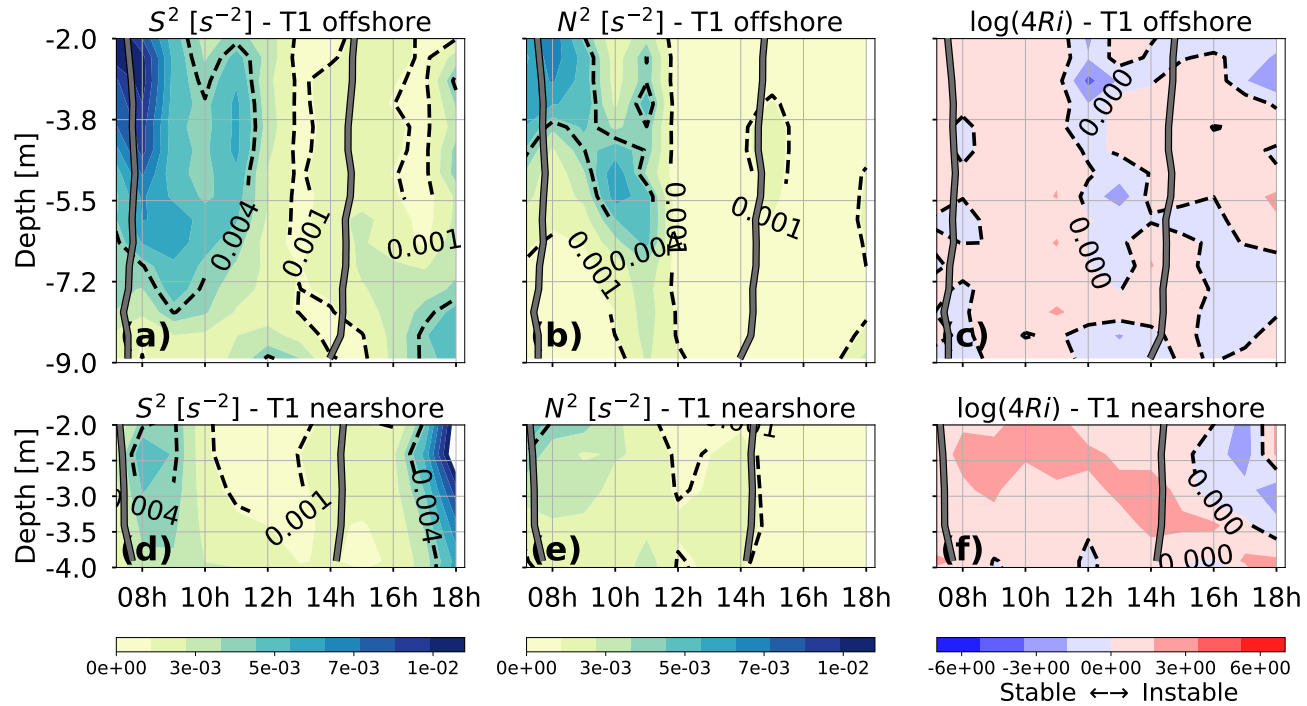


Figure 2.5: Time series of the squared vertical shear (S^2), buoyancy frequency (N^2) and the transformed Richardson Number ($\log(4Ri)$, where $Ri = N^2/S^2$) at the offshore (a, b and c) and onshore (d, e and f) limits of T1. The thick gray lines mark the HW and LW slacks (i.e., $v = 0$).

sign again so that it was predominately in the CC direction. This period coincides with the approximation of the plume front as shown by the radar images in Figure 2.4c to f.

The amplitude, phase and ellipticity of the M_2 tidal constituent derived from the harmonic analysis are shown in Figure 2.6. In general, the observed amplitudes and phases of the M_2 constituent were uniform throughout T1. The results for the ellipticity of the M_2 constituent showed an anti-cyclonic rotating ellipses near the surface and cyclonic rotating ellipses near the bottom all over the surveyed transect. These results agree with the findings of Souza and Simpson [1996] who reported changes of the tidal ellipse parameters over depth due to the influence of the Rhine ROFI. We additionally showed that the modification of the tidal ellipses in the presence of stratification can extend further into the nearshore.

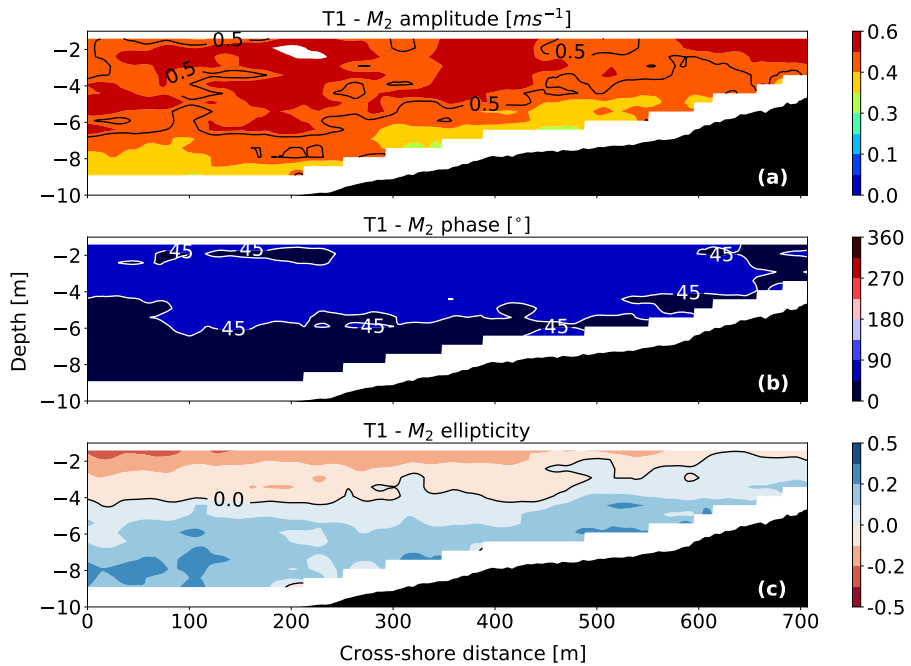


Figure 2.6: Main parameters of the M_2 tidal current ellipse at transect T1. (a) M_2 amplitude; (b) M_2 phase; (c) M_2 ellipticity.

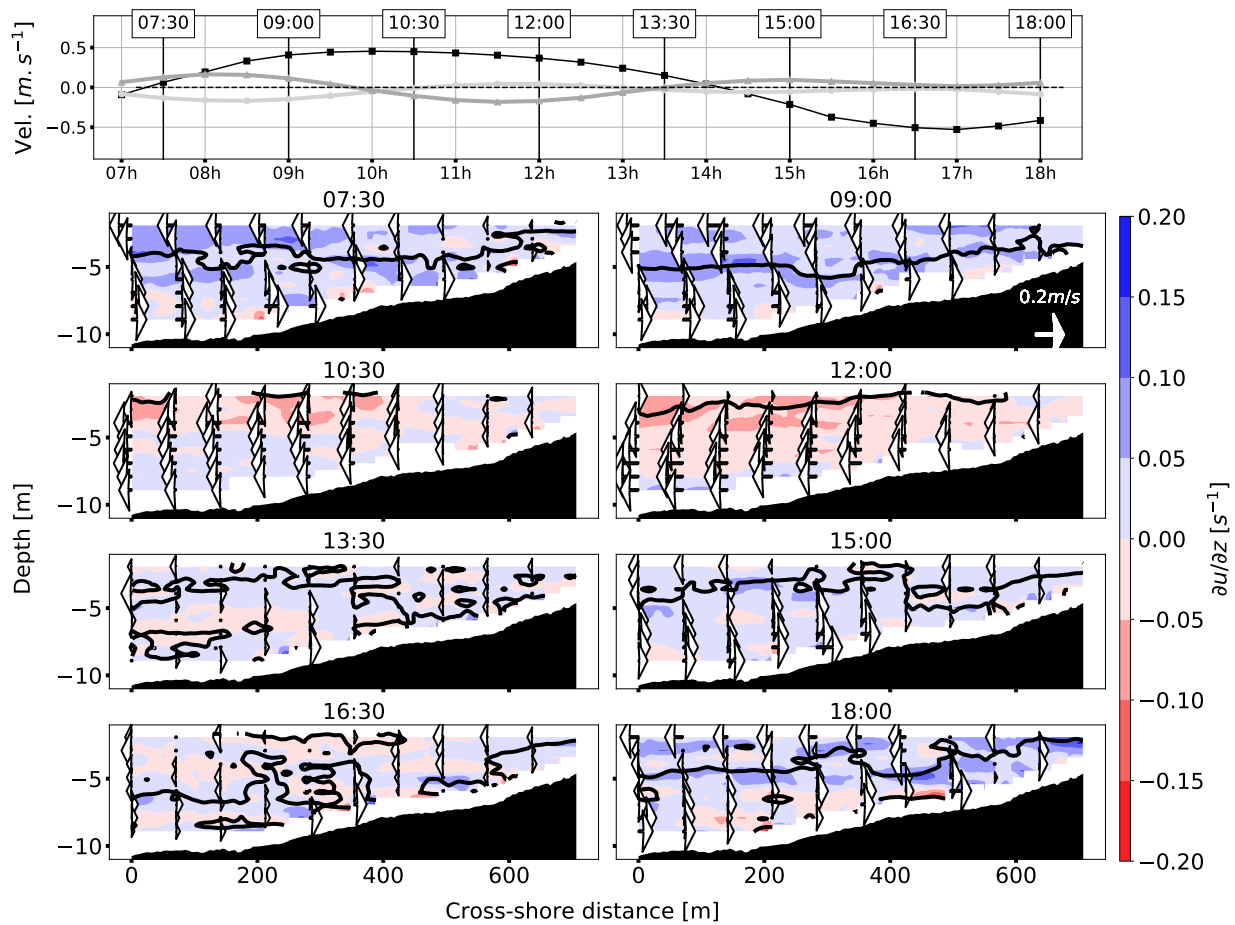


Figure 2.7: (Previous page.) Upper panel: Depth-averaged alongshore (black line) and cross-shore velocities near the bed (dark gray line) and near the surface (light gray line) velocities. The velocities were taken from the offshore limit of T1. Lower panel: vertical shear during 8 distinct periods over the tidal cycle. Negative values indicate a tendency to counterclockwise cross-shore circulation. The vectors represent the cross-shore velocities and the contour line indicates zero velocity.

2.5 DISCUSSION

The results from the observations presented in Section 2.4 identify the cross-shore current structures seaward of the Sand Engine along Transect T1. In this Section, the role of the density gradients and curvature in yielding cross-shore exchange currents is explored focusing on how the presence of the mega-nourishment results in changes of cross-shore circulation.

The strong vertical stratification captured in the measurements is part of the semi-diurnal switching of stratification that has been extensively investigated in the Rhine River ROFI [Visser et al., 1994, Simpson and Souza, 1995, Souza and Simpson, 1996, 1997, De Boer et al., 2006, 2008, 2009]. The present work showed that this mechanism extends to the nearshore zone (up to ≈ 6 m depth) despite the perturbation of the tidal flow caused by the Sand Engine as well as the stirring by wind and waves, which are expected to maintain the nearshore zone permanently well-mixed as suggested by De Boer et al. [2009]. The observations revealed a close association between stratification and the cross-shore flow (Figure 2.3). The semi-diurnal variability of the density field is attributed to classic cross-shore tidal straining due to the two-way interaction between the horizontal density gradient and the counter-rotating tidal ellipses, resulting in the semidiurnal switching in stratification as described by Simpson and Souza [1995]. The proximity of the measurement site to the Rhine outflow likely explains why stratification was observed in the nearshore, because the effects of tidal straining are enhanced due to the larger amount of fresh water that can be advected towards the coast [Simpson et al., 1993]. Moreover, during periods when a larger amount of fresh water is advected to the coast, other baroclinic processes rather than tidal straining are responsible for generating additional vertical stratification [De Boer et al., 2008, Flores et al., 2017]. Likewise, the observed stratification during ebb (about 1400H) cannot be explained by the semi-diurnal switching of stratification (tidal straining) and thus other baroclinic processes might have taken place due to the presence of the Rhine ROFI at the site during the survey (Figures 2.3 and 2.4). The frontal processes, that

are inherent to the near-field of the river plume [De Boer et al., 2008], also controlled the cross-shore exchange currents. Under these conditions, the buoyancy input may prevail over the stirring processes by wind and waves seaward of the Sand Engine during fair-weather conditions.

The results for the Richardson number (Figure 2.5) indicated that stratification had a dominant influence on the vertical structure of the flow measured at T₁. Further evidence of this dominance is shown by the ellipticity of the M₂ constituent (Figure 2.6e) which is strongly controlled by stratification as demonstrated by Souza and Simpson [1996]. The ellipticity of the M₂ constituent clearly showed the decoupling of the water column in two layers, denoting the importance of stratification in yielding the observed cross-shore exchange currents which extended all over the surveyed transect. This condition is believed to be representative of longer timescales as the average stratification (top-to-bottom salinity differences) from a six week mooring deployment during the same time period was 2.14 ± 1.7 psu [Flores et al., 2017] while the average stratification on October 17, 2014 was 2.29 psu.

To analyze the interplay between centrifugal acceleration and the baroclinic pressure gradient, Eq. 2.5 was scaled as in Seim and Gregg [1997] but using the two-layer approach so that the centrifugal term and the baroclinic forcing became $\Delta(v^2/R)$ and $(m/B)(gh/\rho_0)\Delta\rho$, respectively, where B is the transect width and $\Delta\rho$ is the top-to-bottom density differences and m gives the sign of the baroclinic forcing based on the mean cross-shore slope of the isopycnals. These calculations showed that the buoyancy force was greater than the centrifugal acceleration during the 13-hours survey (Figure 2.8a). The strength of the vertical shear (Figure 2.7) appeared to be controlled by $(m/B)(gh/\rho_0)\Delta\rho$ (Figure 2.8) confirming the small role of the curvature effects either in counteracting or enhancing the cross-shore exchange currents. After HW slack, weak vertical stratification was observed (Figure 2.3i) as the plume front approximated to the nearshore zone (Figure 2.4e) causing a switch of the cross-shore exchange currents at T₁ but not at T₂ (Figures 2.3e and f). At this tidal phase, the centrifugal acceleration was very small and thus it is plausible that the cross-shore baroclinic forcing was controlled by other baroclinic processes rather than classic tidal straining (i.e., semi-diurnal switching of stratification) so that the vertical shear tended to maintain a CC circulation at T₁.

As the centrifugal acceleration is a function of the alongshore velocities and the radius of curvature, it should fluctuate not only over a spring-neap cycle but also, on a longer timescale, according to the pace that the Sand Engine flattens out. We consider here whether the centrifugal acceleration played a more significant dynamical

cal role immediately after the Sand Engine was built when the curvature was greater. The centrifugal acceleration in prior conditions was estimated by using the radius of curvature of the Sand Engine estimated from bathymetric surveys in each year since 2011 and two weeks of simulated velocities off the tip of the Sand Engine [see Luijendijk et al., 2015]. In this estimate it was assumed that the flow contraction at the tip does not lead to any significant increase of the alongshore velocities at 12 m depth, resulting in a conservative estimate of the magnitude of the centrifugal term.

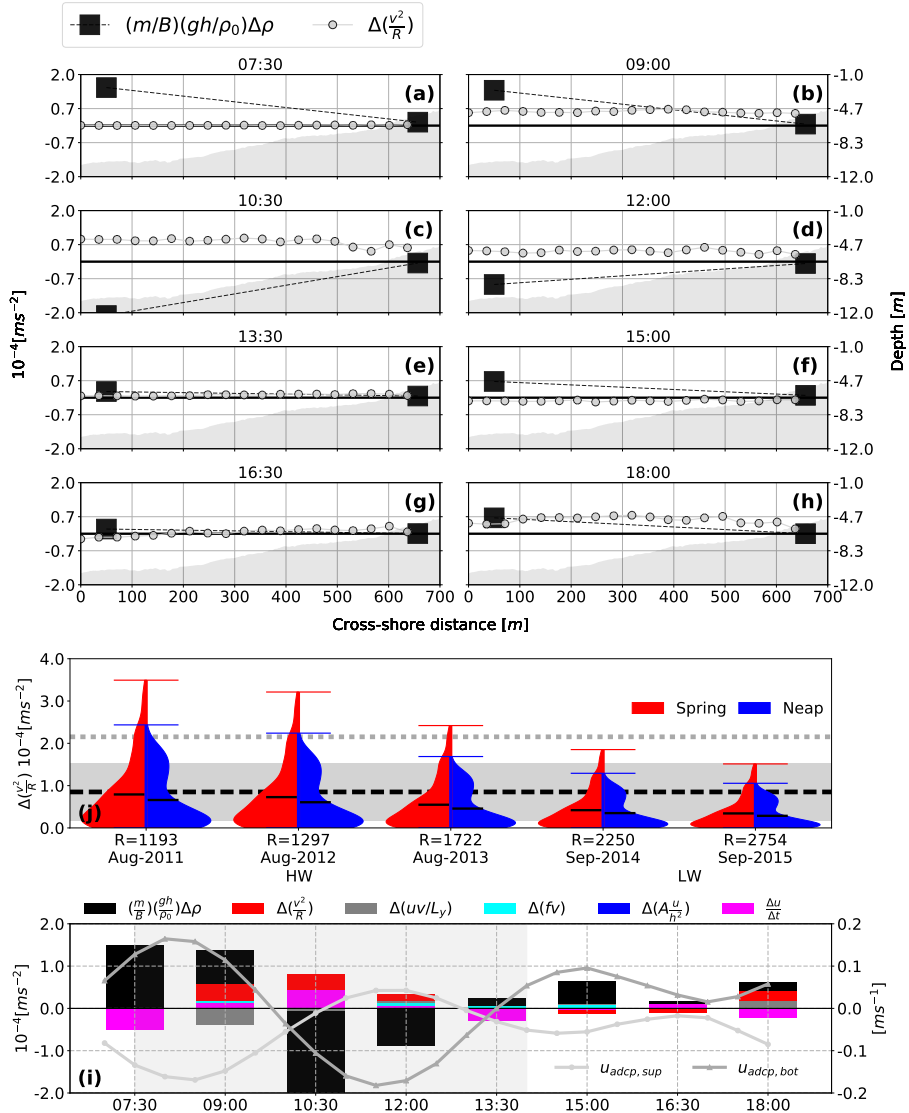


Figure 2.8: (Previous page.) (a to h) Distribution of the baroclinic forcing (squares) and centrifugal acceleration (circles) along transect T1 during 8 distinct periods of the tidal cycle. (i) Violin plot of the estimated centrifugal acceleration off the tip of the Sand Engine considering the changes in the radius of curvature (R , in meters) from 2011 until 2015. The shapes correspond to the distribution of the data during spring (red) and neap (blue) with their respective maxima (colored bars) and means (black bars). The dashed black line and shaded area show the mean and standard deviation of the baroclinic forcing. The dashed gray line in (i) indicates the maximum baroclinic forcing. (j) Scaled terms of the cross-shore exchange flow governing equation (left y-axis), and near surface and near bottom cross-shore velocities (right y-axis) at the seaward limit of T1.

In Figure 2.8i the centrifugal acceleration estimates are compared with the range of baroclinic forcing observed during our sampling period, noting that this corresponds to a neap period when the stratification is generally high. This exercise suggests that the curvature likely played a more important role in the first three years of the Sand Engine. At that time, the magnitudes of the centrifugal acceleration were comparable to the baroclinic forcing, although the mean baroclinic forcing was still higher than the mean centrifugal acceleration. Nonetheless, the cross-shore exchange currents might also have been controlled by curvature effects especially during spring tides, when stronger currents strengthen the centrifugal acceleration and tidal stirring reduces the baroclinic forcing.

Presently, the seaward deflection of the alongshore currents due to the curvature around the tip of the Sand Engine does not contribute significantly to the development of the observed cross-shore exchange currents. Given the observed dominance of the baroclinic forcing, the hypothetical interplay between centrifugal acceleration and baroclinic forcing seen in Figure 2.2 may be only valid in the far-field of the Rhine ROFI where the cross-shore baroclinic pressure gradient is expected to be controlled solely by the classic tidal straining and, obviously, where a curved seaward protrusion, such as the Sand Engine in its early stages, is present.

Therefore, as the cross-shore exchange currents did not appear to be effectively forced by centrifugal acceleration, we performed a scaling analysis of the remaining terms of Equation 2.4 to determine whether they contribute to the cross-shore momentum balance. Apart from centrifugal acceleration and baroclinic forcing, we also included the advective acceleration, $\Delta(uv/L)$, Coriolis acceleration, $\Delta(fu)$, vertical dissipation, $\Delta(Au/h^2)$, and time variation, $\Delta u/\Delta t$. The results in Figure 2.8j clearly demonstrate how the cross-shore exchange currents were greatly governed by

fluctuations of the baroclinic pressure gradient (black bars in Figure 2.8j), while the contribution of the other terms appeared to not significantly affect the behavior of the cross-shore exchange currents.

Nonetheless, the magnitude of the term $\Delta u/\Delta t$ (i.e., local time variation) revealed there is a tendency for the flow to accelerate (magenta bars in Figure 2.8j), implying the existence of a local imbalance between the driving forces. Thus, the time needed reach a steady state balance in Equation 2.5, as discussed by Lacy and Monismith [2001], could not be achieved most likely due to the short time that the tide takes to flow around the tip of the Sand Engine. Yet, it is not entirely clear whether other terms might have come to play with respect to the momentum balance. A speculative explanation is that the downwards transfer of momentum due to Reynolds stresses associated with the wave motion (i.e., $\rho \overline{u'w'} \neq 0$) [see Nielsen et al., 2011] might have contributed to the mixing term of the momentum balance as shore-perpendicular irregular waves were observed during the survey. However, with the available dataset, it was not possible to describe the term $\rho \overline{u'w'}$.

Moreover, the estimation of horizontal gradients over shallow and sloping bathymetries imposes a number of constraints ranging from numerical problems [e.g., Stelling and Van Kester, 1994] to observational limitations [e.g., Hopkins, 1996]. Hence, the scaling used in the present study, in which the baroclinic forcing is calculated from density profiles of two stations of unequal depth, provides a first-order approximation of the baroclinic term in Equation 2.5. Although the two-layers approach minimized some of those restrictions, it is likely that the assumption of mild cross-shore density gradients is violated when the plume front propagated through the surveyed transects around 1130H.

2.6 CONCLUSIONS

The observational results presented here provided information on the cross-shore current structures seaward of the Sand Engine, a localized mega-nourishment meant to naturally supply sand to the adjacent coast. Despite the large perturbation of the coastline, the current curvature of the Sand Engine does not present an appreciable contribution in controlling the cross-shore exchange currents. However, the curvature of the Sand Engine was higher when it was first built. Estimates of the centrifugal acceleration with higher curvature conditions suggest that curvature played a more significant role in the local dynamics during the first three years after the Sand Engine

was built, and likely contributed to cross-shore exchange currents. These effects are further enhanced during spring tides.

The cross-shore exchange currents were found to be strongly driven by the cross-shore baroclinic pressure gradient in the study area. The observed centrifugal accelerations were not large enough to balance the cross-shore baroclinic pressure gradient, thus other accelerations, e.g., $\Delta u/\Delta t$, are required to produce a balance considering the local spatiotemporal scale. The wave motion of the shoaling waves is believed to contribute to this balance, although it was not possible to quantify the competition between wave stirring and stratification in the nearshore.

Nonetheless, the occurrence of stratification in depths as shallow as 6 m associated with a relatively strong cross-shore shear, revealed that tidal straining and other baroclinic processes can occur in shallow waters even under the stirring effects of waves and wind. The proximity to the Rhine River mouth is a key condition that allows these baroclinic processes to take place in the nearshore.

Finally, the dataset used in this work, although limited, served to interpret the governing mechanisms of the cross-shore current structures in the vicinity of the Sand Engine. These findings strongly suggest that planning for future large nourishment projects such as the Sand Engine should consider the proximity of freshwater inflows to the nourishment site and account for the dynamics of the stratification-induced circulation in the nourishment design. This is an especially important consideration since good nourishment sites may often be proximate to large river inflows as engineered river mouths can often interrupt longshore sediment transport.

BED SHEAR STRESS IN THE DUTCH INNER SHELF

This chapter is based on the publication: S. Meirelles, M. Henriquez, A. R. Horner-Devine, A. J. Souza, J. Pietrzak, and M. Stive. Bed shear stress on the middle shoreface of the South-Holland coast. In The Proceedings of the Coastal Sediments 2015. World Scientific, 2015a

3.1 INTRODUCTION

This chapter addresses the importance of the hydrodynamics, discussed in Chapter 2, in driving momentum fluxes to the bed by means of the shear velocity, u_* . The shear velocity is a quantity from which the bed shear stress is readily computed. The bed shear stress is intrinsically related to the sediment mobility so that it is the fundamental connection between hydrodynamics and seabed responses.

The shear velocity is a derived quantity which cannot be measured directly. Many analytical and semi-empirical models (e.g., Grant and Madsen [1979], Grant and Madsen [1986]; Madsen [1994]; Soulsby et al. [1993] and Soulsby and Clarke [2005]) use different approaches to account for the combined action of waves and currents on the shear velocity. This is of fundamental importance as the hydrodynamics of the inner shelf is commonly driven by different forces acting at same time which are expected to equally contribute to the bed shear stress. To calculate the shear velocity, the flow is normally split in two (or more) components consisting of a steady part ($\bar{\mathbf{u}}$) and an oscillatory part ($\tilde{\mathbf{u}}$) due to currents and waves, respectively.

To assess how the hydrodynamics in the Dutch inner shelf is translated into frictional forces, an instrumented frame was deployed off the South-Holland coast to measure currents and waves. The acquired data served as input for the shear velocity and subsequent bed shear stress calculations following Madsen [1994]. The effects of

spring-neap cycles and stratification are examined with respect to their influence on the sediment transport.

3.2 STUDY AREA AND FIELD OBSERVATION

The experiment site has its southern border approximately 10 km from the Rotterdam Waterway. The Scheveningen harbor is in the northern limit, located 7.3 km from the deployment location. The offshore boundary of the experimental domain is near the depth contour of 18 m (Figure 4.1). The study area is also known by the presence of an unprecedented 21.4 Mm^3 localized nourishment called Sand Engine or Zandmotor [Stive et al., 2013].

As part of the STRAINS experiment (STRATification Impact on the Nearshore Sediment transport), a bed-frame (NEMO Lander) was deployed at the nominal depth of 12 m NAP (Dutch datum at approximately mean sea level) alongside other instrumented platforms. The measurements spanned over two spring tides during the winter of 2013.

The set of instruments mounted on the NEMO Lander measured currents and waves throughout the measurement period. Current profiles were estimated from a downward-looking Aquadopp-HR (mounted 50 cm above the bed) recording 1320 samples at 2 Hz every hour. Current profiles throughout the water column were recorded from an up-looking Aquadopp sampling at 1 Hz alternately with waves that were recorded at 2 Hz in burst of 17 minutes. Near-bottom flow was also continuously measured from single point current meters using an ADV (Vector) at 8 Hz deployed 0.5 m above the bed, approximately. Bottom sediment samples were collected with a Van Veen sediment grabber. Salinity and temperature were acquired with CTD probes mounted in a mooring. Additional wave data was provided by a Waverider buoy located at nearby site.

3.3 METHODOLOGY

3.3.1 *The Madsen [1994] model*

The approach of Madsen [1994] introduces the near-bottom orbital velocity directional spectrum in the turbulent wave-current bottom boundary layer model whose solution

is given by Grant and Madsen [1979, 1986]. The wave-current shear velocity is defined as:

$$\mathbf{u}_* = C_\mu \mathbf{u}_{*w\max}^2. \quad (3.1)$$

The factor C_μ accounts for the presence of currents. $\mathbf{u}_{*w\max}$ is the shear velocity based on the maximum representative wave-associated bed shear stress which is given by:

$$\mathbf{u}_{*w\max}^2 = \frac{1}{2} f_{wc} \mathbf{u}_{br}^2. \quad (3.2)$$

Eq. 3.2 introduces the friction factor f_{wc} in the presence of wave and currents which for practical application can be approximated by the following explicit formulas:

$$f_{wc} = \begin{cases} C_\mu e^{\left(7.02 \left(\frac{C_\mu}{k_N \omega_r}\right)^{-0.078} - 8.82\right)} & \text{for } 0.2 < (C_\mu \mathbf{u}_{br}) / (k_N \omega_r) < 10^2; \\ C_\mu e^{\left(5.61 \left(\frac{C_\mu}{k_N \omega_r}\right)^{-0.109} - 7.30\right)} & \text{for } 10^2 < (C_\mu \mathbf{u}_{br}) / (k_N \omega_r) < 10^4, \end{cases} \quad (3.3)$$

where k_N corresponds to the Nikuradse sand grain roughness of the bottom which is correlated with the bed roughness so that $k_N = 30z_0$; z_0 is the roughness length (or bottom roughness); and ω_r is the representative wave number so that

$$\omega_r = \frac{\iint \omega S_{uv}(\omega, \theta_w) d\omega d\theta}{\iint S_{uv}(\omega, \theta_w) d\omega d\theta}, \quad (3.4)$$

where S_{uv} is the directional near-bed orbital velocity cross-spectrum.

The representative bottom orbital velocity presented by Madsen [1994] and later extended by Wiberg and Sherwood [2008] is expressed as following:

$$\mathbf{u}_{br} = \sqrt{2 \iint S_{uv}(\omega, \theta_w) d\omega d\theta}. \quad (3.5)$$

Finally, the shear velocity for current alone is written as:

$$\mathbf{u}_{*c} = \frac{\mathbf{u}_* \ln(z_r / \delta_{wc})}{2 \ln(\delta_{wc} / z_0)} \left(-1 + \sqrt{1 + \frac{4k \ln(\delta_{wc} / z_0)}{(\ln(z_r / \delta_{wc}))^2} \frac{\mathbf{u}(z_r, \theta_c)}{\mathbf{u}_*}} \right). \quad (3.6)$$

The current shear velocity is an implicit relation that assumes that the current velocity and direction (θ_c) are measured at a certain height z_r above the boundary layer δ_{wc} .

3.4 DATA ANALYSIS

First, the horizontal velocities measured by the ADV were divided in segments of ≈ 17 min and then they were de-trended. The near-bed cross-spectra were computed via Fourier analysis. The chosen cut-off frequencies were based on the relative water depth h/L (where L is the wavelength) criteria from the Linear Theory. Figure 3.1 shows that the waves found in intermediate waters (i.e., waves that “feel” the bottom) were those with peak period between ≈ 4 and ≈ 14 s. Only those frequencies (periods) were considered in the wave power spectra. The wave orbital velocity series were interpolated to 8 Hz before the bed shear stress computation.

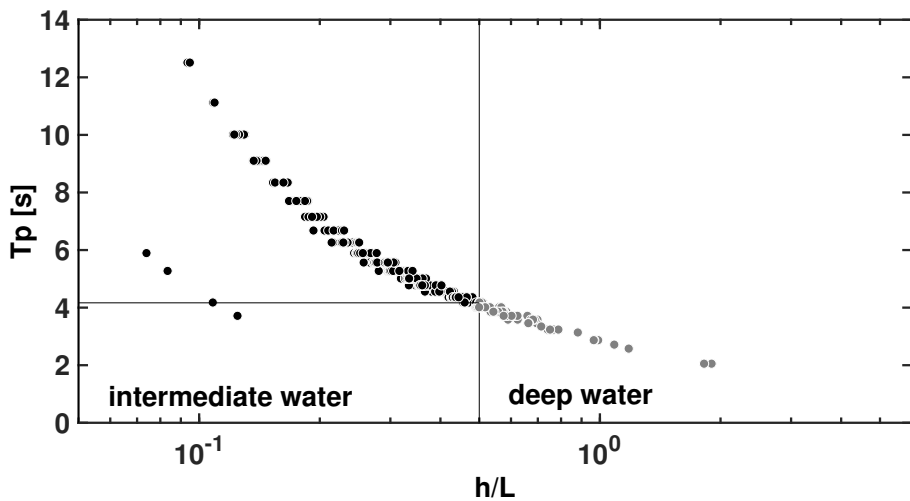


Figure 3.1: Wave peak period extracted from the wave records during the STRAINS experiment plotted against the relative depth h/L .

The astronomical tidal currents were obtained through harmonic analysis of the horizontal velocity components [Pawlowicz et al., 2002]. Prior to the performance of the harmonic analysis, the velocity signal was down-sampled into hourly averaged data. The principal shallow water constituents for the North Sea [Andersen, 1999] were included in the analysis so as to account for non-linearities caused by the higher tidal harmonics. The tidal current series were later up-sampled to 8 Hz.

A zero-phase Butterworth bandstop filter was applied aiming at obtaining the residual flow by removing the bandwidth of the wave frequencies. Priorly, the tidal signal was subtracted from the total signal. The role of the wave, tidal and residual components were assessed by means of bed shear stress whose formula reads:

$$\tau = \rho \mathbf{u}_*^2. \quad (3.7)$$

Where ρ is the seawater density which was derived from the depth-averaged CTD measurements. The shear velocity was resolved separately for the mean, oscillatory and residual parts of the flow (i.e., $\mathbf{u}_{\text{total}} = \mathbf{u}_{\text{tide}} + \mathbf{u}_{\text{wave}} + \mathbf{u}_{\text{residual}}$). The magnitude of each of those three components was calculated ($U = \sqrt{\mathbf{u}^2} = \sqrt{u^2 + v^2}$) to then be used as an input in the shear velocity model.

In the North Sea shelf, the tidal variance is dominant so that sophisticated filtering techniques to fully remove tides from the original signal are required [e.g., Brown et al., 2012]. The classical harmonic analysis, especially in shelf seas, can lead to tidal phase changes which generate unrealistic residual currents [Pugh, 1996]. To minimize this problem, it is common to apply specialized low-pass filter to dump all the tidal energy and avoid phase shifts. The downside is the loss of the higher frequency energies (> 26 h, for example) that may be related to wind variations, infragravity wave modulations and other processes that are relevant. The methodology used in the present investigation aimed at preserving the processes of interest for the sediment transport in the inner shelf.

3.5 RESULTS

The winds were persistent from the Northern quadrant varying from gentle to moderate almost through the whole period. The peak wave period fluctuated around 5 s. Because of the predominant wind-sea waves (5 s waves), the stirring role of wave action at 12 m depth was minor.

The tide induced bed shear stress (Figure 3.3) manifested a spring-neap tidal variance. The wave induced bed shear stress prevailed only during the passage of a moderate gale (year days 55 to 57). The bed shear stress induced by the residual currents appeared to be controlled by the local wind as it was observed a close association with the wind series.

Tide induced bed shear stress presented values higher than the threshold of motion near the peaks of flood and ebb tides, mostly during spring cycles. Wave induced

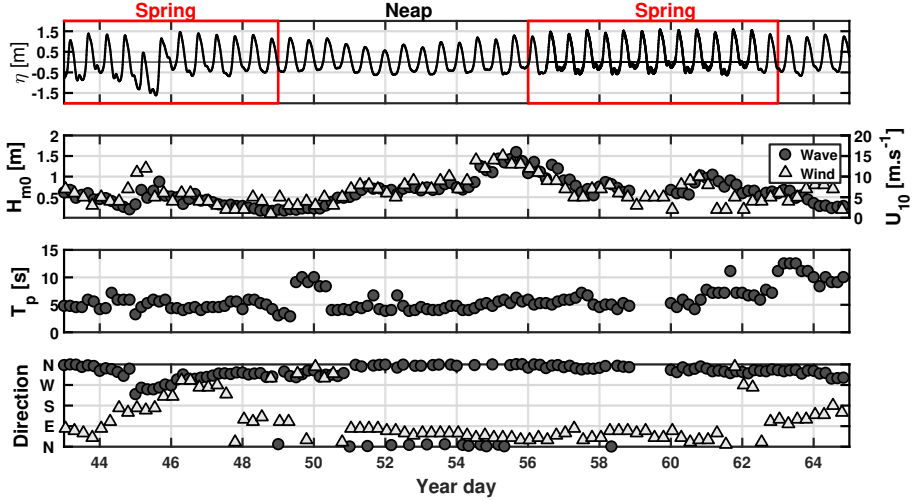


Figure 3.2: Oceanographic conditions during the STRAINS experiment. From top to bottom: [1] water elevation (the red rectangles indicate spring tides); [2] significant wave height (left axis; black circles) and wind speed (right axis; grey triangles); [3] peak period, T_p ; [4] wind (grey triangles) and wave direction (black circles).

bed shear stress showed values below the threshold of motion during fair weather conditions, but relatively high values of bed shear stress were observed during the gale, when the wave height was $\gtrsim 1$ m. The bed stress induced by residual currents showed values above the critical threshold for motion when the winds were $\gtrsim 8 \text{ m s}^{-1}$.

It is worth noting that the tidal flow is substantially influenced by stratification as discussed in Chapter 2. The occurrence of tidal straining and other baroclinic processes are translated into bed shear stresses immediately above the bed so that the sediment mobility is indirectly influenced by stratification. The behavior of the bed shear stress under the influence of stratification is seen in Figure 3.4 which presents τ_{tide} , τ_{wave} , τ_{residual} and the top-to-bottom salinity difference ΔS averaged across all M_2 tidal cycles of the first and second spring tides.

The observed stratification during spring tides demonstrated that, close to the river mouth, the tidal stirring alone is not strong enough to break stratification. Moreover, it is possible to observe that the sharp increase of stratification after HW slows down the decrease of bed shear stress during both springs (see the black vertical dashed line in Figure 3.4). This suggests that higher values of τ_{tide} are maintained for a longer period under the influence of the baroclinic tidal flow. τ_{wave} and τ_{residual} appeared

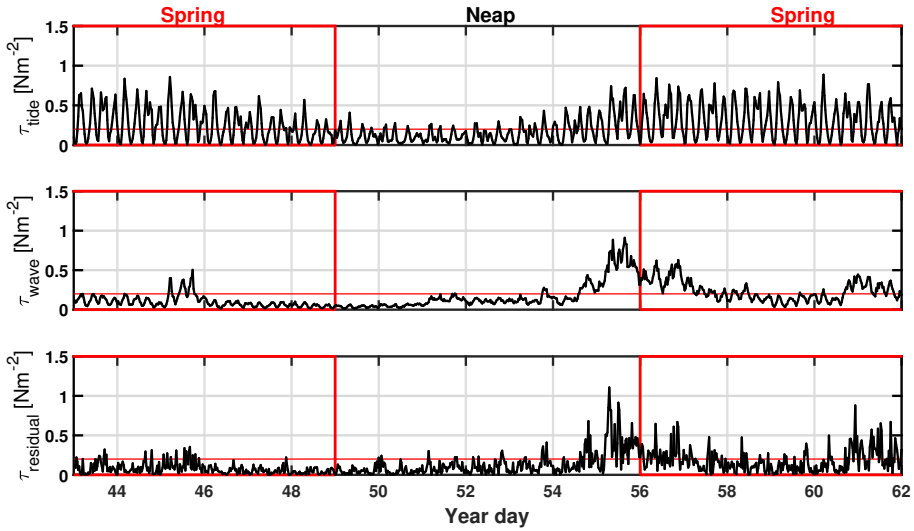


Figure 3.3: Computed bed shear stress using the Madsen (1994) approach (the red rectangles indicate spring tides). From top to bottom: [1] tide-induced bed shear stress; [2] wave induced bed shear stress; [3] residual current induced bed shear stress. The red horizontal lines indicate the critical bed shear stress with respect to the d_{50} during the STRAINS.

to have a weak association with stratification and, moreover, their magnitudes were significantly smaller.

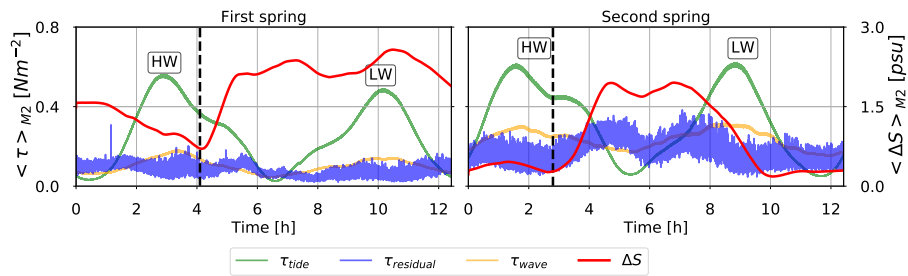


Figure 3.4: tide, wave, and residual current bed stresses together with top-to-bottom salinity difference averaged across all M_2 tidal cycles of the first (left panel) and second (right panel) spring tides. The vertical dashed black line indicates the rapid increase of stratification.

3.6 DISCUSSION AND CONCLUSIONS

The bed shear stress translates hydrodynamics into frictional forces on the bed that are directly related to sediment transport. Due to its transitional character, the inner shelf experiences the action of forcings that are normally negligible in the surfzone where breaking waves dictate most of the flow modulations that govern the sediment fluxes [Wright, 1995]. The present work showed that tides, waves and residual currents are responsible for impinging frictional forces onto the bed.

During the STRAINS experiment, the results showed that sand was periodically re-suspended by tides near the peaks of flood and ebb tides. Yet, the baroclinic tidal flow seemed to prolong higher values of bed shear stress. The wave agitation seemed to be not relevant during fair weather conditions indicating that the contribution of waves in the sediment transport in the inner shelf might be storm-driven. The results for the residual current bed shear stress demonstrated that other physical processes rather than tides and waves can eventually be of same importance to the bed shear stress.

We conclude that the tidal flow is likely to be the prevailing forcing that governs the bed shear stress off the South-Holland coast. Stratification is believed to significantly contribute to the bed shear stress due to its impact on the structure of the tidal currents (see Chapter 2). Nonetheless, the role of the tidal currents in agitating the bed seems to be only significant during spring tides.

Part II

MORPHODYNAMICS

A suit of instruments measured the near-bed flow together with sediment concentration and 3D bed elevation. A detailed inspection of the impact of the stratified tidal flow on the morphodynamics demonstrated that the net ripple migration is higher under the influence of stratification and so is the net bedload transport due to migrating ripples. The impact of stratification on the ripple dynamics is also connected to the contribution of the suspended load transport.

SMALL SCALE BEDFORM TYPES IN THE DUTCH INNER SHELF

This chapter is based on the publication: S. Meirelles, M. Henriquez, A. J. Souza, A. R. Horner-Devine, J. D. Pietrzak, S. Rijnsburg, and M. J. F. Stive. Small scale bedform types off the South-Holland coast. Journal of Coastal Research, 75(sp1):423–426, 2016

4.1 INTRODUCTION

The seabed morphology directly affects the overlying boundary layer and hence plays a fundamental role in the sediment load. The types of bedform can reveal important information on how the typical hydrodynamic regimes dictate sediment mobility. The occurring ripple patterns define the bed roughness which is of importance not only to sediment transport processes but also to biological and chemical processes that take place on the seafloor [Traykovski, 2007].

Following the analysis of Amos and Collins [1978] and Smyth and Li [2005], the bedforms are categorized in this work as follows: current ripples (C), wave ripples (W), combined wave-current ripples (WC), current ripples with subordinate wave ripples (Cw), wave ripples with subordinate current ripples (Wc) and poorly developed ripples (P).

This study aims at classifying the small scale bed states under mixed flow conditions found off the South-Holland coast through field observations. Visual identification of the bed states is compared to the wave-induced flow and the rotating tidal currents using the instantaneous mobility numbers. The mobility number is chosen here because it is independent on the bed morphology and hence it minimizes the uncertainties introduced by reducing the seabed properties into a single parameter such as the friction factor.

4.2 METHODS

The methodology described in the following sections is part of Chapters 4 and 5.

4.2.1 *Study area*

The study area is characterized by the presence of a mega-nourishment known as the Sand Engine (or *Zandmotor*, in Dutch) on the southern Dutch coast. The Sand Engine is designed to naturally supply sand for the adjacent coast [Stive et al., 2013] (Figure 4.1). The seaward protrusion of the Sand Engine impacts the barotropic tidal flow leading to the formation of eddies at its edges [Radermacher et al., 2016], but the baroclinic tidal flow, when present, dominates the cross-shore exchange currents [Meirelles et al., 2018a]. The baroclinic tide is controlled by the Rhine ROFI, that exits from the Rotterdam waterways and extends northward along the Dutch coast [Simpson et al., 1993, Simpson, 1997, Souza and Simpson, 1997, De Boer et al., 2009], exerting a direct impact on the sediment transport processes [Horner-Devine et al., 2017, Flores et al., 2017].

The grain size of the sediment in the south portion of the Dutch coast generally ranges from 125 to 250 μm [Wijnberg, 2002]. In the study area, Huisman et al. [2016] found a pronounced alongshore heterogeneity of the superficial grain size seaward of the Sand Engine. The authors observed a coarsening of the bed offshore the tip of the Sand Engine ($\approx 350 \mu\text{m}$ in 2014) and a fining at its flanks ($< 200 \mu\text{m}$ in 2014). Such alongshore heterogeneity in the spatial distribution of the grain size was accredited to the flow contraction at the Sand Engine.

4.2.2 *Data collection*

The dataset used in the present study includes hydrodynamics, density structure of the water column and seafloor morphology. Near-bed velocity was measured with Acoustic Doppler Velocimeters (ADVs) mounted at 0.25 m, 0.50 m and 0.75 m above the bed, sampling at 16 Hz during 5 mins bursts at 10 mins intervals (total of 2989 bursts). A mooring with a set of CTD's (Conductivity-Temperature-Depth) acquired salinity and temperature data throughout the water column approximately every 30 s. The information on the bedform dynamics was collected with a 3D profiling sonar - 3D Acoustic Ripple Profiler (ARP) - that scanned the seafloor every hour providing

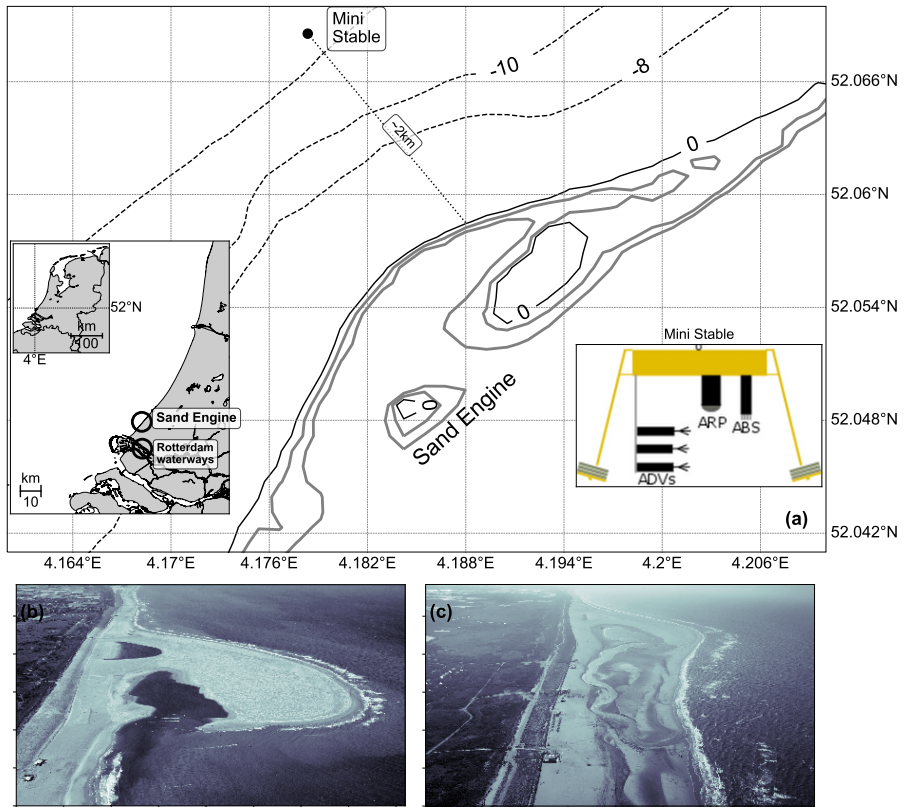


Figure 4.1: Location of the study area and the measurement site where the Mini Stable was deployed. (a) The inset shows the Netherlands, the Holland Coast with the Sand Engine and the Rotterdam waterways; (b) the Sand Engine a few months after its completion; and (c) the Sand Engine during the field experiment in Sep 2014 (Courtesy of Rijkswaterstaat/Joop van Houdt)

seafloor imagery of a circular area of approximately 11.8 m^2 . A four-frequency (1, 2, 3 and 4 MHz) acoustic backscatter system (ABS) measured the sound scattered by sediment over a profile. The suspended sediment parameters are extracted from the backscattered signal through the acoustic inversion method [Betteridge et al., 2006, Thorne and Hurther, 2014]. The ABS collected data for 5 min at 8Hz every 15 min interval.

4.2.3 Data analysis

Hydrodynamics

The along- (v) and cross-shore (u) near-bed velocities were decomposed into mean, oscillatory and turbulent components (i.e., $\mathbf{u} = \bar{\mathbf{u}} + \tilde{\mathbf{u}} + \mathbf{u}'$) following the method of Shaw and Trowbridge [2001] (hereafter ST method). The ST method applies an adaptive filtering technique to minimize the contamination by wave motion on the shear stress estimations that are derived from measurements of vertically separated current meters. In the present study, we used the ADVs at 0.25 m and 0.75 m above the bed (mab) to apply the ST method.

Wave-induced flow at 0.25 mab, $\tilde{\mathbf{u}}_{0.25}$, was obtained as follows:

$$\tilde{\mathbf{u}}_{0.25} = \mathbf{A}(\hat{\mathbf{h}}). \quad (4.1)$$

Where \mathbf{A} is a windowed data matrix containing the velocities at 0.75 mab with length equal to the number of points of one-half of the peak period. The filter weights are given by $\hat{\mathbf{h}}$ that is equal to $(\mathbf{A}^T \mathbf{A})^{-1} \mathbf{A}^T \mathbf{u}_{0.25}$.

To examine the movement of sediment by the flow, it is necessary to account for the non-linearities of the different velocity components. Following Reniers et al. [2004], the asymmetries of the non-linear tidal ($\tilde{\mathbf{u}}$) and orbital velocity ($\tilde{\mathbf{u}}$) were represented by the residual transport velocities:

$$\mathbf{u}_{rt} = \frac{\int_{t_0}^{t_0+1} \mathbf{u}^3 dt}{\int_{t_0}^{t_0+1} \mathbf{u}^2 dt}, \quad (4.2)$$

that were integrated over the burst length. The residual transport velocities are directly related to the equilibrium sediment concentration and provide a measure of the net effect of the sediment motion.

The ellipticity (ε) of the M_2 tidal constituent is [Thomson and Emery, 2014]:

$$\varepsilon = (W_+ - W_-)/(W_+ + W_-), \quad (4.3)$$

where W_{\pm} are the amplitudes of the cyclonic and anti-cyclonic circular components of the M_2 tidal current which was extracted from the series of horizontal velocities by using least-squares-based harmonic analysis.

The echo intensity recorded by the 3D profiling sonar was firstly converted into bed elevation and interpolated onto a regular Cartesian grid [Bell and Thorne, 1997]. The seafloor images were then de-trended and corrected for tilt variations of the benthic frame. Only a rectangle circumscribed to the circular scanned area was considered in the analysis, aiming to reduce the poor resolution of the image edges and noise created by the frame's legs. The final grid dimensions were 2.7×3.9 m and the image resolution was 1.95 cm per pixel so that the bedform analysis was limited to features with length scales between 2 cm and 2 m, approximately.

The ripple parameters were derived through discrete Fourier transform (DFT) of the two-dimensional images, $z(x, y)$, following Perron et al. [2008]. From the 2D-DFT, the mean ripple height (h) could be computed by

$$h = 4\sqrt{\sigma_z}, \quad (4.4)$$

where σ_z is the variance of the bed elevation. The weighted peak ripple wavelength (λ) was determined as:

$$\lambda = \frac{1}{\sqrt{k_x^2 + k_y^2}}, \quad (4.5)$$

that is a function of the two spatial wavenumber components k_x and k_y weighted by the spectral power. The bed images were rotated according to the coastline main orientation (42° CW from North) aiming at capturing the alongshore and cross-shore variances separately. From this, the ratio:

$$\frac{k_y}{|k|}, \quad (4.6)$$

was calculated as a measure of the ripple asymmetries, where $|k| = \sqrt{k_x^2 + k_y^2}$. Values of $k_y/|k|$ approximately equal to 1 are interpreted as symmetrical ripples governed by alongshore processes, whereas symmetrical ripples dominated by cross-shore processes have $k_y/|k| = 0$.

The ripple migration rate (M_r) was derived from the 2D normalized cross-correlation between two consecutive images, $\bar{R}_{12}(\vec{x})$, which were one hour apart. The distance lag corresponding to the strongest positive peak ($\vec{x} = l^*$) in the correlation

function provided information on the mean distance traveled by the ripples per hour. The normalized correlation for two consecutive images can be defined as

$$\bar{R}_{12}(l^*) = \frac{R_{12}(l^*)}{\sqrt{R_{11}(0) + R_{22}(0)}}, \quad (4.7)$$

where $R_{11}(0)$ and $R_{22}(0)$ are the zero lag autocorrelation for each image. The peak correlation lags in x and y were then used to calculate the migration rate as

$$M_r = \frac{\sqrt{l_x^{*2} + l_y^{*2}}}{\Delta t}. \quad (4.8)$$

The direction, θ , of the ripple migration was also determined by

$$\theta = \tan^{-1} \left(\frac{l_y^*}{l_x^*} \right). \quad (4.9)$$

Also, a first order approximation of the ripple migration was obtained through optical flow technique which computes the 2D vector field of consecutive images [Solem, 2012]. We applied this technique over a sequence of 12 (=12 hours) bed imageries aiming at getting estimations of the ripple motion within a tidal cycle.

Bed states

Following the analysis of Amos et al. [1988] and later Smyth and Li [2005], the bed-form categories in this work were: current ripples (C), wave ripples (W), combined wave-current ripples (WC), current ripples with subordinate wave ripples (C_w), wave ripples with subordinate current ripples (W_c) and poorly developed ripples (P). The bed states were first determined by visual observation. Two operators classified the images independently according to the classification of Amos et al. [1988] in which the criterion was based on the ripple geometry, orientation and length. The discrepancies that resulted from both classifications were small and were adjusted based on the hydrodynamic information. Most of the differences occurred during mixed bed states especially C_w and WC types.

The instantaneous mobility number was also used to categorize the bed types. The mean absolute velocities, obtained by subtracting the wave-induced flow and the random variations from the total velocity (i.e., $\bar{\mathbf{u}} = \mathbf{u} - (\bar{\mathbf{u}} + \mathbf{u}')$), was used to calculate the mobility number that reads:

$$\Psi_c = \frac{\overline{u_{0.25}}^2 + \overline{v_{0.25}}^2}{(s-1)gd_{50}}. \quad (4.10)$$

Where s is the ratio of particle to water densities, g is acceleration due to gravity and d_{50} is the median grain size from samples collected during the experiment (≈ 0.350 mm). In a similar fashion, the mobility number for waves, Ψ_w , was computed. The logarithm of the ratio of $\Psi_{rms,w}$ to $\Psi_{rms,c}$ was used to evaluate the conditions for the formation of wave and current bedform types analogous to the approach presented by Amos and Collins [1978].

Bedload and suspended load transport

The mean bedload transport (Q_b) associated with migrating ripples, assuming that sediment by-passing from one ripple to another is negligible and the sediment suspension is not intermittent [Soulsby, 1997], was computed as [Masselink et al., 2007]:

$$Q_b = \rho_s(1 - p)M_r h. \quad (4.11)$$

Where $\rho_s = 2650 \text{ kgm}^{-3}$ is the sediment density for quartz sand, p ($= 0.35$) is the sediment porosity and h is the ripple height.

The observed flux of suspended sediment by tides is given by:

$$q_s = \langle \bar{u} \bar{C} \rangle. \quad (4.12)$$

Where \bar{u} was obtained from the ST method (Section 4.2.3), \bar{C} is the mean suspended sediment concentration and $\langle \rangle$ denotes hourly averaging.

Stratification

The bottom-surface salinity differences (ΔS) provided information on the degree of vertical stratification of the water column [Simpson et al., 1993]. The salinity series at 1 and 11 m below the surface were used to compute the values of ΔS .

4.3 RESULTS

The measurements encompassed two neap-spring cycles. The wind speed during the measurement period was $6 \pm 3 \text{ ms}^{-1}$ mainly from South quadrant during fair weather conditions. The wave height was 0.6 m on average with direction varying basically between N and W. The average peak wave period was 6 s. One significant episodic event was captured where waves reached more than 2 m height and the wind blew at 16 ms^{-1} .

From the visual identification of the bedforms, current-formed ripples predominated throughout the series followed by poorly developed ripples (Figure 4.2). Amos and Collins [1978] characterized poorly developed ripples based on the stationarity of the crests from frame to frame. Wave ripples occurred the least number of times being associated with the passage of storm. Intermediate states of ripple geometry prescribed about 23% of the recognized types.

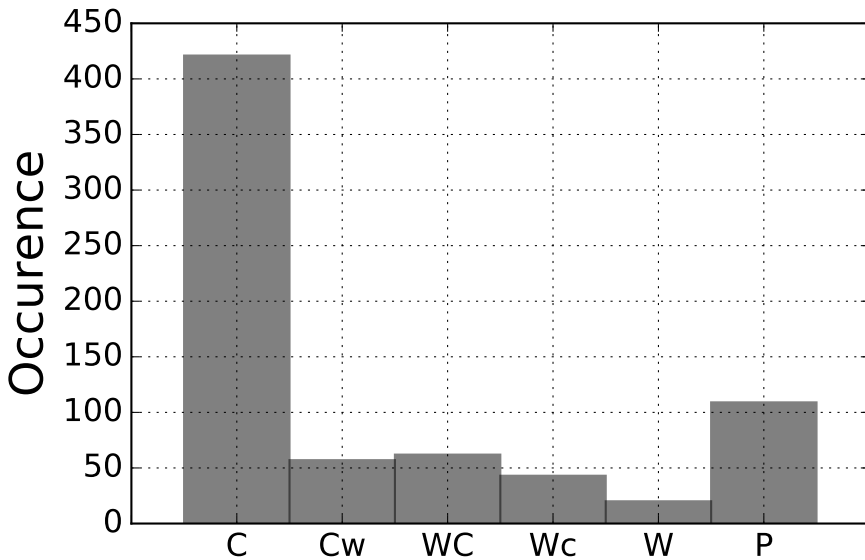


Figure 4.2: Occurrence of current ripples (C), wave ripples (W), combined wave-current ripples (WC), current ripples with subordinate wave ripples (Cw), wave ripples with subordinate current ripples (Wc) and poorly developed ripples (P). This result is based on the visual identification explained in the text

The current mobility number not only exhibited semi-diurnal dependence but also revealed a coherent fortnight oscillation as expected (Figure 4.3a). The wave mobility number predominated between days 264 and 265 reaching values over 120 which were about 5 times greater than the current counterpart. Although the current mobility number appeared to prevail, the wave mobility number presented similar magnitude during four different periods through the record. Figure 4.3b depicts the comparison between the $\log(\psi_{rms,w}/\psi_{rms,c})$ and the bed types resulted from the visual observation. There was a general agreement between both approaches. The majority of curve lies below -1 indicating the high occurrence of C and P. Values greater than 1

encompassed the wave-formed ripples. All the intermediate bed states were within -1 and 1 . Remarkably, a persistent semi-diurnal fluctuation was observed (Figure 4.3b) denoting how important the tidal currents are in the region. Poorly developed ripples were mostly observed under fair weather conditions during neap tides.

4.4 DISCUSSION

The dominant type of small scale bedform found off South-Holland coast was current-generated ripple. On the contrary, Traykovski [2007] observed a dominance of wave orbital scale ripples at similar depth. Also, Smyth and Li [2005] identified predominantly W and Wc types of ripples, at depths greater than 20 m, on Sable Island Bank. Those evidences reflect the role of the waves in exposed coastal areas where the incident waves are dominant, which is not the case in the North Sea where most of the incident waves are wind-sea waves.

Nonetheless, during episodic events, waves were responsible to quickly reorganize the bed morphology which likely led to hysteresis during the following waning conditions. As expected, wave-formed ripples exhibited an evident 2D pattern whereas current-formed ripples were 3D (Figure 4.4). Furthermore, wave-formed ripples were found to migrate at a rate twice as much than current-formed ripples with approximately 90° difference in their migration directions as seen by their trajectories in Figure 4.4.

Purely current ripples were clearly tidal driven although wind-driven flow might be important too, but it was not considered in the present study. The seabed morphology did not experience significant changes in neap tides with calm conditions when poorly developed ripples were encountered.

The intermediate bed states altogether comprise the second highest bed state occurrences. This indicates the importance of the combined action of wave and currents on the bed morphology at the location. However, those transitional bed states were difficult to classify properly as seen in Figure 4.3b. This is especially true after wave events when the bed restoration suffers a delay as reported by Traykovski [2007].

The dimensionless mobility number ratio used here seems to perform poorly when the ripples are not in equilibrium with the hydrodynamic forcings. Therefore the thresholds established (between -1 and 1) for Cw, WC and Wc types are possibly not fixed but dependent on ripple length information. Despite of limitations, the visual

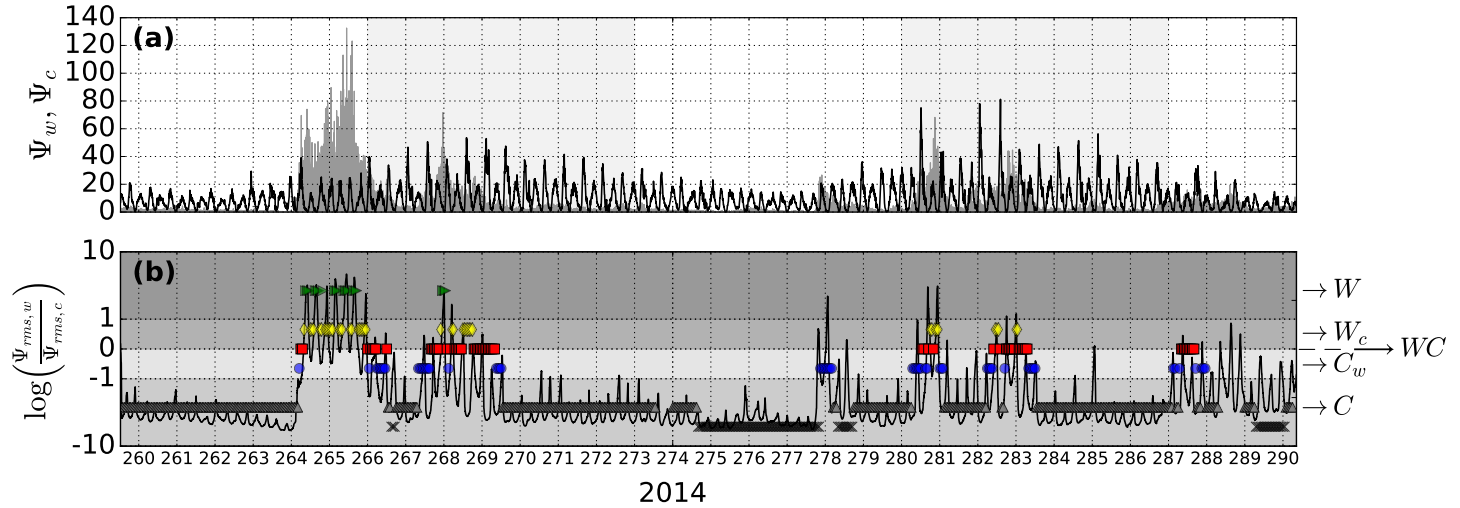


Figure 4.3: (a) time series, in days of 2014, of the wave and current mobility numbers. The hatched areas depict the spring tide periods. (b) series of the logarithm of the ratio of $\Psi_{rms,w}$ to $\Psi_{rms,c}$ compared to the results from the visual observation. The green, yellow, red, blue, gray and black marks correspond to W , W_c , WC , C_w , C and P , respectively.

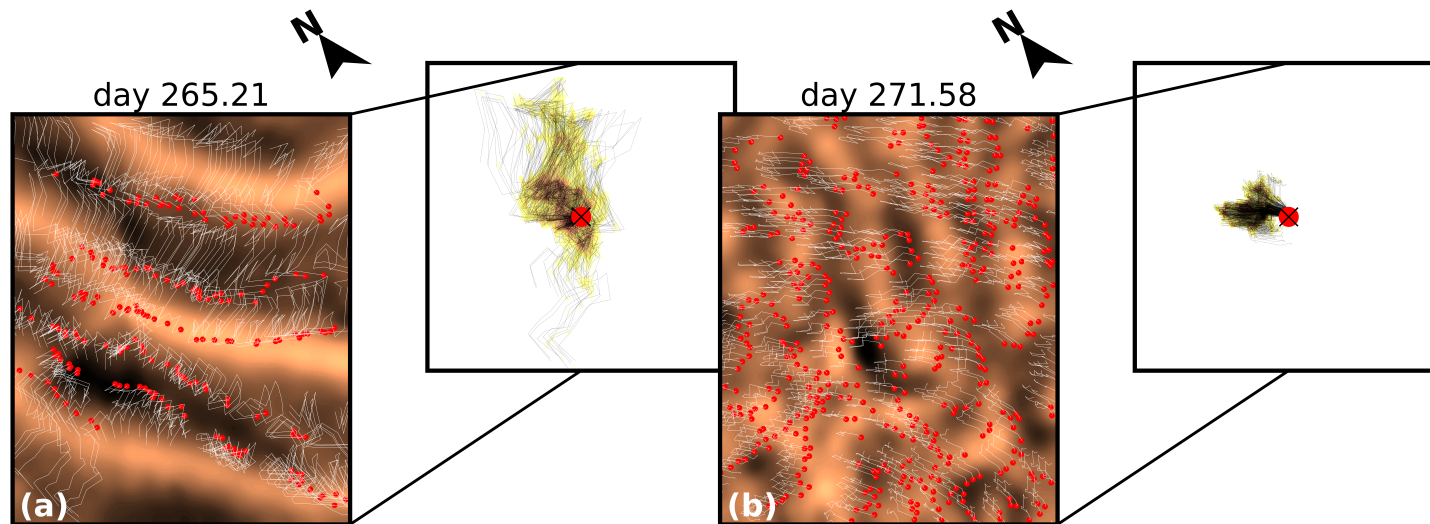


Figure 4.4: Seafloor imagery of a wave-formed ripple observed during the storm event on day 265 (a); and current-formed ripple observed during the first spring tide on day 271 (b). The trajectories seen in (a) and (b) were extracted from 13 consecutive images (i.e., approximately one tidal cycle) using optical flow technique (pixel tracking). The ending point of the trajectories is shown by the red circles (also seen in the insets). The insets in (a) and (b) depict the 2-D histogram of all trajectories together providing a first order estimation of the magnitude and direction of the mean ripple migration respectively.

classification presented a good agreement with the dimensionless mobility number ratio.

4.5 CONCLUSIONS

This study classified the small scale bedforms found offshore the South-Holland coast. The bedforms were separated into 6 categories: current ripples (C), wave ripples (W), combined wave-current ripples (WC), current ripples with subordinate wave ripples (Cw), wave ripples with subordinate current ripples (Wc) and poorly developed ripples (P). The method based on direct visual detection from the seabed images was compared to a simple relation between the wave and current rms mobility number.

The results showed that current ripples, C, were dominant throughout the series. The frequency of occurrence of transitional bed types (Cw, WC and Wc) combined ranked second. Those types were normally associated with rapid change of the bed morphology and more complex ripple patterns. Most of the poorly developed ripples were found during neap tide, while the bed activity is more prominent during spring tide. This reinforces the findings by Henriquez et al. [2016, in prep.] that most of the sediment transport at the measurement site occurs during spring tide.

The dimensionless mobility number ratio appeared to be a simple and quick way to assess the bed states found off South-Holland coast. Since the wave action was not persistent, relict ripples were not a regular feature and hence the ripples might have been in (quasi-)equilibrium with the hydrodynamic forcings in most of the cases.

EFFECTS OF A STRATIFIED TIDAL FLOW ON THE BEDFORM DYNAMICS

This chapter is based on S. Meirelles, A. J. Souza, A. Horner-Devine, J. Pietrzak, M. Henriquez, S. Rijnsburg, R. Flores, M. J. F. Stive, and A. Reniers. Effects of a stratified tidal flow on bedform dynamics. Submitted to the Journal of Geophysical Research, 2019.

5.1 INTRODUCTION

Small-scale bedforms (or ripples) in the marine environment are important to sediment transport processes as rippled beds generate form drag roughness that is usually the dominant controlling mechanism of sediment re-suspension from the seabed [Vincent et al., 1991, Li et al., 1996, Kleinhans et al., 2005]. Moreover, the sand movement by bedload transport commonly involves the migration of bedforms [Wright, 1995, Soulsby, 1997]. In natural environments, ripples can develop complex geometries due to the combined action of the many hydrodynamic forcings, posing a challenge to the study of sediment transport.

Because of the unsteady nature of the hydrodynamic forcings, ripples are continuously adjusting to a new equilibrium [Grant and Madsen, 1979, Baas et al., 2016]. While wave ripples evolve on the time scale of hours [Lofquist, 1978], the time taken by current ripples to reach an equilibrium ranges from a few minutes to days or weeks [Baas, 1994]. Amos and Collins [1978] have reported changes in the ripple morphology within a tidal cycle in which water depth variations mediated the competition between waves and tides on shaping the bed. The protrusion of the roughness elements into the flow also responds to tidal oscillations as investigated by Lefebvre et al. [2011], who found that the bedform roughness of large scale ripples varied by a factor of 10 over a tidal cycle. Despite the bedform dynamics being dictated by tides

in many environments, little is known about the effects of the tidal flow on bedforms in stratified regimes.

Under steady flow conditions, Baas [1994] showed that current-generated ripples always reach a dynamic equilibrium if sufficient time is provided. The author found that the evolution of current ripples can be divided in four developmental stages that, from an initial flat bed, are: incipient ripples, straight and sinuous ripples, non-equilibrium linguoid ripples, and equilibrium linguoid ripples. The empirical model of Oost and Baas [1994] demonstrated that the occurrence of these stages of development in a tidal environment depends on the nature of the tidal flow in which the formation of equilibrium linguoid ripples can be prevented by continuous changes in the current direction and/or velocity. Thus, ripple development and symmetry are also expected to be impacted by the highly variable tidal flow that occurs under stratified conditions in many coastal regions with a freshwater plume [e.g., Souza and Simpson, 1996].

Along the Dutch coast, the tidal currents are dominated by the M_2 constituent and exhibit the character of a progressive Kelvin wave propagating to the northeast so that the peaks of flood and ebb currents coincide with high and low water, respectively. In the absence of vertical stratification resulting from the freshwater input of the Rhine river, the tidal excursion is nearly rectilinear and parallel to the coast throughout the water column [De Boer et al., 2006]. Fluctuations of the vertical stratification created by tidal shear acting on the horizontal density gradients, decouples the water column at the pycnocline [Simpson et al., 1993, Visser et al., 1994, De Boer et al., 2008]. This generates a strongly sheared flow leading to the development of counter-rotating tidal ellipses in the bottom and surface layers with 180° phase difference. The sheared flow created by stratification primarily affects the cross-shore component of the flow, whereas the alongshore component remains the same throughout the water column. The two-way interaction between the horizontal density gradients and the counter-rotating tidal ellipses (cross-shore shear) leads to a semidiurnal switching in stratification in the Rhine Region Of Freshwater Influence (hereafter Rhine ROFI) through a processes called tidal straining, with maximum and minimum stratification occurring at high and low water, respectively [Simpson and Souza, 1995]. Additionally, a fortnight variability of stratification in the mid- and far-field of the Rhine ROFI has been observed as a result of the vertical mixing promoted by spring currents [e.g., Souza and Simpson, 1996, Simpson, 1997], however, recent studies have shown that strong stratification can occur in near-field of the Rhine ROFI throughout a spring-neap cycle [e.g, Horner-Devine et al., 2017, Flores et al., 2017, Meirelles et al., 2018a].

While significant advances have been achieved on bedforms, the morphodynamic behavior as ripples under combined wave-current flow conditions in the marine environment is still not well understood. As a consequence, the application of existing ripple predictors is limited to the thresholds derived from lab experiments and insufficient field observations which are mostly from wave-dominated coasts. More recent studies [e.g. Nelson and Voulgaris, 2014, 2015] have been aimed at describing and predicting the nonequilibrium time-varying ripple parameters by accounting for the multidirectional character of the waves. However, due to the lack of information on the bed response to the combined effects of wave and currents, the model validation has been restricted to wave-dominated environments.

This chapter aims to explain the morphological response of the bed to the stratified and non-stratified tidal flow on the Dutch inner shelf whose seabed is predominantly sandy. Moreover, we explore how the bedform dynamics affects the bedload transport and sediment resuspension from the bed with respect to stratification. The goal is addressed with an extensive dataset collected off the southern coast of the Netherlands during a more than 30 days measurement.

5.2 METHODS

During Autumn 2014, a suite of instruments was mounted on a bed frame (known as Mini Stable) that was deployed 2 km offshore at 12 m depth. The measurements aimed at gaining knowledge on the dynamics of the Rhine Region of Fresh Water Influence (ROFI), that outflows from the Rotterdam waterways, and its connections with the morphodynamics and sediment transport seaward of the Sand Engine. The campaign was part of a joint multi-disciplinary experiment named STRAINS (Stratification Impacts on Nearshore Sediment Transport) and MegaPEX (Mega Perturbation Experiment). Detailed information on the methodology is presented in Section 4.2 of Chapter 4.

5.3 RESULTS

The measurements covered nearly two full spring-neap cycles (Figure 5.1a). The average ripple height over the entire series was 2.2 ± 0.5 cm, reaching 4.2 cm during the only severe storm recorded (Figure 5.1b). The average significant wave height and peak period were 0.67 m and 6.2 s, respectively. The correspondence between wave

height and wind speed indicated the predominance of wind-sea conditions throughout the campaign. Under fair weather conditions, the average wind speed fluctuated around $6.26 \pm 3.00 \text{ ms}^{-1}$ predominantly from the south. The storm was marked by wave height of 2.23 m with wind speed of about 15 ms^{-1} . The mean river discharge was $1867 \pm 335 \text{ m}^3\text{s}^{-1}$ which is above the Autumn's climatological average of $1750 \text{ m}^3\text{s}^{-1}$. The mean grain size at the measurement site from samples collected during the campaign was $252.3 \pm 35.7 \mu\text{m}$, fluctuating between medium and fine sand fractions.

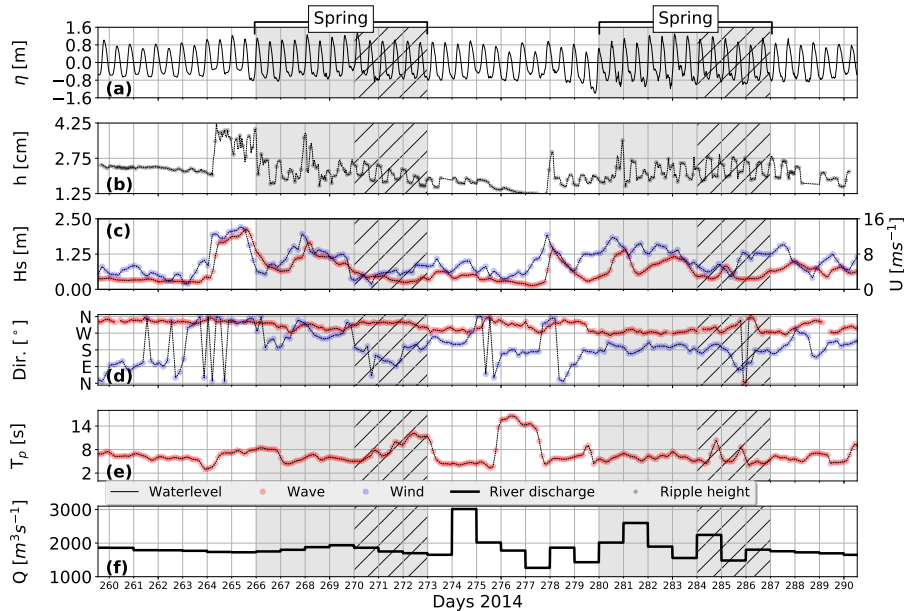


Figure 5.1: Observed conditions during the field measurements. (a) waterlevel derived from the ADV pressure sensor; (b) ripple height; (c) significant wave height (red) and wind speed (blue); (d) wave (red) and wind (blue) directions; (e) wave peak period; and (f) river discharge. The spring tides are marked by the gray areas and the hatches inside the gray areas indicate the periods used to investigate the bedform behavior with respect to stratification (see text for details).

In Chapter 4, we showed that 59% of the ripples were classified as current ripples. Wave ripples occurred only during the storm, comprising 3% of all occurrences. The frequency of occurrence of transitional bed types composed 23% and poorly developed ripples were found to develop mostly during neap tides making up 15% of the observed bed types. The predominance of the current ripples during the two spring-neap tides is exemplified in the acoustic imagery of the seabed shown in Figure 5.2.

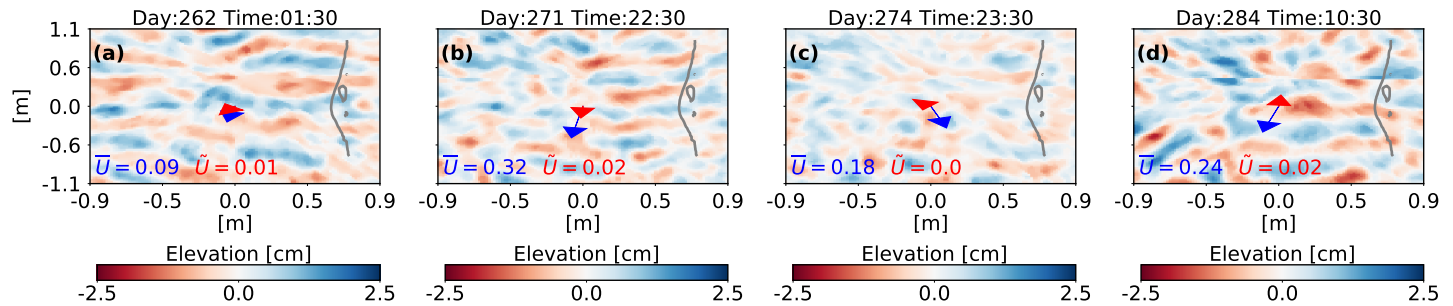


Figure 5.2: Imagery of the seabed for four different periods correspondent to Neap 1 (a); Spring 1 (b); Neap 2 (c) and Spring 2 (d). The current speed (blue arrows) and the orbital velocity (red arrow) are also indicated on the images. The approximate orientation of the coastline is represented by the Sand Engine contour (not to scale).

Relatively small near-bed orbital velocities as well as neap currents were not able to reshape the bed as shown further in this study.

5.3.1 *Spring-neap variability*

Strong vertical stratification ($\Delta S > 2$) was observed throughout the measurement period except for the second spring tide which was characterized by the periodic intrusion of the tidal plume front but with no significant ambient vertical stratification (Figure 5.3). The incidence of fronts during the second spring tide is believed to be controlled by the local wind that was on average stronger than in the first spring (Figure 5.1c). Five wave events ($H_{m0} > 1$ m) were detected in the time series in which wave ripples were observed in the bed imagery (see Chapter 4). As the present investigation focuses on the near-bed tidal flow, the wave events were not considered in the analysis of the bedform dynamics.

The results show a fortnightly variation of the bedform dynamics in which no significant motion of the bed was observed during neap tides regardless of the onset of stratification (Figure 5.3c-f). The ripples tended to gradually degrade during neap tides under fair weather conditions as seen by the gentle decay of the ripple height in Figure 5.3b. On the contrary, a conspicuous semi-diurnal modulation of the ripple properties was observed during spring tides. This indicated that, while the bed tended to remain immobile during neap tides, the spring currents often exceeded the threshold current speed for initiation of motion so that the ripples were able to (re-)adjust to the nature and strength of these currents. Given the minor role of the neap currents on the bedform dynamics, we considered only the spring tide periods in our subsequent analysis.

5.3.2 *Ripple response to stratified and non-stratified spring tide currents*

To examine the impact of the stratified tidal flow on the bedform dynamics, we selected two different periods with the same duration and similar oceanographic conditions, except for the presence of ambient stratification. Spring 1 corresponds to a 3-day period (day 270 to 273) selected from the first recorded spring tide that was marked by the vertical stratification of the water column (second column of Figure 5.3), whereas Spring 2 consists of another 3-day period (day 284 to 287) selected from the second recorded spring tide in which no significant vertical stratification was ob-

served (fourth column of Figure 5.3). Both Spring 1 and Spring 2 were characterized by fair weather conditions allowing for the investigation of impact of the tidal currents on the bedforms.

Relatively weak winds ($4.07 \pm 1.37 \text{ ms}^{-1}$) with varying direction allowed the water column to remain stratified during Spring 1. During Spring 2, the winds strengthened ($6.73 \pm 2.27 \text{ ms}^{-1}$) and sustained a southerly direction for about 5 days, including those days preceding Spring 2 (Figure 5.1c-d). This allowed for an Ekman-type transport (downwelling winds) which favored mixing [Souza and James, 1996]. The polar histograms in Figure 5.4 depict the occurrence of wind events associated with

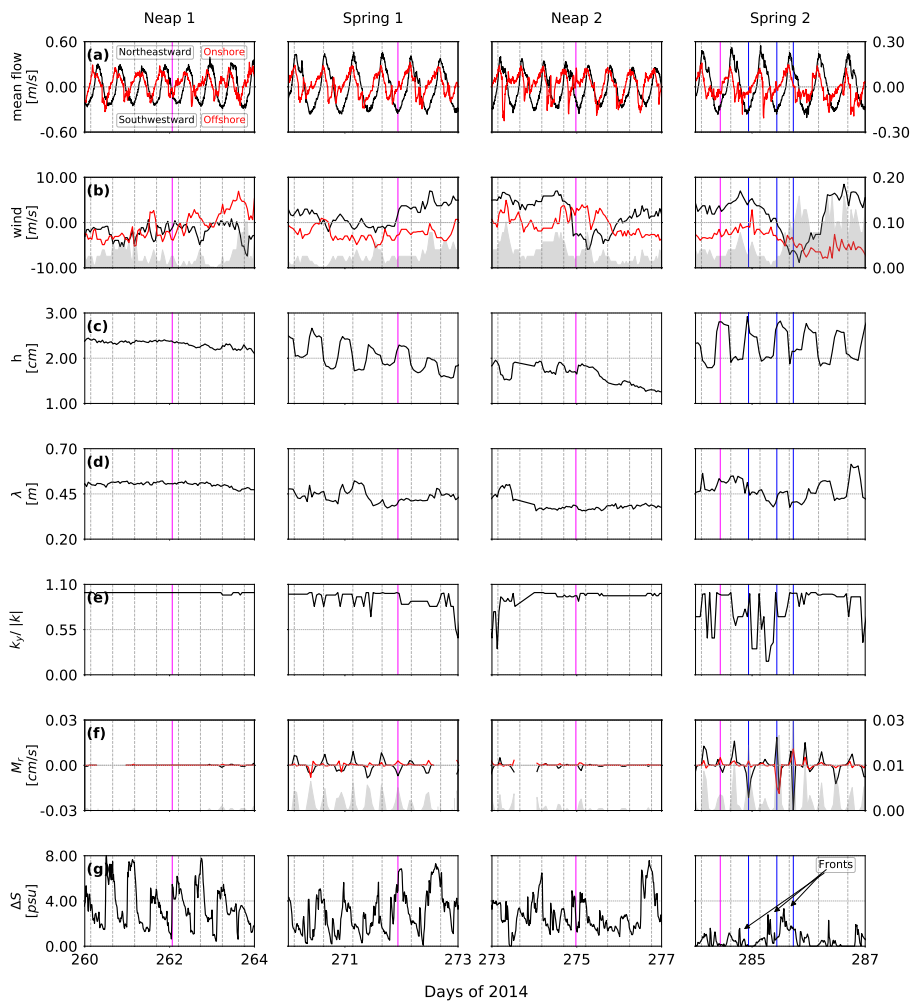


Figure 5.3: (Previous page.) Time series of the main parameters during Neap 1, Spring 1, Neap 2 and Spring 2. (a) Alongshore (black line; left y-axis) and cross-shore (red line; right y-axis) mean flow; (b) Alongshore (black line; left y-axis), cross-shore (red line; left y-axis) wind velocity, and wind stress, in Pa, at the sea surface (shaded area in gray; right y-axis); (c) mean ripple height; (d) ripple weighted peak wavelength; (e) $k_y/|k|$ ratio; (f) Alongshore (black line; left y-axis) and cross-shore (red line; left y-axis) ripple migration rates, and ripple migration magnitude (shaded area in gray; right y-axis); (g) top-to-bottom salinity differences. The vertical blue lines indicate the peaks observed in the ripple migration rates during Spring 2. The vertical magenta lines indicate the time when the images in Figure 5.2 were collected. The events with $H_s \geq 1$ m were left out from this figure.

stratification during Spring 1 and 2. Southerly wind events during Spring 2 lasted twice as long as those of Spring 1 such that the majority of wind events in Spring 2 was associated with values of ΔS between 0 and 2 (lower panel in Figure 5.4a), denoting that there was no significant stratification. On the other hand, the wind events during Spring 1 occurred in all ΔS bands (upper panels in Figure 5.4a-d), however, most of the occurrences were observed within $0 < \Delta S \leq 2$ and $2 < \Delta S \leq 4$. It is important to note that most of the periods in which the water column got mixed during Spring 1 were closely related to the effects of tidal straining that is responsible for the semi-diurnal switching of stratification [e.g., Visser et al., 1994]. In contrast, the onset of stratification during Spring 2 was promoted by the frontal passages and it lasted for few hours under easterly winds influence (Figure 5.3g). The mechanisms that generate the fronts are not yet well understood, but it is speculated that the fronts result from the cross-shore advection of the inner edge of the Rhine ROFI or the ejection of brackish water lenses from the river mouth on ebb tide [de Ruijter et al., 1997, De Boer et al., 2008, 2009, Horner-Devine et al., 2017].

Regarding the effects of stratification on the bedforms, the results suggested that the ripples responded differently to the stratified conditions in Spring 1 and the frontal period in Spring 2 (Figure 5.3c-g). This is evidenced by differences in ripple height, wavelength, geometry, and migration rate as summarized in Table 5.1. The ripple height and wavelength during Spring 1 were respectively 11% and 8% smaller than in Spring 2. The values of the wavenumber ratio $k_y/|k|$ were 13% higher during Spring 1 showing that the ripples exhibited a more symmetrical morphology. This difference in the ripples geometry seen in Spring 1 and 2, that probably resulted from the lower migration rates, might indicate that the ripple development was inhibited by the rotating stratified flow so that the continuous changing in direction did not

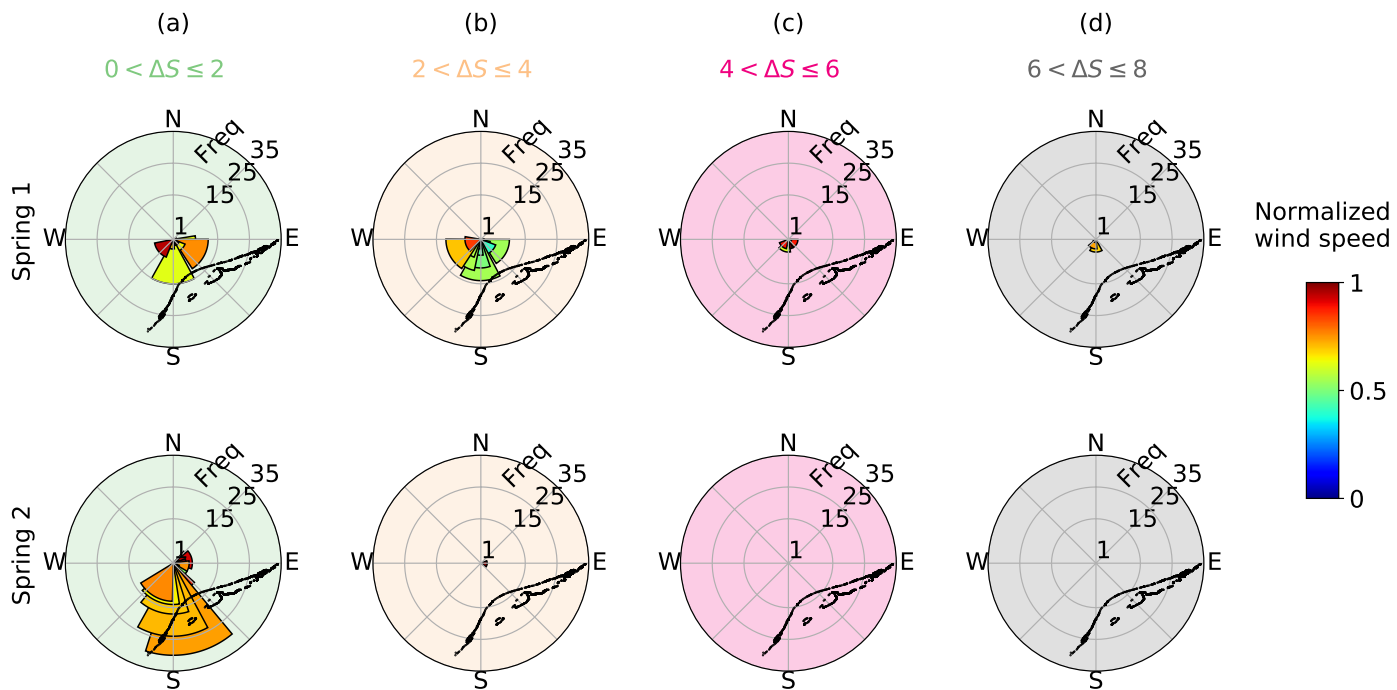


Figure 5.4: Polar histogram of wind direction during Spring 1 (upper panels) and Spring 2 (lower panels) in which the background colors indicate the stratification of the water column based on binned values of ΔS , which range from 0 (well-mixed) to 8 (strongly-stratified) (a-d). The colormap provides a measure of the wind strength. The Sand Engine contour line (1 m above sealevel) is shown in black.

allow the ripples to evolve into a more linguoid plan form (i.e., more asymmetrical geometry). Yet, these differences in the geometrical parameters of the ripples seen in Spring 1 and 2 affected the ripple migration rates that were on average higher during Spring 2.

Spring 2 was marked by an intensification of the wind stress at the sea surface together with intense frontal activity (Figure 5.3b and g). The connection of the bedform dynamics to the fronts and the local wind was assessed through phase-averaging analysis that allowed investigation of the periodicity of the ripple parameters over a M_2 tidal cycle (Figure 5.5) to check to what extent the ripple parameters were governed by the astronomic tide. The results clearly reveal that the ripple migration, height, and geometry fluctuated according to the M_2 tidal cycle, denoting the dominance of the tidal flow in dictating the bedform dynamics. Nonetheless, the along- and cross-shore components of the ripple migration did not entirely behave in agreement with the tidal currents during Spring 2. Such non-tidal behavior is likely due to the wind action and frontal activity that altered the tidal-driven bedform dynamics during Spring 2. As the frontal propagation is markedly shoreward, the cross-shore ripple migration experienced a stronger influence from the fronts. Nonetheless, the cross-shore migration rates were smaller than their alongshore counterparts by approximately a factor of 2. The frontal activity has already been reported as a relevant mechanism for the cross-shore sediment transport of fine material as demonstrated by Horner-Devine et al. [2017] and Flores et al. [2017]. Those studies showed that the cross-shore velocity profile develops strong vertical shear almost immediately upon arrival of the front which is accompanied by high concentration of fine material. Thus, we also expected that such strong vertical shear, during spring tides, may also impact the ripple dynamics.

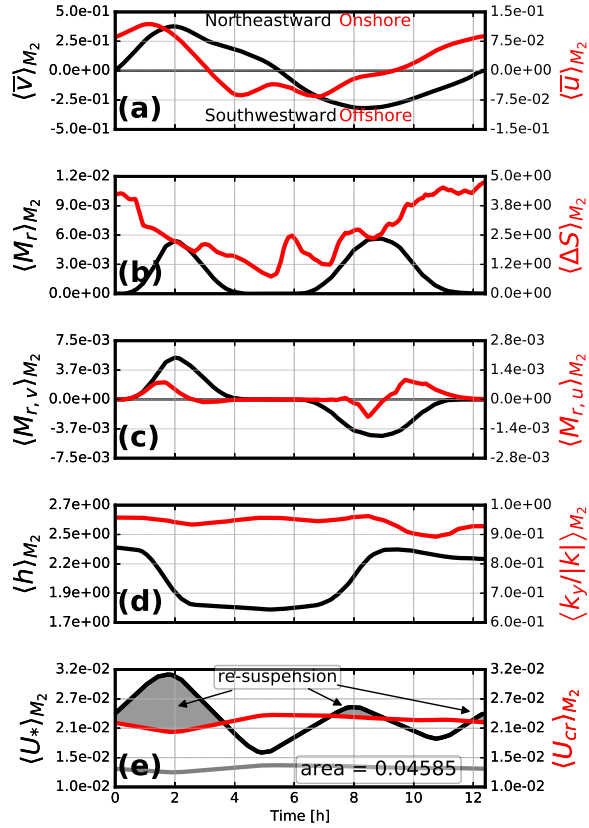
5.3.3 *Semi-diurnal variability*

In the present observations, the mean ripple height manifested a pronounced semi-diurnal variability signifying that the ripple evolution was governed by the ebb and flood currents during Spring 1 and 2 (Figure 5.3c and 5.5). The measurements showed a rapid increase of the mean ripple height approximately 2 hours before low water (LW) as shown by Figure 5.5. From LW to moments before high water (HW) the mean ripple height remained nearly constant, indicating the bedforms had reached quasi-equilibrium dimensions. Moments before HW the mean ripple height decreased

Table 5.1: Descriptive statistics of the main ripple parameters.

	h [cm]				λ [m]				$k_y/ k $				migration rates [cm/s]			
	mean	sd	min	max	mean	sd	min	max	mean	sd	min	max	mean	sd	min	max
Spring 1	2.01	0.28	1.56	2.66	0.43	0.03	0.37	0.52	0.92	0.08	0.44	1.00	1.8×10^{-3}	2.0×10^{-3}	0.0	8.0×10^{-3}
Spring 2	2.27	0.32	1.79	2.92	0.47	0.05	0.38	0.61	0.80	0.21	0.16	1.00	3.4×10^{-3}	4.7×10^{-3}	0.0	26.9×10^{-3}

Spring 1



Spring 2

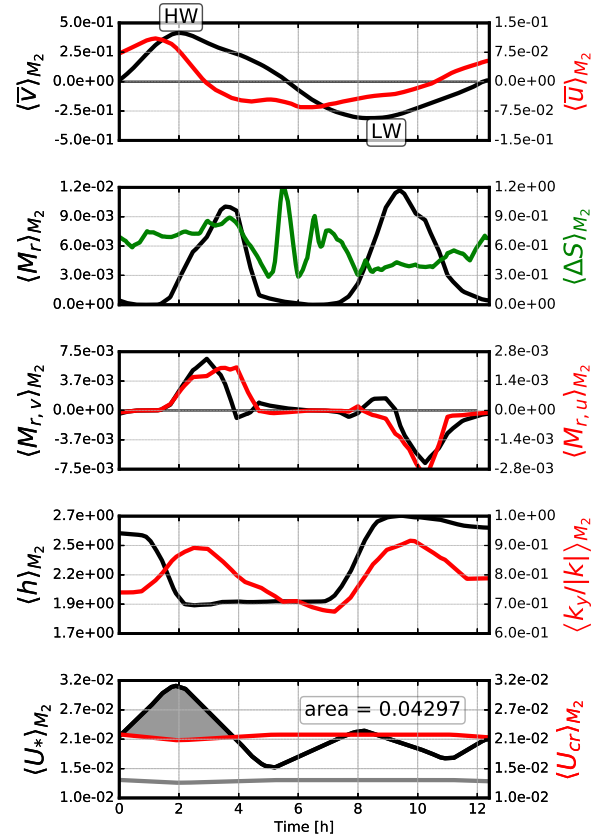


Figure 5.5: (Previous page.) Phase-averaged quantities computed for Spring 1 and 2 periods. (a) Alongshore (black line; left y-axis) and cross-shore (red line; right y-axis) tidal flow; (b) magnitude of ripple migration (black line; left y-axis) and top-to-bottom salinity differences (red/green line; right y-axis); (c) Alongshore (black line; left y-axis) and cross-shore (red line; right y-axis) ripple migration rates; (d) ripple mean height (black line; left y-axis) and $k_y/|k|$ ratio (red line; right y-axis); (e) Total current shear velocity [Grant and Madsen, 1979] (black line; left y-axis), critical shear velocity for initiation of suspended load transport (red line; right y-axis), and critical shear velocity for initiation of sediment motion (gray line; right y-axis). All the quantities were averaged over the M_2 period (=12.42 hours). Note that the vertical scale of the top-to-bottom salinity in (b) is not the same in Spring 2 and therefore it is plotted in green.

rapidly and about 2 hours later the ripple height stabilized again so that the ripples sustained their dimensions until the next LW.

The aforementioned patterns of ripple development are in close agreement with the results presented by Baas et al. [1993] and Baas [1994]. These authors, based on a extensive series of experiments in a flume, showed that the time-span for current ripples to reach equilibrium, for a given grain size, can be in the order of minutes at flow velocities just below the threshold for sediment suspension. Similarly, the present observations revealed that the ripples changed their equilibrium condition when the flood and ebb currents were close to their maxima (i.e., close to HW and LW). The ripples reached the washed-out ripple stage (according to the classification seen in Baas et al. [1993]) close to HW, while they developed towards their equilibrium dimensions close to LW (Figure 5.5d).

Although this semi-diurnal variability of the ripple development presented similar behavior during Spring 1 and 2, the differences in the ripple dimensions and geometry were noticeable in those periods, as previously explained. Besides the impact of the stratified tidal flow on the ripple development, the stratified tidal flow seemed to favor sediment re-suspension which possibly affected the ripple dimensions. By analyzing the critical shear velocity for initiation of suspended load transport (Figure 5.5e), we found that more events of re-suspension took place under the influence of the stratified tidal flow during Spring 1. The gray areas in Figure 5.5e indicate the time during which the near-bed velocity within a tidal cycle exceeded the critical shear velocity for initiation of suspended load transport. In Spring 1 and 2, a relatively large amount of sediment appeared to be picked-up from the bed in the flood phase (from ~ 0 to ~ 6 hours) which eroded the bed and led to the formation of washed-out

ripples. However, events of re-suspension in the ebb phase (from ~ 6 to 12.42 hours) were only detected in Spring 1 as the shear velocity reached values above the threshold for re-suspension. Thus, washed-out ripples might have been more likely to occur during Spring 1 which may explain the nearly constant value of $k_y/|k|$ (Figure 5.5d) as this bedform stage is characterized by a more symmetrical geometry than ordinary current ripples [Baas et al., 1993].

5.3.4 *Ripple migration rates*

The ripple migration was strongly dictated by the alongshore tidal flow so that two distinct peaks of migration rate were observed close to HW and LW whereas the migration ceased around both slack waters (Figures 5.3f and 5.5b). As the ripples were mostly washed out during the flood phase, higher migration rates were observed during the ebb phase. To investigate the preferential migration pathways, we examined the cumulative migration rates as depicted on Figure 5.6a and b. During Spring 1, the alongshore net migration rates exhibited a steadily downward sloping curve implying a consistent trend of a southward net migration (Figure 5.6a). The slope of the curve during Spring 2 presented slight changes in direction suggesting the dominant forcings acted differently from those of Spring 1 (discussed further in this session). The cross-shore component of the net migration rate also behaved differently in Spring 1 and 2 (Figure 5.6b). A consistent upward sloping curve was observed during Spring 1 implying a shoreward tendency of the ripple migration. The slope of the curve in Spring 2 seemed relatively milder indicating the net migration rates were smaller. The net ripple migration during Spring 2 appeared to be not significant, although the gross migration rates were relatively higher compared to those observed in Spring 1.

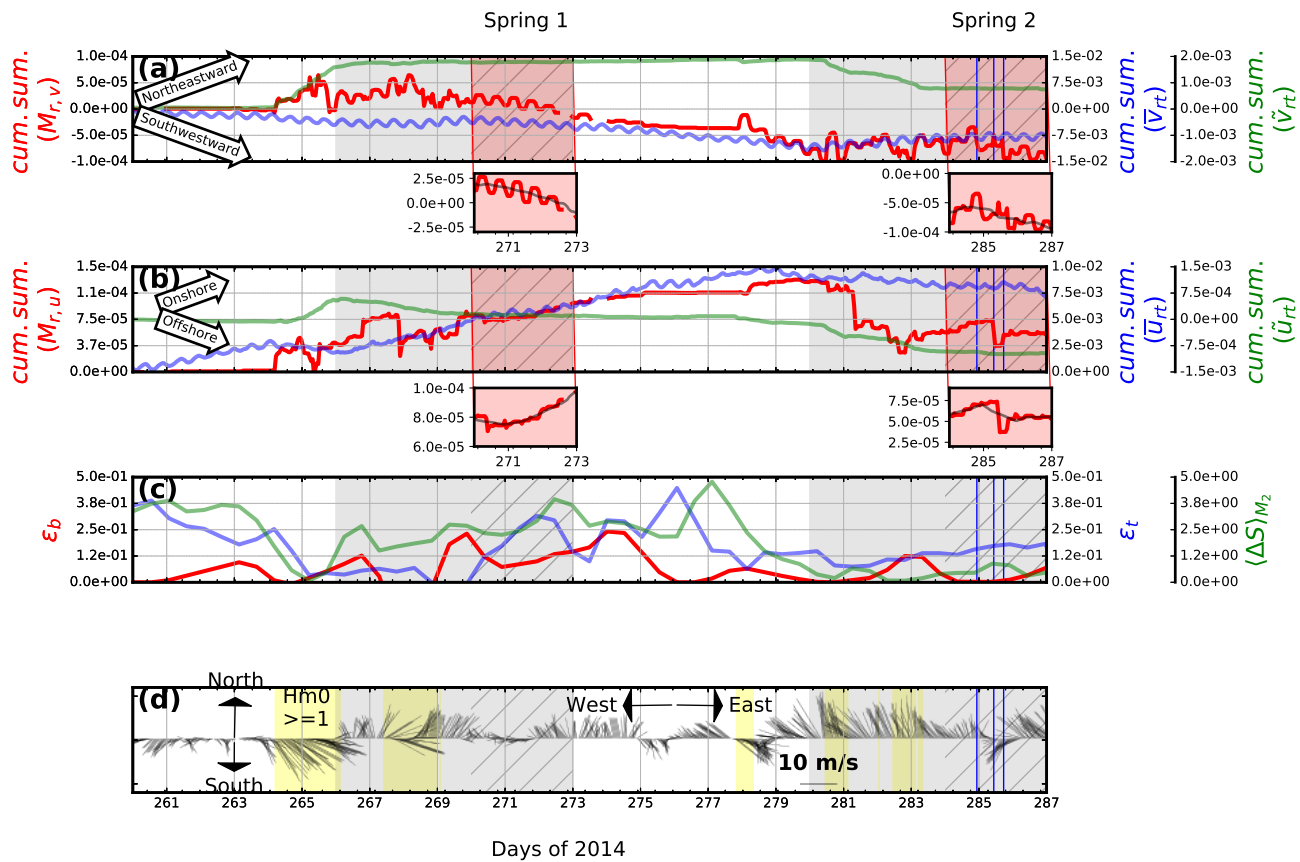


Figure 5.6: (Previous page.) Time series of cumulative fluxes of (a) alongshore ripple migration rates (red line), mean residual transport velocities (blue line) and wave-driven residual transport velocities (green line); (b) same as (a) but in the cross-shore; (c) Ellipticity of the ripple migration (red line), ellipticity of the tidal flow (blue line) and top-to-bottom salinity difference smoothed over a M_2 period; (d) Stick plot of the wind series. The hatched gray lines show Spring 1 and Spring 2. The red panels on the bottom of (a) and (b) show a zoomed in view of the migration rates during Spring 1 and 2. The yellow areas in (d) indicate the periods where the significant wave height was ≥ 1 m. The vertical blue lines (a-d) indicate the peaks observed in the ripple migration rates during Spring 2.

Another important aspect was the prevalence of the tidal flow over wave-driven flow throughout the series (Figure 5.6a and b). This could be observed through the cumulative tidal and wave-driven residual transport velocities (Equation 4.2) that are the velocities associated with the asymmetries of the nonlinear parameters responsible for the (net) sediment transport [Reniers et al., 2004]. In general, the cumulative ripple migration rates were in agreement with the cumulative tidal residual transport velocities confirming the dominance of the tidal currents in moulding the bed. The exceptions were observed during periods when the significant wave heights were higher than 1 m (see yellow areas in Figure 5.6d).

The net ripple migration during Spring 1 can be attributed to the asymmetries in velocity due to stratification. This is more evident in the cross-shore components (Figure 5.6b) given the enhancement of the cross-shore tidal amplitude as the tidal current ellipses develop a more circular pattern. The period of wind intensification accompanied by the passage of plume fronts also impacted the ripple dynamics as seen by sudden jumps in the net migration during Spring 2 (see vertical blue lines in Figure 5.6). Nonetheless, these events lasted for a short period of time (less than a tidal cycle) and did not change the overall trend of the net ripple migration. It is worth mentioning that the front intrusion into the nearshore can produce complex hydrodynamic structures [e.g., Meirelles et al., 2018a] and has a paramount role in the cross-shore sediment transport [e.g., Horner-Devine et al., 2017, Flores et al., 2017] in the study area.

A typical way to investigate the behavior of the stratified tidal flow is by means of tidal current ellipticity, which determines how circular the tidal motion is [e.g., Souza and Simpson, 1996, De Boer et al., 2006]. We extended this analysis to the bedforms so that the ellipticity of the ripple migration was computed aiming at gaining insight on how the bedforms respond to the stratified tidal flow. The results showed a reasonably

good agreement of the ellipticity of the tidal flow as well as the ripple migration with stratification (Figure 5.7). In general, the ellipticity of the tidal flow obeyed the behavior of the vertical stratification and, to a lesser extent, so did the ellipticity of the ripple migration, except during neap tides in which the migration rates were negligible. This correlation between the ripple migration ellipticity and stratification supports the hypothesis of current direction hindering the development of ripples.

To further explore the influence of stratification on the ripples, we compared the ellipticity against stratification as depicted by Figure 5.7. During Spring 1, marked by strong vertical stratification, the tidal motion became more circular resulting in an increase of the ellipticity of the tidal flow (Figure 5.7a). This circular nature of the tidal currents appeared to favor a more circular motion of the bedforms as the ellipticity of the ripple migration was high during Spring 1 (Figure 5.7b). The relatively smaller values of the bedform ellipticity is likely owed to the time needed for the ripples to adjust to the circular motion of the overlying flow. During Spring 2, however, the low values of the ellipticity of the ripple migration indicated there is no significant circular motion over the tidal cycle in the absence of ambient stratification, i.e., the ripple movement was more rectilinear.

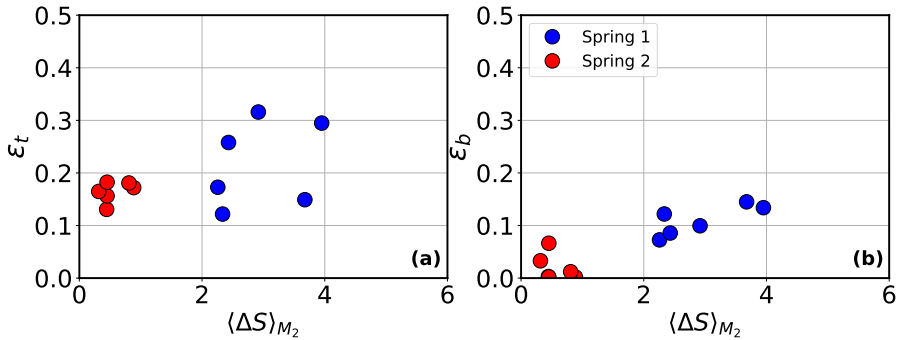


Figure 5.7: Scatter plot of (a) tidal current ellipticity against top-to-bottom salinity; and (b) ripple ellipticity against top-to-bottom salinity during Spring 1 (blue circles) and 2 (red circles).

5.4 DISCUSSION

The results of the present investigation suggest that vertical stratification yields different geometrical patterns of the bedforms and changes the preferential ripple migration pathways. The fundamental difference of the stratified tidal flow does not lie in

the strength of the flow but in the circular aspect of its motion. The fact that the equilibrium ripple dimensions are a function of time and flow strength [Baas et al., 1993, Baas, 1994] might imply the ripples during Spring 1 had their development hindered by the continuous change in direction of the stratified tidal flow. Such conditions facilitated the formation of more symmetric ripples (Figures 5.3e and 5.5d). This scenario would explain the re-suspension events seen in Spring 1 which seem to agree with the findings in flume experiments by Baas and De Koning [1995]. The authors found that the suspended-sediment concentration decreases linearly with increasing equilibrium ripple heights.

Concerning the net ripple migration, the asymmetries of the tidal flow imparted by stratification appeared to influence the distance traveled by the ripples over Spring 1 and 2. The diagram seen in Figure 5.8 illustrates the net displacement of the stratified and non-stratified near-bed currents and their impact on the net ripple migration. The stratified flow during Spring 1 produced a southeasterly drift whereas the non-stratified flow during Spring 2 generated a northwesterly drift that in fact seemed to be strongly influenced by the offshore winds and the front passages (Figure 5.3b and g) so that an offshore residual was observed. The estimated net ripple migration revealed southward residual migration which supports the hypothesis that flood currents (northeastward currents) promote more re-suspension events that are responsible for eroding the bed. Regarding the effects of stratification, the response of the bed was closely related to the behavior of the stratified tidal flow so that a markedly onshore residual was observed during Spring 1. During Spring 2, the net ripple migration was about 7 times smaller than that of Spring 1. Nonetheless, the peaks in the migration rates associated with the wind action and intrusion of the plume front led to a significant gross ripple movement which strongly affected the cross-shore ripple migration. From these results, it is hypothesized that the non-linearities of the stratified tidal flow potentially enhance the net ripple migration even though the daily migration rates were relatively smaller.

5.4.1 *Impact on the sediment transport*

To gain some first insights on the effects of the bedform dynamics with respect to the sediment transport, we examined the behavior of the bed- and suspended load sediment transport. The calculations for the sediment transport using the field data followed the methodology described in Section 4.2.3. Additionally, we compared

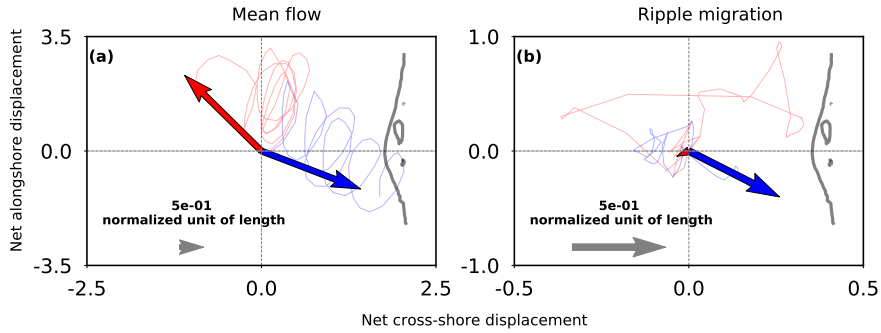


Figure 5.8: Net displacement, in normalized units of length, of (a) the mean flow; and (b) the ripple migration over Spring 1 (blue arrows) and Spring 2 (red arrows). The daily displacement of the mean flow (in a) and the ripple migration (in b) are shown by the blue (Spring 1) and red (Spring 2) lines. The approximated orientation of the coastline is represented by the Sand Engine contour.

the bedload transport calculations to the predictions of a one-dimensional (vertical) sediment transport model [Neumeier et al., 2008] which is based on the formulation of van Rijn [1993] for the bedload transport rate. This comparison aimed to verify whether there was large discrepancies between the predicted and observed bedload transport.

The results shown in Figure 5.9 revealed that the predicted and observed bedload transport followed in general the same behavior throughout the series. Although there was a good agreement, the observed bedload presented relatively higher values especially during periods of high waves (e.g., day 265) and frontal activity (e.g., day 286). According to these results, the model of Neumeier et al. [2008] seemed to underpredict the magnitude of the bedload transport rates in periods of high bed shear stress. Nevertheless, this comparison implies the bedload transport in the Dutch inner shelf might be largely due to the migrating ripples.

Regarding the sediment transport rates, we observed that the suspended load transport rates were $\mathcal{O}(10^1)$ greater than the bedload transport rates (Figure 5.10a and b). Naturally, the bedload transport due to migrating ripples obeyed the same behavior of the ripple migration rates (discussed in Section 5.3.4). This means that during Spring 1, the net bedload transport rate was onshore- and southwest-directed as seen by the slopes of the Mean curves in Figure 5.10c and d. In Spring 2, the mild slope of the curves suggested that net bedload transport seemed to be very small (except during

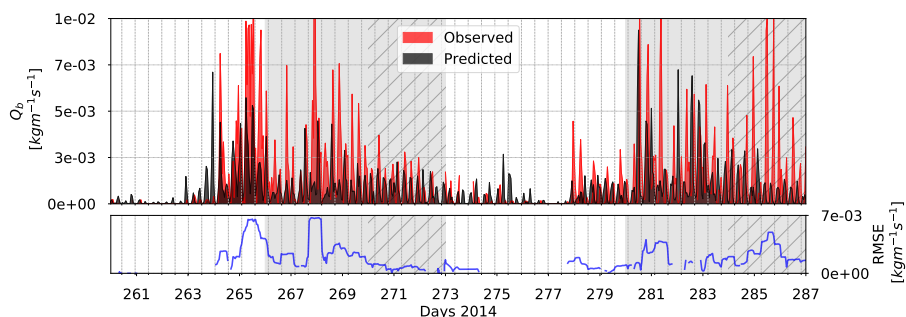


Figure 5.9: Comparison of the bedload transport rates estimated from the measurements and predicted from a sediment transport model (upper panel); and the corresponding root-mean-square-error (lower panel). The spring tides are marked by the gray areas and the hatches inside the gray areas indicate Spring 1 and Spring 2.

the frontal activity), though the gross bedload transport (Figure 5.10a and b) were markedly higher.

The examination of the suspended transport rates included all days of the first and the second spring tide (gray areas in Figure 5.10). The reason for that is because the ABS captured only the first day of the Spring 2 impeding a proper comparison against Spring 1. The results for the first spring showed that relatively high gross alongshore suspended transport rates (Figure 5.10a) did not lead to a relatively high net alongshore suspended transport rates as seen by the mild slope of the curve Figure 5.10c. The net alongshore suspended transport rates during the second spring tide (well-mixed conditions) exhibited a clearer north-directed trend as the cumulative rates presented a positive slope (Figure 5.10c). With respect to the cross-shore suspended load rates, the results showed a onshore-directed transport under stratified conditions (first spring) and weakly offshore-directed transport under well-mixed conditions (second spring).

The net bedload transport was always south-directed regardless of stratification due to the higher amount of sediment put into suspension during the flood stage of the tide (i.e., northeastward currents) which in turn favored the suspended load transport. As the stratified tidal flow promotes more re-suspension of sand from the bed during the ebb tide (Figure 5.5e), the net alongshore suspended load was reduced under stratified conditions. Although we observed that the near-bed stratified currents tended to be southeast-directed (Figure 5.8), the net suspended load transport rates tended to be northeast-directed. This could be explained by the ebb currents not being

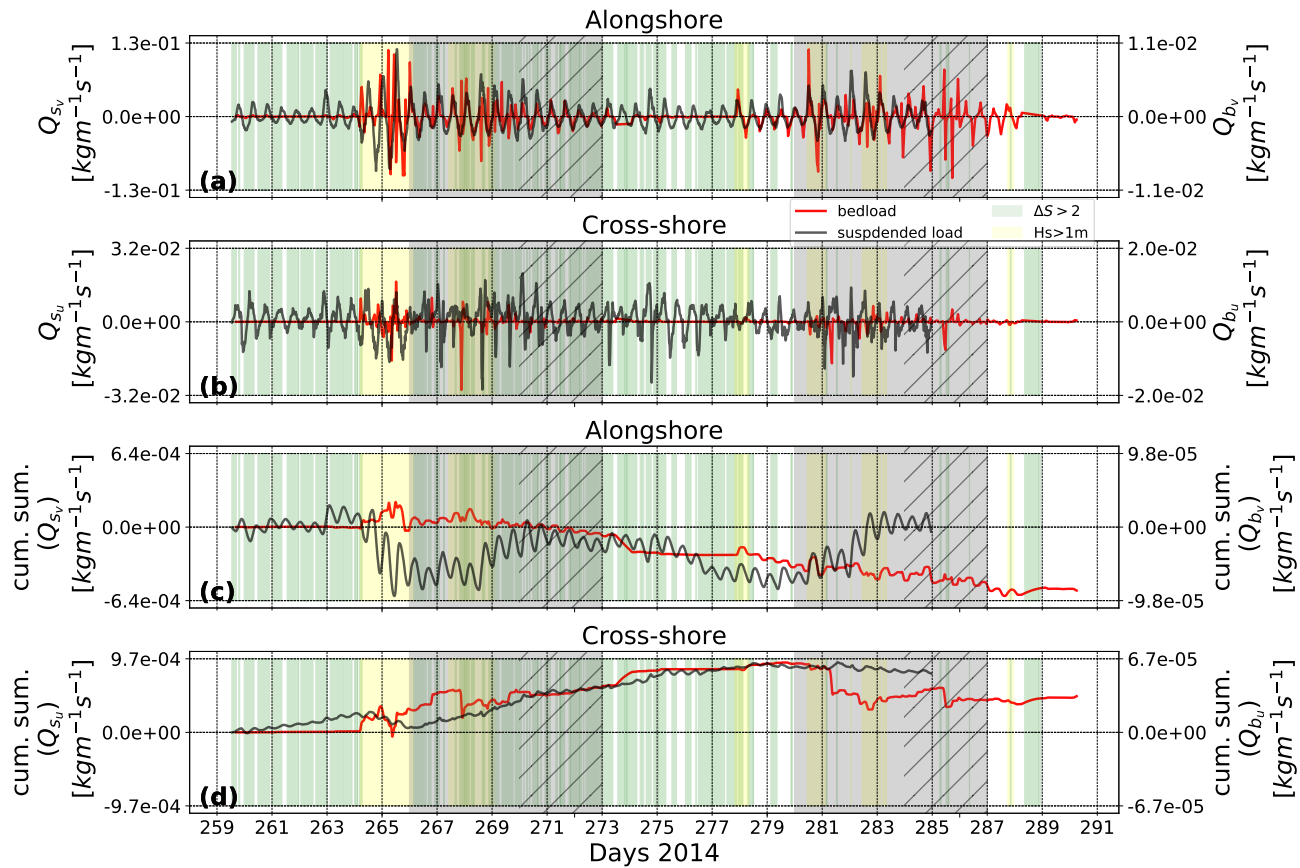


Figure 5.10: (Previous page.) Bed- and suspended load series calculated from the observations. (a) alongshore bed- and suspended load transport rates; (b) cross-shore bed- and suspended load transport rates; (c) cumulative alongshore bed- and suspended load transport rates; and (d) cumulative cross-shore bed- and suspended load transport rates. The spring tides are marked by the gray areas and the hatches inside the gray areas indicate Spring 1 and Spring 2. The green areas indicate $\Delta S > 2$ and the yellow areas indicate waves higher than 1 m.

able to sustain the sand particles into suspension long enough so that the net alongshore suspended transport obeyed the relatively stronger flood currents. However, the cross-shore suspended transport was considerably higher and onshore-directed due to development of the cross-shore exchange currents under stratified conditions (as discussed in Chapter 2).

The behavior of the bed- and suspended load transport under well-mixed and stratified conditions is summarized in Figure 5.11. We conjecture that the stratified flow fostered the shoreward sediment transport as both bedload and suspended load. Moreover, the bedload and suspended load transports were opposing in the alongshore direction because most of the suspended load occur during flood tide and most of the bedload occur during ebb tide. The suspended load transport was by far the most important transport mode in the measurement site.

5.5 CONCLUSIONS

The present work describes the bedform dynamics by tides under the influence of the Rhine River ROFI. The bedforms in the measurement site are strongly controlled by tides so that their behavior exhibits not only a spring-neap signature, but also a distinct semi-diurnal fluctuation. Under the influence of the Rhine ROFI (i.e., stratification), the bedform mean dimensions are reduced, indicating that their development is affected by the stratified tidal flow. We show that the circular nature of the tidal flow, given by tidal current ellipticity, is likely to be the mechanism responsible for hindering the bedform evolution because of the continuous adjustment of the ripples to the changes in the flow. Consequently, less developed bedforms are formed that are characterized by a more symmetrical geometry. The observations suggest that the ripple migration rates are diminished as more sediment is picked up from the bed during stratified periods.

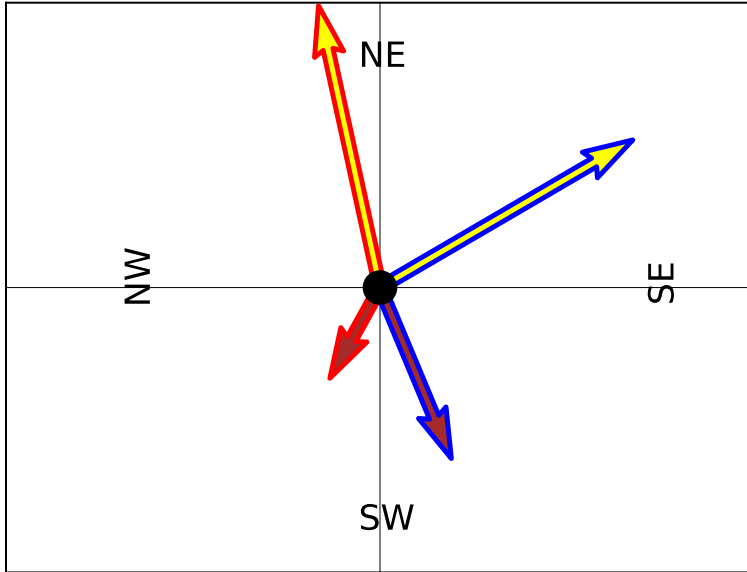


Figure 5.11: Schematic representation of the bedload (brown arrows) and suspended load (yellow arrows) under stratified (blue lines) and non-stratified (red lines) conditions. Vectors are not to scale.

Due to the asymmetries imparted by stratification, the tidal flow undergoes a relatively larger drift due to the irregular ellipsoidal tidal excursion observed during stratified periods. This residual stratified tidal current seems to allow the ripples to travel longer distances, even though they present reduced dimensions. On the other hand, the larger ripple dimensions observed during the non-stratified period indicate that a greater volume of sand is in movement but, as the tidal drift is smaller, the net ripple migration is also smaller. These asymmetries of the tidal flow are also important in terms of migration direction as the ripples seem to migrate shoreward during stratified conditions and seaward during well-mixed conditions.

The observations suggest that the bedload and suspended load transports are always onshore-directed under the effects of the stratified tidal flow. Independent of stratification, the net alongshore bedload transport is permanently south-directed, whereas the net alongshore suspended load permanently north-directed. The suspended load transport rates are $\mathcal{O}(10^1)$ greater than the bedload transport rates.

The present work explores the connection between stratification and bedforms. The stratified tidal flow is an important agent governing the ripple morphology which in

turn can affect the ripple migration rates that are intrinsically related to the bedload transport mode. The re-suspension of sediment from the bed is also impacted by the stratified tidal flow owing to changes in the ripple asymmetries. Finally, we showed that stratification affects not only the magnitude of the ripple migration but also its direction.

CONCLUSIONS

This research aimed at gaining new insights on the physical mechanisms that drive the seafloor (bedforms) dynamics and its intrinsic sediment transport under the influence of the Rhine river ROFI based on the following hypothesis:

Hypothesis

The stratified tidal flow modifies the geometry and dynamics of the small scale bedforms which ultimately affects the bedload and suspended load sediment transport.

The answers to the research questions validate this hypothesis as seen below:

Research Question 1 - RQ1 (Chapters 2 and 3)

To what extent does the stratified tidal flow control the inner shelf hydrodynamics?

Answer: the present study has demonstrated, based on observations and revisiting the past literature, that tidal straining and other baroclinic processes strongly affect the structure of the tidal currents, especially in the cross-shore direction. The proximity to the Rhine River mouth is a key condition that allows these baroclinic processes to be extended to the nearshore even during spring tides.

RQ1.1

What is the impact of the Sand Engine on the stratified tidal flow?

Answer: the Sand Engine does not present an appreciable impact on the baroclinic tide, especially on the behavior of the cross-shore exchange currents. However, the curvature of the Sand Engine might have played a more significant role in the local dynamics during the first three years after the Sand Engine was built, and thus contributed to cross-shore exchange currents. The eddies observed at the flanks of the Sand Engine are resolved by the barotropic tidal flow [Radermacher et al., 2016], so that the structure of the baroclinic tidal flow is believed to be preserved seaward of the Sand Engine.

RQ1.2

What is the contribution of the different terms of the momentum equation to the cross-shore flow?

Answer: the observed centrifugal acceleration promoted by the Sand Engine curvature is not large enough to balance the cross-shore baroclinic pressure gradient. Apart from centrifugal acceleration and baroclinic forcing, the advective acceleration, Coriolis acceleration and vertical dissipation appears to not significantly affect the behavior of the cross-shore exchange currents, which is greatly governed by fluctuations of the baroclinic pressure gradient. Nonetheless, the magnitude of the local time variation term reveals there is a tendency for the flow to accelerate, implying the existence of a local imbalance between the driving forces.

RQ1.3

What is the shoreward extent of the stratified cross-shore flow?

Answer: the occurrence of stratification in depths as shallow as 6 m associated with a relatively strong cross-shore shear reveals that tidal straining and other baroclinic processes can occur in shallow waters even under the stirring effects of waves and wind.

RQ1.4

How does stratification affect the bed shear stress?

Answer: the influence of stratification on the hydrodynamics is translated into near-bed shear velocity in the layer immediately above the seafloor. The tide-

induced bed shear stress is able to periodically agitate the bed near the peaks of flood and ebb cycles mostly during spring tides. Under stratified conditions, relatively high values of bed shear stress are sustained for a prolonged period of time.

Research Question 2 - RQ2 (Chapter 4 and 5)

How does the near-bed stratified tidal flow affect the bedform dynamics and sediment pick-up from the seafloor?

Answer: the bedform dynamics under the influence of the Rhine River ROFI is strongly controlled by tides so that their behavior exhibits not only a spring-neap signature, but also a distinct semi-diurnal fluctuation. Under the influence of the Rhine ROFI, the bedform mean dimensions are reduced, indicating that their development is affected by the stratified tidal flow. The circular nature of the tidal flow, given by tidal current ellipticity, is likely to be the mechanism responsible for hindering the bedform evolution because of the continuous adjustment of the ripples to the changes in the flow.

RQ2.1

What bed form types are found off the South-Holland coast?

Answer: current ripples, C, are dominant in the Dutch inner shelf. The frequency of occurrence of transitional bed types (Cw, WC and Wc) combined ranked second. Wave ripples prevail when $H_s \geq 1$ m. Most of the poorly developed ripples are found during neap tide, while the bed is notably active during spring tide.

RQ2.2

Which mechanisms control the bedform dynamics under stratified conditions?

Answer: The circular nature of the tidal flow, given by tidal current ellipticity, is likely to be the mechanism responsible for hindering the bedform evolution because of the continuous adjustment of the ripples to the changes in

the flow. Moreover, less developed bedforms are formed which are characterized by a more symmetrical geometry. Consequently, more sediment pick-up from the bed is observed under the influence of ambient stratification, because the suspended-sediment concentration decreases linearly with increasing equilibrium ripple heights [Baas and De Koning, 1995].

RQ2.3

How does stratification impact the bedform migration rates?

Answer: due to the asymmetries imparted by stratification, the tidal flow undergoes a relatively larger drift due to the irregular ellipsoidal tidal excursion observed during stratified periods. This residual stratified tidal current seems to allow the ripples to travel longer distances, even though they present reduced dimensions. On the other hand, the larger ripple dimensions observed in well-mixed conditions indicate that a greater volume of sand is in movement but, as the tidal drift is smaller, the net ripple migration is also smaller. These asymmetries of the tidal flow are also important in terms of migration direction as the ripples seem to migrate shoreward during stratified conditions and seaward during well-mixed conditions.

RQ2.4

How does bedform dynamics affect the sediment transport modes?

Answer: the stratified tidal flow favors the gross suspended load transport over the bedload transport as more sediment is picked up from the bed over a tidal cycle. Independent of stratification, the net alongshore bedload transport is permanently southwest-directed, whereas the net alongshore suspended load is permanently north-directed. Ambient stratification promotes onshore-directed bed- and suspended load net sediment transport. The suspended load transport rates are $\mathcal{O}(10^1)$ greater than the bedload transport rates.

The answers to the research questions form a conceptual understanding of the influence of stratification on sediment transport in the inner shelf. The schematic diagram seen in Figure 6.1 outlines the behavior of bed- and suspended load transport with and without stratification. Stratification magnifies the gross suspended load transport,

but the net suspended transport is smaller due to the higher transport rates observed during the ebb phase. Stratification also magnifies the onshore-directed bed- and suspended load transports. In the absence of stratification the net cross-shore transport is offshore-directed, though it presents very small magnitudes. The directions of the net bed- and suspended load transports are opposing with respect to their alongshore components.

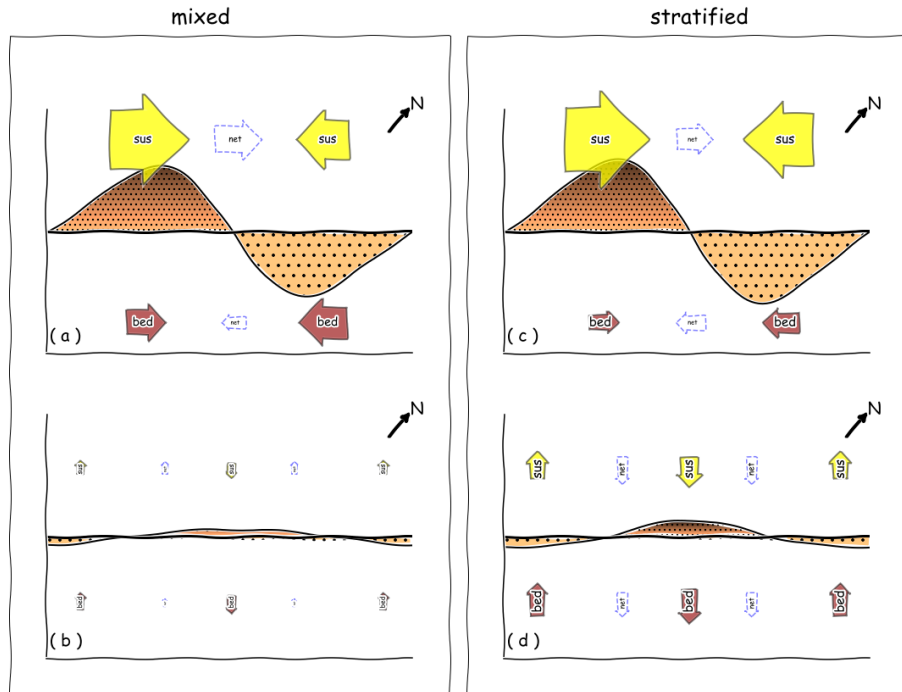


Figure 6.1: Schematic diagram of the influence of stratification on the bed- (brown arrows) and suspended (yellow arrows) load transport in the alongshore (a-b) and cross-shore (c-d) directions. The blue dashed arrows represent the net transports and the North arrow is shown in black.

The present work investigates the impact of the stratified tidal flow on the morphodynamics of the Dutch inner shelf. The results are mostly based on field observations. Although the vast dataset allowed a detailed examination of the processes of interest, the implementation of a 3D numerical model would enable to extend the analysis of the impact of the stratified tidal flow on the morphodynamics. Efforts to adequately simulate the details of this flow using Delft3D-FM, which would have provided an extension of the results to longer timescales and a wider range of conditions, have failed thus far. The timing and magnitude of the baroclinic forcing that is so key to this

setting results from a complex stratified tidal flow separation and frontogenesis process closer to the river mouth, which has proved to be hard to replicate with enough fidelity in the model to make a meaningful comparison with the field observations. More efforts are needed to implement a numerical model able to properly simulate the sediment transport under the influence of the stratified tidal flow.

BIBLIOGRAPHY

- M. J. Alae, G. Ivey, and C. Pattiaratchi. Secondary circulation induced by flow curvature and coriolis effects around headlands and islands. *Ocean Dynamics*, 54(1): 27–38, 2004.
- C. Amos and M. Collins. The combined effects of wave motion and tidal currents on the morphology of intertidal ripple marks: the wash, uk. *Journal of Sedimentary Research*, 48(3), 1978.
- C. Amos, A. Bowen, D. Huntley, and C. Lewis. Ripple generation under the combined influences of waves and currents on the canadian continental shelf. *Continental Shelf Research*, 8(10):1129 – 1153, 1988. ISSN 0278-4343. doi: [https://doi.org/10.1016/0278-4343\(88\)90016-7](https://doi.org/10.1016/0278-4343(88)90016-7). URL <http://www.sciencedirect.com/science/article/pii/0278434388900167>.
- O. B. Andersen. Shallow water tides in the northwest european shelf region from topex/poseidon altimetry. *Journal of Geophysical Research: Oceans*, 104(C4):7729–7741, 1999. ISSN 2156-2202. doi: 10.1029/1998JC900112. URL <http://dx.doi.org/10.1029/1998JC900112>.
- J. H. Baas. A flume study on the development and equilibrium morphology of current ripples in very fine sand. *Sedimentology*, 41(2):185–209, 1994.
- J. H. Baas and H. De Koning. Washed-out ripples: their equilibrium dimensions, migration rate, and relation to suspended-sediment concentration in very fine sand. *Journal of Sedimentary Research*, 65(2), 1995.
- J. H. Baas, A. P. Oost, O. K. Sztano, P. L. Boer, and G. Postma. Time as an independent variable for current ripples developing towards linguoid equilibrium morphology. *Terra Nova*, 5(1):29–35, 1993.
- J. H. Baas, J. L. Best, and J. Peakall. Predicting bedforms and primary current stratification in cohesive mixtures of mud and sand. *Journal of the Geological Society*, 173(1):12–45, 2016.

- J. C. Bathurst, C. R. Thorne, and R. D. Hey. Direct measurements of secondary currents in river bends. *Nature*, 269:504–506, 1977. doi: <http://dx.doi.org/10.1038/269504a0>.
- J. Becherer, M. T. Stacey, L. Umlauf, and H. Burchard. Lateral circulation generates flood tide stratification and estuarine exchange flow in a curved tidal inlet. *Journal of Physical Oceanography*, 45(3):638–656, 2015.
- P. Bell and P. Thorne. Application of a high resolution acoustic scanning system for imaging sea bed microtopography. In *Electronic Engineering in Oceanography, 1997. Technology Transfer from Research to Industry., Seventh International Conference on*, pages 128–133. IET, 1997.
- K. F. E. Betteridge, P. S. Bell, P. D. Thorne, and J. J. Williams. Evaluation of a triple-axis coherent doppler velocity profiler for measuring near-bed flow: A field study. *Journal of Atmospheric and Oceanic Technology*, 23(1):90–106, 2006. doi: 10.1175/JTECH1834.1. URL <https://doi.org/10.1175/JTECH1834.1>.
- J. M. Brown, R. Bolaños, M. J. Howarth, and A. J. Souza. Extracting sea level residual in tidally dominated estuarine environments. *Ocean Dynamics*, 62(7):969–982, 2012.
- M. Buijsman and H. Ridderinkhof. Variability of secondary currents in a weakly stratified tidal inlet with low curvature. *Continental Shelf Research*, 28(14):1711 – 1723, 2008. ISSN 0278-4343. doi: <http://dx.doi.org/10.1016/j.csr.2008.04.001>. URL <http://www.sciencedirect.com/science/article/pii/S0278434308001520>.
- R. J. Chant and R. E. Wilson. Secondary circulation in a highly stratified estuary. *Journal of Geophysical Research: Oceans*, 102(C10):23207–23215, 1997. ISSN 2156-2202. doi: 10.1029/97JC00685. URL <http://dx.doi.org/10.1029/97JC00685>.
- Codiga, D. L. Unified tidal analysis and prediction using the UTide Matlab functions (Python version). Technical report 2011-01, University of Rhode Island, Graduate School of Oceanography, University of Rhode Island, Narragansett, RI, 2011.
- P. Cowell, M. Stive, A. Niedoroda, H. de Vriend, D. Swift, G. Kaminsky, and M. Capobianco. The coastal-tract (part 1): a conceptual model approach to aggregated modeling of low-order coastal change. *Journal of Coastal Research*, 19(4):812–827, 2003a.
- P. J. Cowell, M. J. Stive, A. W. Niedoroda, H. J. de Vriend, D. J. Swift, G. M. Kaminsky, and M. Capobianco. The coastal-tract (part 1): a conceptual approach to aggregated modeling of low-order coastal change. *Journal of Coastal Research*, pages 812–827, 2003b.

- G. J. De Boer, J. D. Pietrzak, and J. C. Winterwerp. On the vertical structure of the Rhine region of freshwater influence. *Ocean dynamics*, 56(3-4):198–216, 2006.
- G. J. De Boer, J. D. Pietrzak, and J. C. Winterwerp. Using the potential energy anomaly equation to investigate tidal straining and advection of stratification in a region of freshwater influence. *Ocean Modelling*, 22(1):1–11, 2008.
- G. J. De Boer, J. D. Pietrzak, and J. C. Winterwerp. SST observations of upwelling induced by tidal straining in the Rhine ROFI. *Continental Shelf Research*, 29(1):263 – 277, 2009. ISSN 0278-4343. doi: <http://dx.doi.org/10.1016/j.csr.2007.06.011>. URL <http://www.sciencedirect.com/science/article/pii/S0278434307001847>. Physics of Estuaries and Coastal Seas: Papers from the PECS 2006 Conference.
- W. P. de Ruijter, A. W. Visser, and W. Bos. The Rhine outflow: a prototypical pulsed discharge plume in a high energy shallow sea. *Journal of Marine Systems*, 12(1): 263–276, 1997.
- M. A. de Schipper, S. de Vries, G. Ruessink, R. C. de Zeeuw, J. Rutten, C. van Gelder-Maas, and M. J. Stive. Initial spreading of a mega feeder nourishment: Observations of the Sand Engine pilot project. *Coastal Engineering*, 111:23–38, 2016.
- H. J. de Vriend, M. van Koningsveld, S. G. Aarninkhof, M. B. de Vries, and M. J. Baptist. Sustainable hydraulic engineering through building with nature. *Journal of Hydro-environment Research*, 9(2):159 – 171, 2015. ISSN 1570-6443. doi: <http://dx.doi.org/10.1016/j.jher.2014.06.004>. URL <http://www.sciencedirect.com/science/article/pii/S1570644314000653>. Special Issue on Environmental Hydraulics.
- De Zandmotor. The Sand Motor: looking back at 2.5 years of building with nature. Technical report, Rijkswaterstaat, 2014. URL <http://www.dezandmotor.nl>.
- R. Dean and R. Dalrymple. *Coastal Processes with Engineering Applications*. Cambridge University Press, 2004. ISBN 9780521602754.
- P. Drinker. *Boundary shear stresses in curved trapezoidal channels*. PhD thesis, Massachusetts Institute of Technology, 1961.
- R. P. Flores, S. Rijnsburger, A. R. Horner-Devine, A. J. Souza, and J. D. Pietrzak. The impact of storms and stratification on sediment transport in the rhine region of freshwater influence. *Journal of Geophysical Research: Oceans*, 2017. ISSN 2169-9291. doi: 10.1002/2016JC012362. URL <http://dx.doi.org/10.1002/2016JC012362>.

- D. C. Fugate, C. T. Friedrichs, and L. P. Sanford. Lateral dynamics and associated transport of sediment in the upper reaches of a partially mixed estuary, Chesapeake Bay, USA. *Continental Shelf Research*, 27(5):679 – 698, 2007. ISSN 0278-4343. doi: <http://dx.doi.org/10.1016/j.csr.2006.11.012>.
- C. J. R. Gerret and R. H. Loucks. Upwelling along the Yarmouth shore of Nova Scotia. *J. Fish. Res. Board of Can.*, 33:116–117, 1976.
- W. R. Geyer. Three-dimensional tidal flow around headlands. *Journal of Geophysical Research: Oceans (1978–2012)*, 98(C1):955–966, 1993.
- W. R. Geyer, R. P. Signell, and G. C. Kineke. Lateral trapping of sediment in a partially mixed estuary. In J. Dronkers and M. B. A. M. Scheffers, editors, *Physics of Estuaries and Coastal Seas*, chapter 2, pages 115–124. 1998.
- W. D. Grant and O. S. Madsen. Combined wave and current interaction with rough bottom. *Journal of Geophysical Research*, 84:1797–1808, 1979.
- W. D. Grant and O. S. Madsen. The continental shelf bottom boundary layer. In M. Van Dyke, editor, *Annual Review of Fluid Mechanics*, chapter 18, pages 265–305. 1986.
- B. Grasmeijer, M. Kleinhans, and T. Dolphin. *Measured and Predicted Suspended Sand Transport on a Sandy Shoreface*, chapter 85, pages 1–13. 2006.
- M. Henriquez, S. Meirelles, A. Horner-Devine, J. D. Pietrzak, A. Souza, and M. J. F. Stive. Cross-shore sand transport by tide on the shoreface. Submitted to the *Journal of Geophysical Research*, 2016.
- T. S. Hopkins. A note on the geostrophic velocity field referenced to a point. *Continental Shelf Research*, 16(12):1621 – 1630, 1996. ISSN 0278-4343. doi: [http://dx.doi.org/10.1016/0278-4343\(95\)00080-1](http://dx.doi.org/10.1016/0278-4343(95)00080-1). URL <http://www.sciencedirect.com/science/article/pii/0278434395000801>.
- A. R. Horner-Devine, R. D. Hetland, and D. G. MacDonald. Mixing and transport in coastal river plumes. *Annual Review of Fluid Mechanics*, 47:569–594, 2015.
- A. R. Horner-Devine, J. D. Pietrzak, A. J. Souza, M. A. McKeon, S. Meirelles, M. Henriquez, R. P. Flores, and S. Rijnsburger. Cross-shore transport of nearshore sediment by river plume frontal pumping. *Geophysical Research Letters*, 2017. ISSN 1944-8007.

- doi: 10.1002/2017GL073378. URL <http://dx.doi.org/10.1002/2017GL073378>. 2017GL073378.
- K. M. H. Huijts, H. M. Schuttelaars, H. E. de Swart, and A. Valle-Levinson. Lateral entrainment of sediment in tidal estuaries: An idealized model study. *Journal of Geophysical Research: Oceans*, 111(C12), 2006. ISSN 2156-2202. doi: 10.1029/2006JC003615. URL <http://dx.doi.org/10.1029/2006JC003615>. C12016.
- B. Huisman, M. de Schipper, and B. Ruessink. Sediment sorting at the sand motor at storm and annual time scales. *Marine Geology*, pages –, 2016. ISSN 0025-3227. doi: <http://dx.doi.org/10.1016/j.margeo.2016.09.005>. URL <http://www.sciencedirect.com/science/article/pii/S0025322716301918>.
- J. P. T. Kalkwijk and R. Booij. Adaptation of secondary flow in nearly-horizontal flow. *Journal of Hydraulic Research*, 24(1):19–37, 1986. doi: 10.1080/00221688609499330.
- M. Kleinhans, B. Grasmeyer, T. Dolphin, and B. Ruessink. *Apparent Current Roughness Caused by Waves and Bedforms on a Sandy Shoreface*, chapter 4, pages 1–11. 2005. doi: 10.1061/40855(214)5. URL <http://ascelibrary.org/doi/abs/10.1061/40855%28214%295>.
- M. G. Kleinhans. Sediment dynamics on the shoreface and upper continental shelf, a review. Technical report, Universiteit Utrecht, 2002.
- M. G. Kleinhans and B. T. Grasmeyer. Bed load transport on the shoreface by currents and waves. *Coastal Engineering*, 53:983–996, 2006.
- J. R. Lacy and S. G. Monismith. Secondary currents in a curved, stratified, estuarine channel. *Journal of Geophysical Research: Oceans*, 106(C12):31283–31302, 2001.
- A. Lefebvre, V. B. Ernsten, and C. Winter. Influence of compound bedforms on hydraulic roughness in a tidal environment. *Ocean Dynamics*, 61(12):2201–2210, 2011. ISSN 1616-7228. doi: 10.1007/s10236-011-0476-6. URL <http://dx.doi.org/10.1007/s10236-011-0476-6>.
- M. Z. Li, L. Wright, and C. L. Amos. Predicting ripple roughness and sand resuspension under combined flows in a shoreface environment. *Marine Geology*, 130(1–2):139 – 161, 1996. ISSN 0025-3227. doi: [http://dx.doi.org/10.1016/0025-3227\(95\)00132-8](http://dx.doi.org/10.1016/0025-3227(95)00132-8). URL <http://www.sciencedirect.com/science/article/pii/0025322795001328>.

- K. E. Lofquist. Sand ripple growth in an oscillatory-flow water tunnel. Technical report, DTIC Document, 1978.
- A. P. Luijendijk, F. Scheel, L. Braat, and N. Waagmeester. Pilot application of Delft3D Flexible Mesh: Assisting a field campaign at the Sand Engine. In *E-proceedings of the 36th IAHR World Congress*. International Association for Hydro-Environment Engineering and Research, 2015.
- A. P. Luijendijk, R. Ranasinghe, B. A. Huisman, M. A. Schipper, C. M. Swinkels, D. J. R. Walstra, and M. J. F. Stive. The initial morphological response of the sand engine: a process-based modeling study. *Coastal Engineering*, pages 1–14, 2017.
- L. Maas and J. Van Haren. Observations on the vertical structure of tidal and inertial currents in the central north sea. *Journal of Marine Research*, 45(2):293–318, 1987.
- O. S. Madsen. Spectral wave-current bottom boundary layer flows. In *Coastal Engineering 1994: Proceedings, 24th International Conference, Coastal Engineering Research Council*, pages 384–398. American Society of Civil Engineers, 1994.
- G. Masselink, M. Austin, T. O’Hare, and P. Russell. Geometry and dynamics of wave ripples in the nearshore zone of a coarse sandy beach. *Journal of Geophysical Research: Oceans*, 112(C10), 2007.
- S. Meirelles and S. B. Vinzon. Field observation of wave damping by fluid mud. *Marine Geology*, 376:194 – 201, 2016. ISSN 0025-3227. doi: <http://dx.doi.org/10.1016/j.margeo.2016.03.006>.
- S. Meirelles and N. Violante-Carvalho. Ocean wave propagation modelling: a tool to understand optical phenomena. *Revista Brasileira de Ensino de Fisica*, 29:555 – 563, 00 2007. ISSN 1806-1117.
- S. Meirelles, A. Horner-Devine, M. Henriquez, M. Stive, J. Pietrzak, and A. Souza. Middle shoreface sand transport under stratified regimes. In A. Green and J. Cooper, editors, *Proceedings 13th International Coastal Symposium (Durban, South Africa)*, number 70, pages 182–186. Journal of Coastal Research, 2014.
- S. Meirelles, M. Henriquez, A. R. Horner-Devine, A. J. Souza, J. Pietrzak, and M. Stive. Bed shear stress on the middle shoreface of the South-Holland coast. In *The Proceedings of the Coastal Sediments 2015*. World Scientific, 2015a.

- S. Meirelles, M. Henriquez, A. Reniers, M. Stive, J. Pietrzak, A. J. Souza, and A. Horner-Devine. On the impact of a mega localized nourishment on the tidal currents. In *E-proceedings of the 36th IAHR World Congress, The Hague, The Netherlands*, 2015b.
- S. Meirelles, M. Henriquez, A. J. Souza, A. R. Horner-Devine, J. D. Pietrzak, S. Rijnsburg, and M. J. F. Stive. Small scale bedform types off the South-Holland coast. *Journal of Coastal Research*, 75(sp1):423–426, 2016.
- S. Meirelles, M. Henriquez, A. Reniers, A. P. Luijendijk, J. Pietrzak, A. R. Horner-Devine, A. J. Souza, and M. J. F. Stive. Cross-shore stratified tidal flow seaward of a mega-nourishment. *Estuarine, Coastal and Shelf Science*, 200:59 – 70, 2018a. ISSN 0272-7714. doi: <https://doi.org/10.1016/j.ecss.2017.10.013>. URL <http://www.sciencedirect.com/science/article/pii/S0272771416306333>.
- S. Meirelles, M. Henriquez, A. Reniers, A. P. Luijendijk, J. Pietrzak, A. R. Horner-Devine, A. J. Souza, and M. J. F. Stive. Cross-shore stratified tidal flow seaward of a mega-nourishment. *Estuarine, Coastal and Shelf Science*, 200:59 – 70, 2018b. ISSN 0272-7714. doi: <https://doi.org/10.1016/j.ecss.2017.10.013>.
- S. Meirelles, A. J. Souza, A. Horner-Devine, J. Pietrzak, M. Henriquez, S. Rijnsburg, R. Flores, M. J. F. Stive, and A. Reniers. Effects of a stratified tidal flow on bedform dynamics. Submitted to the *Journal of Geophysical Research*, 2019.
- T. R. Nelson and G. Voulgaris. Temporal and spatial evolution of wave-induced ripple geometry: Regular versus irregular ripples. *Journal of Geophysical Research: Oceans*, 119(2):664–688, 2014. ISSN 2169-9291. doi: 10.1002/2013JC009020. URL <http://dx.doi.org/10.1002/2013JC009020>.
- T. R. Nelson and G. Voulgaris. A spectral model for estimating temporal and spatial evolution of rippled seabeds. *Ocean Dynamics*, 65(2):155–171, 2015. ISSN 1616-7228. doi: 10.1007/s10236-014-0801-y. URL <http://dx.doi.org/10.1007/s10236-014-0801-y>.
- U. Neumeier, C. Ferrarin, C. L. Amos, G. Umgiesser, and M. Z. Li. Sedtranso5: An improved sediment-transport model for continental shelves and coastal waters with a new algorithm for cohesive sediments. *Computers & Geosciences*, 34(10):1223 – 1242, 2008. ISSN 0098-3004. doi: <https://doi.org/10.1016/j.cageo.2008.02.007>. URL <http://www.sciencedirect.com/science/article/pii/S0098300408000538>. Predictive Modeling in Sediment Transport and Stratigraphy.

- R. Nicholls, P. Wong, V. Burkett, J. Codignotto, J. Hay, R. McLean, S. Ragoonaden, and C. Woodroffe. *Coastal systems and low-lying areas.*, chapter 6, pages 315–356. 2007.
- P. Nielsen, D. P. Callaghan, and T. E. Baldock. Downward transfer of momentum by wind-driven waves. *Coastal Engineering*, 58(12):1118–1124, 2011.
- A. J. Odgaard. Meander flow model. I: Development. *Journal of Hydraulic engineering*, 1986.
- A. P. Oost and J. H. Baas. The development of small scale bedforms in tidal environments: an empirical model for unsteady flow and its applications. *Sedimentology*, 41(5):883–903, 1994.
- R. Pawlowicz, B. Beardsley, and S. Lentz. Classical tidal harmonic analysis including error estimates in matlab using t_tide. *Computers & Geosciences*, 28(8):929–937, 2002.
- J. T. Perron, J. W. Kirchner, and W. E. Dietrich. Spectral signatures of characteristic spatial scales and nonfractal structure in landscapes. *Journal of Geophysical Research: Earth Surface*, 113(F4), 2008.
- D. Pugh. *Tides, surges and mean sea-level (reprinted with corrections)*. John Wiley & Sons Ltd, 1996. URL <https://eprints.soton.ac.uk/19157/>. Book out of print - COPYRIGHT OWNED BY AUTHOR.
- M. Radermacher, M. A. de Schipper, C. Swinkels, J. H. MacMahan, and A. J. Reniers. Tidal flow separation at protruding beach nourishments. *Journal of Geophysical Research: Oceans*, 2016. ISSN 2169-9291. doi: 10.1002/2016JC011942. URL <http://dx.doi.org/10.1002/2016JC011942>.
- R. E. Raye and F. R. Driscoll. Inertial correction of ship-mounted ADCP records. In F. H. Maltz, editor, *Proceedings Oceans 2002 (Biloxi, MS)*. Ocean Engineering Society, 2002.
- A. J. Reniers, J. Roelvink, and E. Thornton. Morphodynamic modeling of an embayed beach under wave group forcing. *Journal of Geophysical Research: Oceans*, 109(C1), 2004.
- H. E. Seim and M. C. Gregg. The importance of aspiration and channel curvature in producing strong vertical mixing over a sill. *Journal of Geophysical Research: Oceans*, 102(C2):3451–3472, 1997. ISSN 2156-2202. doi: 10.1029/96JC03415. URL <http://dx.doi.org/10.1029/96JC03415>.

- W. J. Shaw and J. H. Trowbridge. The direct estimation of near-bottom turbulent fluxes in the presence of energetic wave motions. *Journal of Atmospheric and Oceanic Technology*, 18(9):1540–1557, 2001.
- J. Simpson. Physical processes in the ROFI regime. *Journal of Marine Systems*, 12(1-4):3–15, Aug. 1997. ISSN 09247963. doi: 10.1016/S0924-7963(96)00085-1. URL <http://www.sciencedirect.com/science/article/pii/S0924796396000851>.
- J. Simpson and A. Souza. Semidiurnal switching of stratification in the region of freshwater influence of the Rhine. *Journal of Geophysical Research*, 100(C4):7037–7044, 1995.
- J. Simpson, E. Williams, L. Brasseur, and J. Brubaker. The impact of tidal straining on the cycle of turbulence in a partially stratified estuary. *Continental Shelf Research*, 25(1):51 – 64, 2005. ISSN 0278-4343. doi: <http://dx.doi.org/10.1016/j.csr.2004.08.003>. URL <http://www.sciencedirect.com/science/article/pii/S0278434304002122>.
- J. H. Simpson, W. G. Bos, F. Schirmer, A. J. Souza, T. P. Rippeth, S. E. Jones, and D. Hydes. Periodic stratification in the Rhine ROFI in the north sea. *Oceanologica Acta*, 16(1):23–32, 1993.
- C. E. Smyth and M. Z. Li. Wave-current bedform scales, orientation, and migration on sable island bank. *Journal of Geophysical Research: Oceans*, 110(C2):n/a–n/a, 2005. ISSN 2156-2202. doi: 10.1029/2004JC002569. URL <http://dx.doi.org/10.1029/2004JC002569>. Co2023.
- J. E. Solem. *Programming Computer Vision with Python: Tools and algorithms for analyzing images*. " O'Reilly Media, Inc.", 2012.
- R. Soulsby. *Dynamics of Marine Sands: A Manual for Practical Applications*. Telford, 1997. ISBN 9780727725844. URL <https://books.google.nl/books?id=4N1M51WIyAoC>.
- R. Soulsby, L. Hamm, G. Klopman, D. Myrhaug, R. Simons, and G. Thomas. Wave-current interaction within and outside the bottom boundary layer. *Coastal Engineering*, 21(1-3):41–69, 1993.
- R. L. Soulsby and S. Clarke. Bed shear-stresses under combined wave sand currents on smooth and rough beds. Technical report, HR Wallingford, 2005. URL http://www.estproc.net/EstProc_library.htm.

- A. Souza and J. Simpson. The modification of tidal ellipses by stratification in the Rhine ROFI. *Continental Shelf Research*, 16(8):997–1007, 1996.
- A. J. Souza and I. D. James. A two-dimensional (x- z) model of tidal straining in the Rhine ROFI. *Continental Shelf Research*, 16(7):949–966, 1996.
- A. J. Souza and J. H. Simpson. Controls on stratification in the Rhine ROFI system. *Journal of Marine Systems*, 12(1):311–323, 1997.
- G. S. Stelling and J. A. T. M. Van Kester. On the approximation of horizontal gradients in sigma co-ordinates for bathymetry with steep bottom slopes. *International Journal for Numerical Methods in Fluids*, 18(10):915–935, 1994.
- M. J. F. Stive and H. J. de Vriend. Modelling shoreface profile evolution. *Marine Geology*, 126:235–248, 1995.
- M. J. F. Stive, M. A. de Schipper, A. P. Luijendijk, S. G. J. Aarninkhof, C. van Gelder-Maas, J. S. M. van Thiel de Vries, S. de Vries, M. Henriquez, S. Marx, and R. Ranasinghe. A new alternative to saving our beaches from sea-level rise: The sand engine. *Journal of Coastal Research*, 29(5):1001–1008, 2013.
- R. E. Thomson and W. J. Emery. *Data analysis methods in physical oceanography*. Newnes, 2014.
- P. D. Thorne and D. Hurther. An overview on the use of backscattered sound for measuring suspended particle size and concentration profiles in non-cohesive inorganic sediment transport studies. *Continental Shelf Research*, 73:97 – 118, 2014. ISSN 0278-4343. doi: <https://doi.org/10.1016/j.csr.2013.10.017>. URL <http://www.sciencedirect.com/science/article/pii/S0278434313003488>.
- P. Traykovski. Observations of wave orbital scale ripples and a nonequilibrium time-dependent model. *Journal of Geophysical Research: Oceans*, 112(C6), 2007.
- A. Valle-Levinson, K. Huguenard, L. Ross, J. Branyon, J. MacMahan, and A. Reniers. Tidal and nontidal exchange at a subtropical inlet: Destin inlet, north-west florida. *Estuarine, Coastal and Shelf Science*, 155:137 – 147, 2015. ISSN 0272-7714. doi: <http://dx.doi.org/10.1016/j.ecss.2015.01.020>. URL <http://www.sciencedirect.com/science/article/pii/S0272771415000414>.
- J. W. H. van de Meene and L. Van Rijn. The shoreface-connected ridges along the central Dutch coast - part 1: field observation. *Continental Shelf Research*, 20:2295–2323, 2000.

- A. Van der Giessen, W. De Ruijter, and J. Borst. Three-dimensional current structure in the Dutch coastal zone. *Netherlands Journal of Sea Research*, 25(1):45–55, 1990.
- H. van Haren. Properties of vertical current shear across stratification in the North Sea. *Journal of Marine Research*, 58(3):465–491, 2000.
- L. van Rijn. *Principles of sediment transport in rivers, estuaries and coastal seas*. Aqua Publications, 1993. ISBN 9789080035621.
- L. Van Rijn. Sediment transport and budget of central coastal zone of holland. *Coastal Engineering*, 32:61–90, 1997.
- L. van Rijn. *SANDPIT - Sand transport and morphology of offshore mining pits: process knowledge and guidelines for coastal management*. Aqua Publications, 2005.
- T. Vermaas. Morphological behaviour of the deeper part of the holland coast. Technical report, Deltares, 2010.
- C. E. Vincent, D. M. Hanes, and A. J. Bowen. Acoustic measurements of suspended sand on the shoreface and the control of concentration by bed roughness. *Marine Geology*, 96(1–2):1–18, 1991. ISSN 0025-3227. doi: [http://dx.doi.org/10.1016/0025-3227\(91\)90199-E](http://dx.doi.org/10.1016/0025-3227(91)90199-E). URL <http://www.sciencedirect.com/science/article/pii/002532279190199E>.
- A. Visser, A. Souza, K. Hessner, and J. Simpson. The effect of stratification on tidal current profiles in a region of fresh-water influence. *Oceanologica acta*, 17(4):369–381, 1994.
- D. J. R. Walstra, L. C. van Rijn, and S. Aarninkhof. Sand transport of the middle and lower shoreface of the Dutch coast: simulation of suntrench model and proposal for large scale laboratory test. Technical report, Delft Hydraulics, 1998.
- P. L. Wiberg and C. R. Sherwood. Calculating wave-generated bottom orbital velocities from surface-wave parameters. *Computers & Geosciences*, 34(10):1243 – 1262, 2008. ISSN 0098-3004. doi: <http://dx.doi.org/10.1016/j.cageo.2008.02.010>. URL <http://www.sciencedirect.com/science/article/pii/S009830040800054X>.
- K. M. Wijnberg. Environmental controls on decadal morphologic behaviour of the holland coast. *Marine Geology*, 189(3-4):227–247, 2002. ISSN 0025-3227. doi: [http://dx.doi.org/10.1016/S0025-3227\(02\)00480-2](http://dx.doi.org/10.1016/S0025-3227(02)00480-2). URL <http://www.sciencedirect.com/science/article/pii/S0025322702004802>.

- L. Wright. Sediment transport and deposition at river mouths: a synthesis. *Geological Society of America Bulletin*, 88(6):857–868, 1977.
- L. Wright. *Morphodynamics of inner continental shelves*. CRC series in marine science. CRC Press, 1995.

ACKNOWLEDGMENTS

Although this thesis is (unjustly) single authored, many hands and minds were responsible for making this happen. Thus, I am indebted to all the “co-authors” who helped me in many ways to put the pieces that compose this thesis together. I would like to thank Marcel for accepting me in the NEMO project and all the support over the research years. I thank Julie, Ad, Alex Souza, Alex Horner-Devine and Martijn for their guidance. I appreciate the help of Arjen, Raul and Sabine with the publications and Howard for proof-reading the manuscripts. My gratitude to the scientific and technical crews involved in the STRAINS/MegaPEX field campaigns, since the preparations. Filipe Fernandes and Stack Overflow (🙏) are thanked for all the Python support. The National Oceanography Center (NOC) is thanked for providing great technical and intellectual support. My very special thanks to the Dutch talented trio: Bas (Forest) Huisman, Bas (Smith) Hoonhout and Max (Cavalera) Radermacher. My lovely family and friends in Brazil, Delft and Shenzhen are also thanked for the good moments. My heartfelt thanks to Mini, Yang and Bel for simply bringing joy and serenity to my everyday life ♡. “All we need is love”.

Saulo Meirelles
Shenzhen, July 2018

CURRICULUM VITAE

PERSONALIA

Saulo Meirelles

May 14, 1981, Rio de Janeiro, Brazil

EDUCATION

1999 – 2001 Federal Technical School of Chemistry of Rio de Janeiro

2002 – 2006 Rio de Janeiro State University, BSc Oceanography

2007 – 2010 Federal University of Rio de Janeiro, MSc Coastal Engineering

EMPLOYMENT

2008 – 2012 Oceanographer at Petrobras

2013 – 2018 PhD candidate at Delft University of Technology

PUBLICATIONS

LIST OF SELECTED PUBLICATIONS

- S. Meirelles, M. Henriquez, A. Reniers, A. P. Luijendijk, J. Pietrzak, A. R. Horner-Devine, A. J. Souza, and M. J. F. Stive. Cross-shore stratified tidal flow seaward of a mega-nourishment. *Estuarine, Coastal and Shelf Science*, 200:59 – 70, 2018b. ISSN 0272-7714. doi: <https://doi.org/10.1016/j.ecss.2017.10.013>.
- S. Meirelles, A. J. Souza, A. Horner-Devine, J. Pietrzak, M. Henriquez, S. Rijnsburg, R. Flores, M. J. F. Stive, and A. Reniers. Effects of a stratified tidal flow on bedform dynamics. Submitted to the *Journal of Geophysical Research*, 2019.
- S. Meirelles, M. Henriquez, A. J. Souza, A. R. Horner-Devine, J. D. Pietrzak, S. Rijnsburg, and M. J. F. Stive. Small scale bedform types off the South-Holland coast. *Journal of Coastal Research*, 75(sp1):423–426, 2016.
- S. Meirelles and S. B. Vinzon. Field observation of wave damping by fluid mud. *Marine Geology*, 376:194 – 201, 2016. ISSN 0025-3227. doi: <http://dx.doi.org/10.1016/j.margeo.2016.03.006>.
- S. Meirelles, M. Henriquez, A. Reniers, M. Stive, J. Pietrzak, A. J. Souza, and A. Horner-Devine. On the impact of a mega localized nourishment on the tidal currents. In *E-proceedings of the 36th IAHR World Congress, The Hague, The Netherlands*, 2015b.
- S. Meirelles, M. Henriquez, A. R. Horner-Devine, A. J. Souza, J. Pietrzak, and M. Stive. Bed shear stress on the middle shoreface of the South-Holland coast. In *The Proceedings of the Coastal Sediments 2015*. World Scientific, 2015a.
- S. Meirelles, A. Horner-Devine, M. Henriquez, M. Stive, J. Pietrzak, and A. Souza. Middle shoreface sand transport under stratified regimes. In A. Green and J. Cooper, editors, *Proceedings 13th International Coastal Symposium (Durban, South Africa)*, number 70, pages 182–186. *Journal of Coastal Research*, 2014.
- S. Meirelles and N. Violante-Carvalho. Ocean wave propagation modelling: a tool to understand optical phenomena. *Revista Brasileira de Ensino de Fisica*, 29:555 – 563, 00 2007. ISSN 1806-1117.

This document was typeset using the typographical look-and-feel `classicthesis` developed by André Miede.